The Design of an Audio Recorder for Respiratory Sound Recording

by:

Jeffrey Winkler

Thesis submitted to the Faculty of Graduate Studies of

The University of Manitoba

in partial fulfilment of the requirements of the degree of

MASTER OF SCIENCE

Biomedical Engineering

University of Manitoba

Winnipeg, Canada

Abstract

Respiratory sound analysis offers critical and clear advantages for diagnosis and monitoring of respiratory disorders. Yet, the recording technology available today remains relatively undeveloped and non-specialized. Standard high-quality audio recording systems often do not capture the low-frequency spectrum of respiratory sounds; not to mention such equipment typically has high associated costs. Contributing to the issue is a lack of standardization of equipment used; hence, what follows is a large variability of the recordings and the inability to effectively compare results between different recording systems.

The objective of the following presented work was to design and build an electronic audio recording device along with microphone and suitable air-chamber to be placed over the trachea or lung for capturing respiratory breathing sounds. Design objectives included maintaining a cost-effective, portable, and small form-factor for the device as well as compatibility with our team's patented obstructive sleep apnea (OSA) diagnostic algorithms to detect for the severity of OSA during either overnight sleep or wakefulness.

All desired objectives for the design were able to be realized in a compact, cost-effective, and highly accurate device. When reviewing the tracheal breathing sound recordings conducted with the device, the results identify signal content, albeit low amplitude, past 5 kHz up to 9 kHz; that indicates the previous cut-off point of many precursory studies might not have been adequate for capturing the entire characteristic features of tracheal respiratory sounds.

Table of Contents

Table of Figures

List of Tables

Acronyms

Symbol	Description
3D	3 Dimensional
ABS	Acrylonitrile Butadiene Styrene
AC	Alternating Current
BMI	Body-Mass Index
CSA	Central Sleep Apnea
DC	Direct Current
FET	Field-Effect Transistor
GPIO	General-Purpose Input/Output
IC	Integrated Circuit
I^2C	Inter-Integrated Circuit
LiPo	Lithium-Ion Polymer
MSA	Complex/Mixed Sleep Apnea
NiCd	Nickel Cadmium
Ni-MH	Nickel Metal Hydride
OLED	Organic LED
OS	Operating System
OSA	Obstructive Sleep Apnea
PLA	Polylactic Acid
PNP	Transistor with one n-type material doped with two p-type materials
PSG	Polysomnogram
SPI	Serial Peripheral Interface
UART	Universal Asynchronous Receiver/Transmitter
USB	Universal Serial BUS
UPS	Uninterrupted Power Supply

Units

Symbol	Description
dB	Decibel
GB	Gigabyte
Hz	Hertz
KB	Kilobyte
kHz	Kilo Hertz
mAh	Milli-Amp Hour
V	Volts

Acknowledgements

I would like to kindly thank my advisor, Dr. Zahra Moussavi, for all the support and guidance she has provided throughout my entire time in the Master's program. I look back to the time when I first started the Master's program and I am both a better researcher and person because of the experience I have gained while under your supervision. Thank you too to my research committee who have been there in the background and helped guide me along the way. As well, thank you to Ahmed Elwali, Ph.D. for the assistance provided during the data capture and analysis stages. And finally, I thank my parents and all the people who have helped and supported me while I have undertaken this endeavour.

Chapter 1

1. Introduction

1.1. Motivation

Auscultation of respiratory sounds over the trachea and lungs has been a major diagnostic tool for diagnosis of lung infectious diseases. The invention of the stethoscope in 1816 initiated the use of respiratory sounds for diagnostic purposes and continues to be a useful and invaluable diagnostic tool used by medical professionals around the world even to this day. With advances in electronics and computer technologies, the capture and analysis using such devices has the potential to play a major role in advancing the field, yet such devices remain relatively undeveloped and non-specialized for use in the diagnosis of respiratory disorders.

Obstructive sleep apnea (OSA) is a common respiratory disorder with many serious implications, yet it has remained underdiagnosed [5]. Questionnaire-based screening techniques for OSA are a quick way to screen but result in a high rate of false positives, contributing to a significant strain on the healthcare system and significantly delaying those individuals who need treatment for OSA. The current standardized method for diagnosing OSA is by means of a polysomnographic (PSG) study, which is monitoring a multitude of physiological measures during sleep. The aim of an overnight, full PSG study is to assess the number of shallow or halted breathing events per an hour of sleep experienced by the individual being recorded along with the duration of each event, sleep stages, the number of arousals, heart rate, blood oxygen saturation level (SaO2), snoring, etc. Thus, during a PSG study many signals including electroencephalography (EEG), electrocardiography (ECG), electromyography (EMG), electrooculography (EOG), blood oxygen saturation (SaO_2), and airflow measurements are collected over a span of 6-8 hours overnight. Naturally, such an elaborate recording procedure requires setup, observation, and manual analysis by a trained technician. PSG is therefore a resource intensive and expensive assessment.

For those individuals who cannot wait for an overnight PSG assessment (i.e., those who are in need an immediate surgery), OSA risk assessment is commonly done using the STOP-Bang questionnaire [6] which is a quick and simple clinical screening tool. The questionnaire contains a set of 8 questions which considers the individual’s snoring criteria, tiredness, observed apneas, blood pressure, body-mass index (BMI), age, neck circumference, and gender. The questionnaire then provides scoring criteria to define the individual’s risk of OSA, being either low, intermediate, or high risk. The STOP-Bang questionnaire has a high sensitivity to detect moderate and severe OSA (> 93%) but a very low specificity (< 37-49%) [7] [6]. This means a significant number of individuals without OSA (the false positives) will continue to be falsely referred to PSG assessment, or if there is no time for a PSG before surgery, many unnecessary pre- and post-operative resources will be expended. Thus, a quick and reliable screening tool, but with much higher specificity for OSA and its severity would be extremely useful, but it is challenging to develop as people with OSA do not show any apparent symptoms during wakefulness.

Diagnosis of OSA by acoustical means has received substantial attention in the last decade. Our research team have been pioneering the use of tracheal respiratory sounds to effectively screen for the severity of OSA with a comparable accuracy to that of PSG either during sleep [8] or wakefulness [2] [9]. Our team's designed diagnostic algorithm for OSA screening during wakefulness, called AWakeOSA [2], utilizes tracheal breathing sounds recorded by microphone to effectively identify those individuals with moderate and severe OSA with a high sensitivity and specificity (86% and 85%, respectively) [2] [3]. Our team has shown the potential of high-quality respiratory sounds analysis to diagnose and monitor respiratory disorders in addition to investigating the underlying mechanisms of OSA. There are also other research groups around the world who also use breathing sounds analysis for diagnosis of OSA [10] [11].

1.2. Respiratory Sound Characteristics

Auscultation of breathing sounds at the surface of the skin for assessing various respiratory infections or disorders has been commonplace in the last 200 years and is highlighted by the continued utilization of the stethoscope for routine examination. Similarly, the main characteristics of respiratory sounds has been explored and documented, especially within the last 30 years. Of primary concern in regard to this project are the characteristics of tracheal and lung sounds during the respiratory phases of inspiration and expiration. From previous studies, the frequency span and relative intensity of the respective respiratory sounds has been identified. Tracheal sounds are generated as a result of turbulent airflow through the upper airway and its resulting resonances; thus, are useful for explaining the upper airway structure. Tracheal sounds form a broad spectrum with components commonly observed below 100 Hz to a range in excess of 3000 Hz at the normal flow rate and are relatively high amplitude [12]. With a strong correlation to airflow through the upper airway, the analysis of tracheal sounds are an ideal and consistent means for acoustic flow estimation techniques [13] [14]. On the other hand, characteristics of tracheal sounds exhibited during inspiration relative to expiration show little consistency from person to person and in turn make it difficult to determine the respiratory phase from tracheal sounds alone.

In contrast to tracheal sounds, lung sounds result from turbulent airflow through the central airways with a low-pass filtering effect applied as the sounds pass through the chest wall. As such, lung sounds form a narrower spectrum with components commonly observed below 100 Hz to a range in excess of 1000 Hz and show lower amplitude relative to tracheal sounds [12]. Lung sounds exhibit a characteristic behaviour whereby sounds produced during the inspiratory phase are consistently louder than during the expiratory phase when measured from the same location, thus, lung sounds work well for respiratory phase identification. While respiratory phase identification can be achieved by simultaneous recording of tracheal and lung sounds [15] [16] and is important for our group's acoustic OSA algorithms, the main application of both tracheal and lung sounds has been on diagnosing conditions such as OSA [2] [3] [8], asthma [17], and other respiratory infectious diseases [18].

1.3. Research Goal

The goal of this thesis was to design and fabricate a new, specialized, audio recording system for capturing respiratory sounds, and to be used primarily in conjunction with the AWakeOSA algorithm for OSA severity screening. Of primary importance with the new device was to optimize the design of the air-chamber (which allows respiratory sounds to be collected from the surface of the skin by microphone) and to capture sounds with high-quality and high-sampling rate. With the primary goal to function as a diagnostic tool, the quality of sounds recorded is paramount to ensuring the diagnostic algorithms receive the best possible information to make an accurate analysis. As well, the high-sampling rate permits a greater range of frequencies to be captured and allow our team the ability to explore if tracheal sounds have spectral components in excess of 5 kHz. Compact-Disc digital audio format was considered as the standard for high-quality and high-sampling rate whereby data is stored in 2-channel, 16-bit digital format at a sampling rate of 44,100 Hz.

Our research team had put together and used a set of audio recording equipment to enable capturing of tracheal breathing sounds. Although proven effective, the previous recording system suffered from several limitations. Namely, it was limited in performance where the maximum frequency of sounds recorded was 5 kHz. As well, the composition of components comprising the previous system was large and cumbersome. Lastly, the design of the air-chamber used with the previous system had not been optimized.

The new device should be able to record both tracheal and lung respiratory sounds in two channels simultaneously. The design of the Air-Chamber for use with the microphone should be optimized. The new device should have a small form-factor and be easily transportable. Furthermore, the new recording system should also maintain a cost-effective manufacture, as much as possible.

1.4. Previous Audio Recording System

The previous recording system used by our research group (let this system be known as the Biopac System) is an assembly of commercial audio amplifier and acquisition equipment. As such, the Biopac System forms the basis for the design of the newly designed Audio Recorder described by this report. As a loosely stated objective, the new Audio Recorder should meet or exceed the characteristics of the Biopac System yet in doing so, be compact in size and remain relatively inexpensive to manufacture. The hardware comprising the Biopac System is thus briefly explained.

Starting from sound source acquisition, the Biopac System utilizes a single Sony ECM-77B electret condenser microphone to record tracheal breathing sounds. The Biopac System does not have a means to record lung sounds and the respiratory phase is recorded manually by the operator. The microphone is powered via an internal AA battery and makes two connections with the Biopac hardware: one connection to provide the audio signal and a second connection for ground.

Figure 1.1. Sony ECM-77B electret condenser microphone; silver cylinder contains the battery and other related circuitry to power microphone. Microphone element shown inserted to custom Microphone Coupler.

The audio signal from the ECM-77B microphone is supplied to an electronic amplifier (Manufacturer: BIOPAC Systems Canada, Inc., Product Number: MCE100C). Connected to the amplifier module is an isolated power supply (Manufacturer: BIOPAC Systems Canada, Inc., Product Number: IPS100C) that acts to power the amplifier module as well as direct the amplified output of the amplifier module to external equipment via 3.5 mm phone jacks on the front panel. From the phone jack on the front of the power supply module, the audio signal is next sent to an analog-to-digital converter (Manufacturer: National Instruments, Product Number: NI-9215, Precision: 16-bit) with USB carrier (Manufacturer: National Instruments, Product Number: NI USB-9162). The output of the analog-to-digital converter is transmitted via a USB cable to a laptop

PC. To record the audio information a custom program running in the LabVIEW graphical programming environment is employed. From the LabVIEW program, an audio file is generated and later analyzed post-recording via the AWakeOSA algorithm.

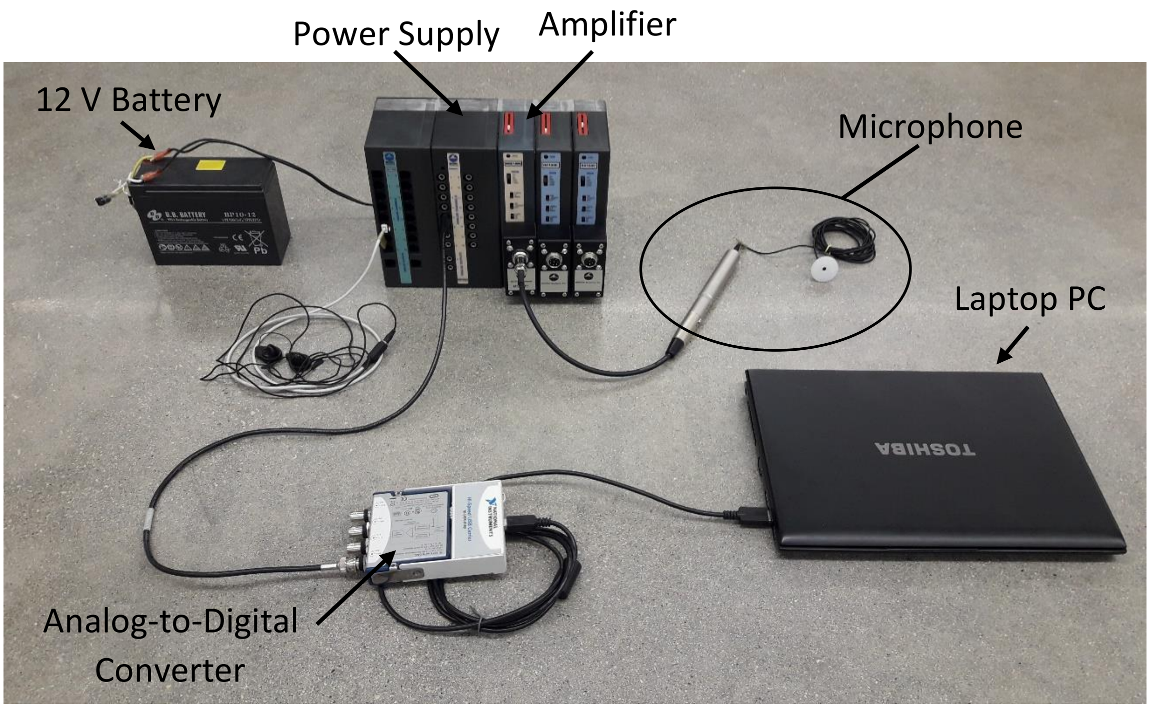

Figure 1.2. Biopac System with main components illustrated.

1.5. Organization of the Thesis

This thesis report has been organized into eight chapters of which describe the process for the design and manufacture of a new, specialized audio recording device for capturing respiratory sounds; called the ASAD-III. The newly designed recording device is realized as a compilation of components that form the overall working device. Following the introduction presented by Chapter 1 above, Chapter 2 provides a system overview of the components forming the ASAD-III system. Chapters 3 through to 6 present the individual major components of the audio recording system and within each chapter can be found the design, evaluation, and discussion of each major component. Chapter 7 presents concluding remarks and lastly, presented within Chapter 8 is the Appendix which contains a detailed review of OSA, system flow charts, schematics, and an overall project budget.

Chapter 2

2. ASAD-III System Overview

The developed system, named ASAD-III (Acoustic Sleep Apnea Detection, version 3), is an electronic audio recording device for capturing tracheal and lung respiratory sounds. The system is a compilation of components and can be described by two main component groups: the Audio Recorder and the Peripheral Components. The complete device is pictured within Fig. 2.1:

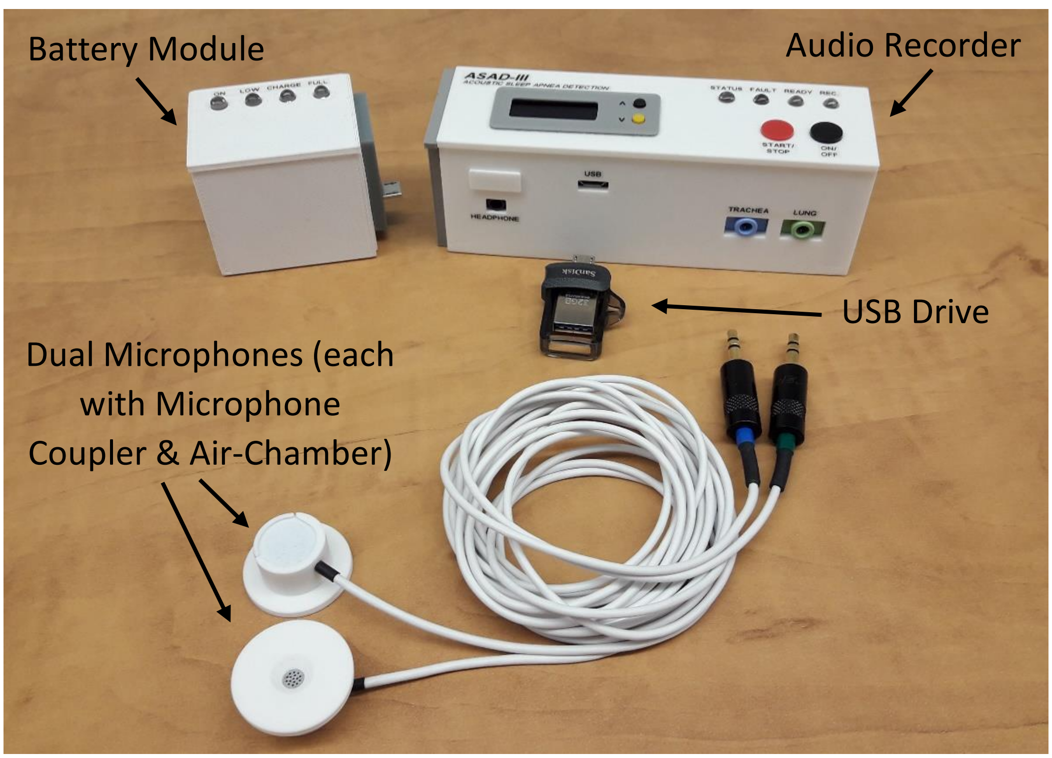

Figure 2.1. ASAD-III (Acoustic Sleep Apnea Detection, version 3) full system with components labelled.

The Audio Recorder is at the center of the system, containing the Central Processing Unit (CPU), Audio Interface Board, Microphone Power Supply Board, and dual User Interface Boards. The Audio Recorder contains all associated hardware to perform analog-to-digital conversion of the information streaming from the dual microphones and simultaneous storage of recorded sounds. Additionally, the dual User Interface Boards provide an intuitive, easy to use means for controlling the device and viewing recording progress.

The Peripheral Components are modular in design and attach to the Audio Recorder to form a complete, functional device. First and foremost are two separate, high quality microphones, for capturing tracheal and lung sounds, respectively. Augmenting the microphones and permitting their application are individual couplers for affixing the microphones to the skin and Air-Chambers to effectively convert chest wall vibrations into air-pressure changes. Lastly, a 1600 mAh battery pack that can independently power the Audio Recorder, or alternatively function as an uninterrupted power supply (UPS) makes this device a completely functional and highly accurate specialized Audio Recorder.

Overall design objectives include maintaining a cost-effective, portable, and small form-factor for the recording device. The recording device should also capture the acoustical information to be compatible with the patented AWakeOSA technology which analyzes the information post-recording [2]. Audio information is stored on the USB in the .WAV file format which permits transfer to and post-analysis via a support vector machine. In addition, the device should permit the recording of lung sounds simultaneously with tracheal sounds to allow for automatic respiratory phase detection using the method introduced in [16]. Hence, the recording device should allow for capture and recording of two channels of acoustic information simultaneously.

Chapter 3

3. Audio Recorder

3.1. Introduction

The Audio Recorder is the major module of the ASAD-III recording device and serves as a central hub onto which the peripheral components connect to. Inside the Audio Recorder are an array of electronic components, organized and described within this chapter by the individual circuit boards that collectively form the Audio Recorder. Of which, at the center of the Audio Recorder is a Raspberry Pi Zero W, a single board computer serving as the Central Processing Unit (CPU) of the device. Digitization of the analog signal from the microphones is performed using an Audio Interface Board (Fe-Pi Audio Z v2) which makes use of an on-board SGTL5000 low power stereo codec to perform the conversion. Also constituting the device is a Microphone Power Supply Board providing regulated power to each of the respective microphones. Finally, two custom User Interface Boards were designed and fabricated to manage and control all functions of the recording process and additionally display the status of the device while in use.

3.2. Design Specifications

A summary of the required specifications for the Audio Recorder is provided in Table 3.2-1. By design, the Audio Recorder should have two separate channels to record two sound channels (tracheal and lung sounds) simultaneously. The sampling rate of the Audio Recorder should be at least 20 kHz to capture sounds up to 10 kHz. The rationale for the sampling rate is to expand upon the previously investigated frequency range for tracheal breathing sounds. Resolution of the resulting digital signal should be at least 12-bits to record with enough accuracy to utilize the AWakeOSA algorithm with sufficient accuracy. Regarding the duration of recording respiratory sounds, the device should have the capability to record continuously for up to 8 hours uninterrupted in the application it is used for sleep studies performed overnight. Finally, the overall size of the device and the cost of manufacture of the device should be made minimal as much as possible, however doing so must not compromise the other required specifications.

Table 3.2-1. Audio Recorder Specifications

Feature:	**Value or Range:**	**Explanation:**
Number of Channels:	2	Number for separate inputs for microphones.
Sampling Rate:	$\geq$ 20 kHz	How often to sample the analog audio signal.
Resolution:	$\geq$ 12-bits	The quantization steps of the digitized signal.
Recording Duration	$\geq$ 8 hours	How long to record.
Device Size:	Hand-Held/Portable	Physical size of the entire recording device.

3.3. Design

Similar to the overall design as a whole, the design of the Audio Recorder and its internal components was constructed in a modular strategy, segmented into separate circuit boards, each of which explained within the following paragraphs of this chapter. This section details the design process, fabrication, and when necessary, modifications and overall techniques utilized to construct the complete Audio Recorder. A combination of commercially available and custom-built electronic circuits were utilized since, at least for several of the desired functions, there did not exist available solutions to perform such functions related to the specialized purpose of the device.

3.3.1. Central Processing Unit

At the center of the Audio Recorder and performing all logical operations of the device as a whole is the central processing unit: a Raspberry Pi Zero W. Utilizing an ARM1176JZF-S processor (1 GHz, single-core), the Raspberry Pi Zero is a small size (65 mm x 30 mm x 5 mm, weight 9 g) single-board computer with connectivity options including: 802.11 b/g/n wireless LAN, Bluetooth 4.1, and Bluetooth Low Energy (BLE) and having on-board peripherals including 512 MB RAM, mini HDMI connector (x1), micro universal serial BUS (USB) data port (x1), and 40-pin header pin connectivity for breakout of all power, general-purpose input/output (GPIO), and serial data transfer protocols (Serial Peripheral Interface (SPI), Inter-integrated Circuit (I^2C), Universal Asynchronous Receiver/Transmitter (UART)). Main on-board components of the Raspberry Pi are identified within Fig. 3.1:

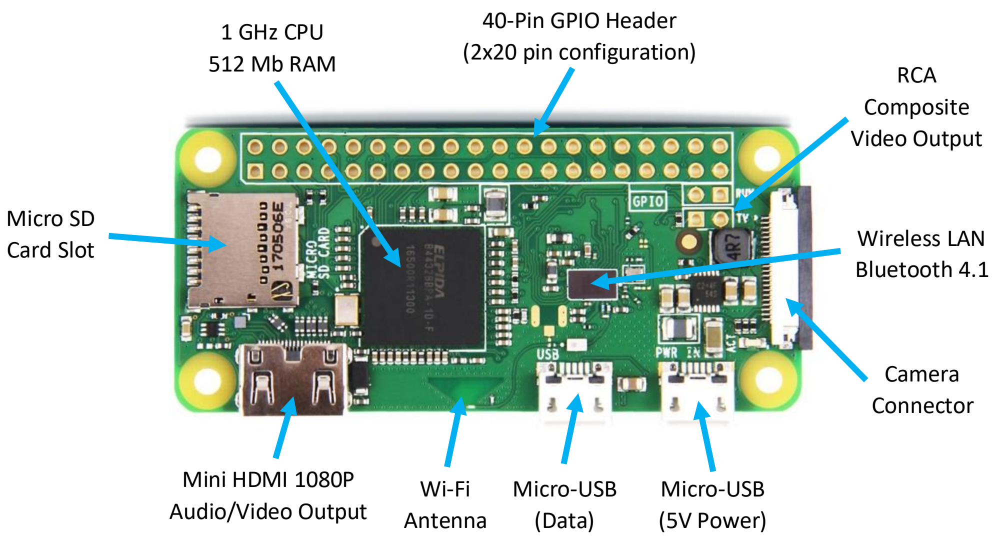

Figure 3.1. Raspberry Pi Zero W with main components labelled. Source: Adapted from [46].

Connectivity between the Raspberry Pi and all peripheral boards was accomplished exclusively via physical connections to the 40-pin GPIO header on the Raspberry Pi; the complete pin output configuration presented to the right in Fig. 3.2. Pins are referenced in one of two ways: either by Board Number, or by Broadcom SOC channel (BCM) number. The Board Number specifies the physical location of each and every pin on the board in a configuration starting the count at 1, from the top-most and left-most pin; and is noted by the number present inside the circles in Fig. 3.2 (ex. Board Number: 1 has the label "3V3 Power" and corresponds to the 3.3 Volt (V) pin). The BCM number is applicable to GPIO pins and distinctly identifies the GPIO pins following the lower-level numbering system defined by the Raspberry Pi's Broadcom-chip processor. For example, the pin labelled "GPIO2" is identified as BCM/GPIO: 2 or can also be referenced as Board Number: 3.

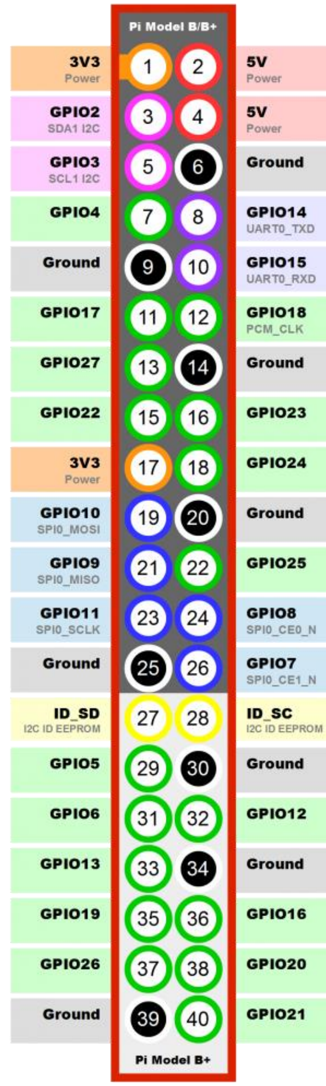

Figure 3.2. Raspberry Pi GPIO pin configuration layout. Source: [41].

The central processing unit (Raspberry Pi) used in the Audio Recorder is unmodified from its original configuration, excluding for two minor additions. The first addition is a set of extra-long male header pins (Pin Height: 17.0 mm, Pin Thickness: 0.6 mm, Pin Spacing: 2.54 mm) that were soldered to the 40-pin connector port of the Raspberry Pi (in a 2x20 configuration). Header pins were chosen in favor of wires or other connection techniques to form a sturdy, yet detachable connection that would allow for the desired modular design. Additionally, as several of the peripheral boards would be communicating with the Raspberry Pi to transfer digital data and commands at relatively high frequencies, the length of connectors between the boards had to remain short to ensure latency in the transmitted data would be negligible.

The male header pins were attached so the header pins extend both above and below the Raspberry Pi to permit connectivity (via female header sockets) to the other peripheral boards that comprise the Audio Recorder. Figure 3.3 illustrates the installation of the header pins:

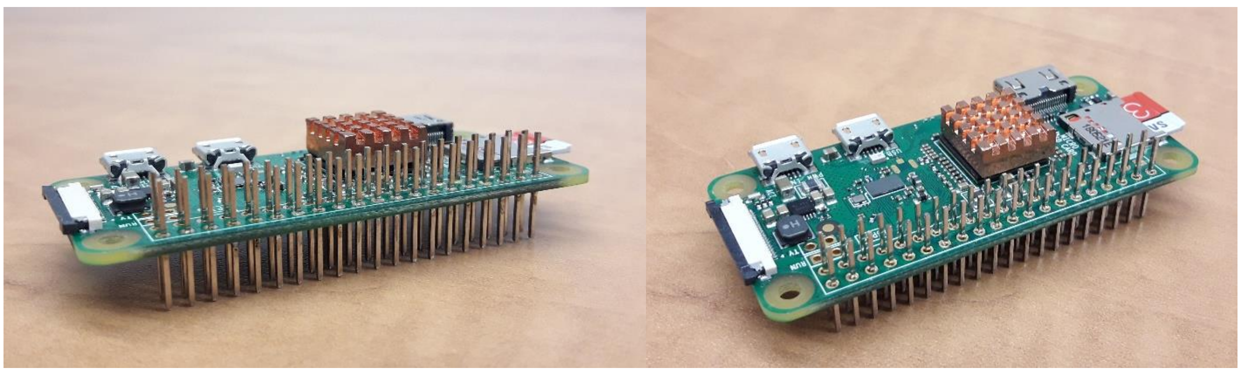

Figure 3.3. Raspberry Pi Zero W with header pins attached to GPIO pins.

The second addition to the Central Processing Unit was the installation of a copper heatsink (Manufacturer: DFRobot, Product Number: FIT0367, Dimensions: 13.2 mm x 12.1 mm x 5.5 mm) on the Raspberry Pi's microprocessor integrated circuit (IC). Although by default, the Raspberry Pi does not require a heatsink for operation, the heatsink was installed as a precautionary measure to help dissipate heat generated and ensure there would not be any issues with heat buildup in the IC over extended periods of use. The heat sink was adhered to the IC body using thermally conductive adhesive (Manufacturer: t-Global Technology, Product Number: LI98-1120-12-0.15, Thickness: 0.0060" (0.152mm), Thermal Conductivity: 0.9W/m-K).

The intended load on the Raspberry Pi was investigated to be only ~30% processor load for the audio recording task and as such, a heat sink with a sparsely distributed and widespread fin pattern was chosen to provide cooling via natural convection. A cooling fan setup was deemed unnecessary as the additional cooling capacity was not required, and additionally the noise and mechanical vibration of the fan, although minimal, were undesired characteristics for the final device. The heatsink is a passive device (requiring no power to operate) and does not generate noise or mechanical vibration, yet still adequately manages heat for the intended final purpose of the device.

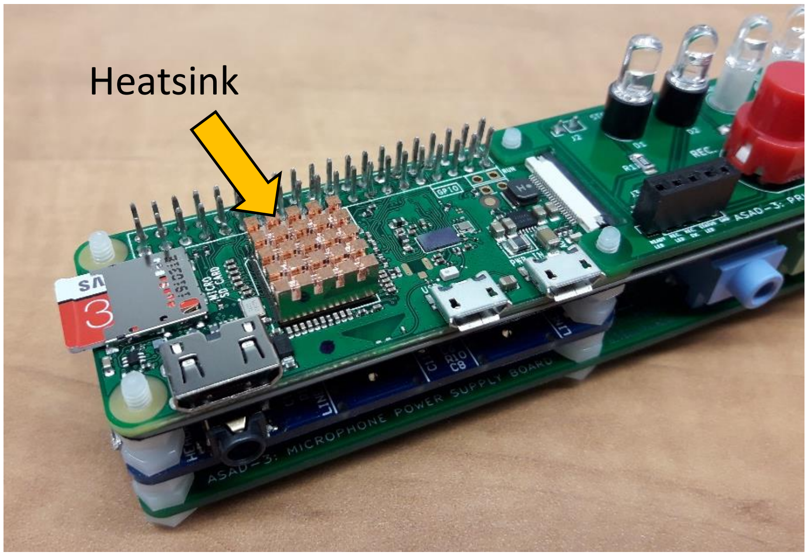

Figure 3.4. Copper heatsink adhered on the Raspberry Pi.

From a software perspective, a variety of Debian GNU/Linux based operating systems (OS) are capable of running on the Raspberry Pi, however for this project the Raspberry Pi OS v10 (Buster) was chosen for its widely known stability, support, and array of factory installed and supported software including the development and programming tools: Python 2/Python 3, Mathematica, Wolfram, Java, etc. The OS is installed on a microSD card which is inserted into the Raspberry Pi and from which the OS is accessed and run.

In addition to the primary OS running on the Raspberry Pi, a custom command-script was written in the Python Version 3.7 high-level computer programming language. The command-script controls all aspects of the functionality of the Audio Recorder including the display screen, push buttons, LED indicators, USB mounting/un-mounting, and most importantly the creation and closure of audio files. To automatically start and run the command-script each time the Raspberry Pi is booted, the command-script was added the directory "/etc/rc.local", which by default of the OS, runs at the start-up of the Raspberry Pi.

Audio information is stored in the WAV file format with 16-bit resolution at a sampling rate of 44,100 Hz. Prior to the analog-to-digital converter, the sampled signal passes through an anti-aliasing filter that removes frequencies above 22,000 Hz. Additionally, the resolution and sampling rate can be reduced within the command-script if desired. The WAV format was exclusively chosen as it does not apply any compression or other form of alteration to the original raw data comprising the audio signal. The stereo file format is utilized to store information from the 2 microphones in the left and right channels of the WAV file, respectively. The file structure of a WAV file is a subset of Microsoft's RIFF specification for media file structure, where a RIFF file is comprised of a file header (called a "RIFF chunk") followed by the recorded data. The structure for the entire WAV file is as noted in Table 3.3.1-1. A WAV file is similar in that the file is comprised of a "RIFF chunk" but has a "WAVE chunk" appended after. The "WAVE chunk" consists of two sub-chunks: the "fmt" sub-chunk and the "data" sub-chunk. More generally, the first 44 bytes of a WAV file can be described as the file header, after which is followed by the raw 16-bit binary data. The file header is used to specify details including the file type, sampling rate, resolution, file size, etc. The file header of a WAV file has the following format: (values shown are for a stereo WAV file format with 16-bit resolution at a sampling rate of 44,100 Hz).

Table 3.3.1-1. File Structure of Microsoft .WAV file format. Source: Adapted from [19].

Data Block	Offset (Bytes)	Size (Bytes)	Name	Value	Description
"RIFF" Chunk	0	4	ChunkID	"RIFF"	Contains the characters "RIFF", indicating the start of the "RIFF Chunk".
	4	4	ChunkSize	File Size	Size of the entire file not including: ChunkID and ChunkSize. Typically filled at file closure.
	8	4	Format	"WAVE"	Specifies the file format: .WAV.
Format Sub-Chunk	12	4	Subchunk1ID	"fmt "	Contains the characters "fmt ", indicating the start of the "Format Sub-Chunk" Must include trailing null (" ").
	16	4	Subchunk1Size	16	Size of the "Format Sub-Chunk" not including: Subchunk1ID and Subchunk1Size.
	20	2	AudioFormat	1	Type of format: 2 byte integer. PCM (uncompressed) = 1, values other than 1 describe some form of compression technique.
	22	2	NumChannels	2	Number of Channels: 2 byte integer. Mono = 1, Stereo = 2, etc.
	24	4	SampleRate	44100	Sampling Rate: 32-byte integer, in Hz.
	28	4	ByteRate	176400	= (Sampling Rate * BitsPerSample * Channels) / 8.
	32	2	BlockAlign	4	= (BitsPerSample * Channels) / 8.
	34	2	BitsPerSample	16	Resolution (bits per sample).
Data Sub-Chunk	36	4	Subchunk2ID	"data"	Contains the characters "data", indicating the start of the "Data Sub-Chunk".
	40	4	Subchunk2Size	File Size	Size of the "Data Sub-Chunk" not including: Subchunk2ID and Subchunk2Size.
	44 . . .		Data		Recorded sound data in raw 16-bit binary format continues to be stored here for the duration of the recording.

When a file is created, the file header is populated and filled with corresponding values as defined by the parameters of the command initiating the recording. In the Python command-script, the values are specified by the Linux command: "arecord –f cd" where "-f" specifies the option for format, and "cd" specifies the necessary parameters to populate the header for "CD quality recording", i.e., the parameters which explicitly define the 2-channel (stereo), 44,100 Hz sampling rate, 16-bit little endian data recording format. Also, during file creation, when the header is populated, the "ChunkSize" value is filled with a place holder value until the recording is stopped and the file is closed; at which point this value becomes updated with the size of the entire file.

The process of closing the file firstly stops the recording and halts additional data from being appended to the file. The final step in closing the file entails updating the "ChunkSize" field in the WAV header with the size of the entire file. It is necessary to perform this step last since prior to stopping the recording, the overall file size is not known.

Since once of the intended functions for the Audio Recorder is to record audio information approximately 8 hours in length, storing the information within a single, large file was impractical, and additionally, would exceed the 4 GB file size limitation (imposed by the 32-bit unsigned integer to indicate file size used in the file header). Instead, the command-script intelligently splits the audio file at pre-defined time intervals to create smaller and more manageable audio files.

When the push-button to begin an audio recording is initially pressed (let it be described as a recording event), the command-script firstly creates a directory folder on the USB flash drive into which all audio information for that recording event will be placed. The file folder name is identified as: “Recording Number X”, where X corresponds to the recording event number. The first time the push-button is pressed X will correspond to 1 and all audio files for that recording event will be contained in the directory folder “Recording Number 1”. If the first recording event is stopped (by pressing the push-button a second time) and then at some point later, if the push-button is pressed again (to begin another recording), a new directory folder will be created in which X will be 2. All audio files for the second recording event will then be contained in the directory folder “Recording Number 2”, while the directory folder “Recording Number 1” with its audio files will remain unchanged. The process of creating an additional sequential folder directory continues for as many times as a new recording event is commenced. An example of the file structure described is shown within Fig. 3.5, where it can be seen the Audio Recorder captured 4 different recording events and created 10 audio files within the first event (2.5 hours recorded).

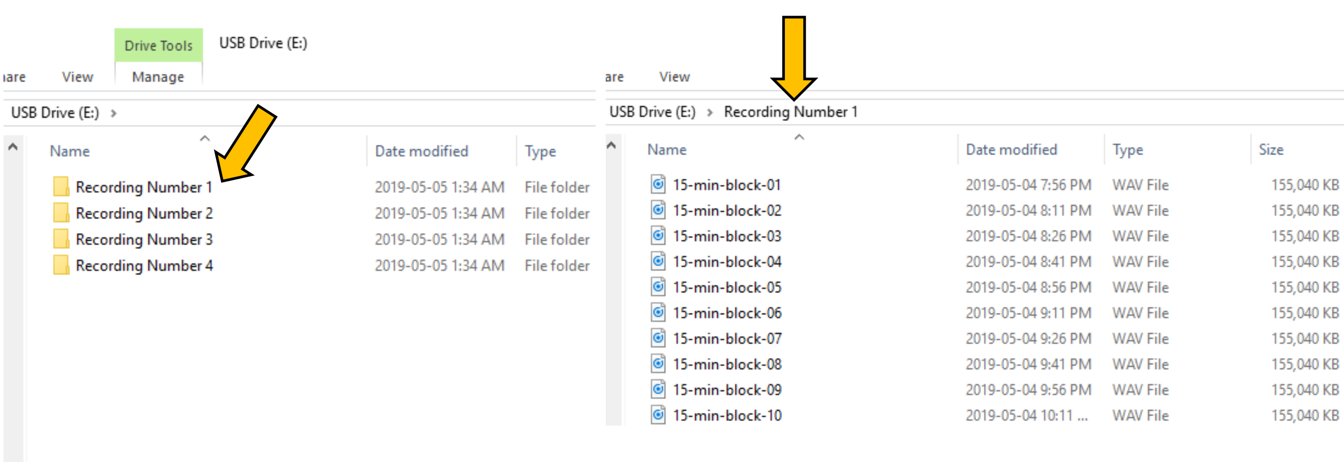

Figure 3.5. Directory folders (left) and Audio Files within the first directory folder (right), as recorded by the Audio Recorder.

Within each folder directory, as mentioned above, the recorded audio information is split into smaller, more manageable files. Without requiring any user intervention, the audio information is automatically split at 900-second (15-minute) intervals, where each audio file corresponds to 155,040 KB (0.155040 GB) in size. Once the audio file duration reaches 15 minutes, the command-script closes the current audio file while simultaneously opening a new file and continues to store audio information in files of duration 15 minutes until the recording event is stopped by the user. The process ensures that there is no loss of data between recording files, while also accomplishing the task of generating smaller, more manageable file sizes. Similar to the consecutive naming convention established by the folder directory creation relating to recording events, each 15-minute block of audio is named in a consecutive convention as well. 15-minute audio blocks are titled as “15-min-block(Y).WAV”; where Y identifies the consecutive block number. For example, when Y is 1 corresponds to the recording from time = 0 min. to time = 15 min., when Y is 2 corresponds to the recording from time = 15 min. to time = 30 min., and so on.

3.3.2. Audio Interface Board

As feature-rich as the Raspberry Pi is, interestingly, it does not include on-board is an analog-to-digital converter. Since the Raspberry Pi does not have an on-board analog-to-digital converter, and since the output of each of the two microphones is an analog output, digitization of the analog signal from the microphones is performed using an Audio Interface Board called the Fe-Pi Audio Z v2. The Audio Interface Board shares the same size and pin configuration as the Raspberry Pi Zero W and implements the well documented and high-quality SGTL5000 low power stereo codec to perform the analog-to-digital conversion. For the implemented design, the Audio Interface

Board samples the analog signal from the microphones at a rate of 44,100 Hz at 16-bit resolution and includes an anti-aliasing filter that removes frequencies above 22,000 Hz.

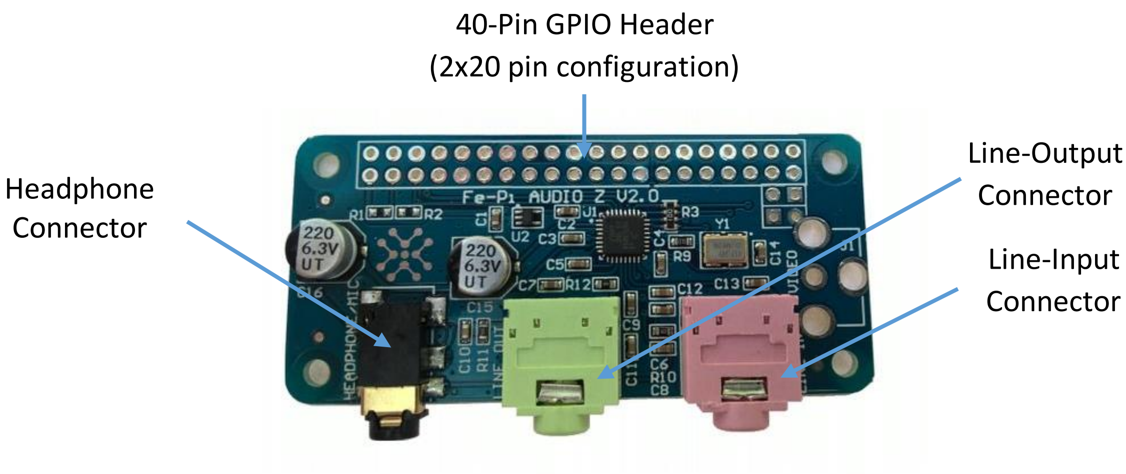

Figure 3.6. Fe-Pi Audio Z v2 shown in original, as purchased configuration. Source: Adapted from [50].

In the original configuration, the Fe-Pi Audio Z board features three individual female 3.5 mm connectors, for line-input, line-output, and headphone connections, as pictured in Fig. 3.6 above. The line-input connector permits a 2-channel (stereo) audio signal to be input to the board, the line-output connector permits a 2-channel (stereo) audio signal to be output to another device (i.e., a speaker), and the headphone connector permits the user to attach a set of 2-channel (stereo) headphones to simultaneously listen to the signals applied to the line-input channels in real-time.

To better meet with the desired purpose and design of the Audio Recorder, the Audio Interface Board was slightly modified from its original configuration. As a first alteration, the 3.5 mm female stereo connector corresponding to the line-input terminals was removed from the Audio Z circuit board. The two line-input terminals were required as the inputs to the ADC for the dual microphone channels, however the original style of connector on the board was not intended for use with dual microphones nor did it have a connection point to supply DC power to the microphones. Instead, the connection point (for power, ground, and the audio signals, respectively) of the two microphones was designed on the Microphone Power Supply Board, and the Microphone Power Supply Board routes the circuit traces for the audio signals to a position underneath the line-input terminals on the Audio Interface Board. In place of the original line-input connector, two male printed circuit (PC) pins (Manufacturer: Mill-Max Manufacturing Corp., Product Number: 800-10-020-10-002000) were affixed. The male PC pins were soldered to the left and right channels of the line-input conductors, respectively, on the Audio Z circuit board and permit a connection from the circuit traces for the audio signals on the Microphone Power Supply Board to supply the audio signals to the Audio Interface Board.

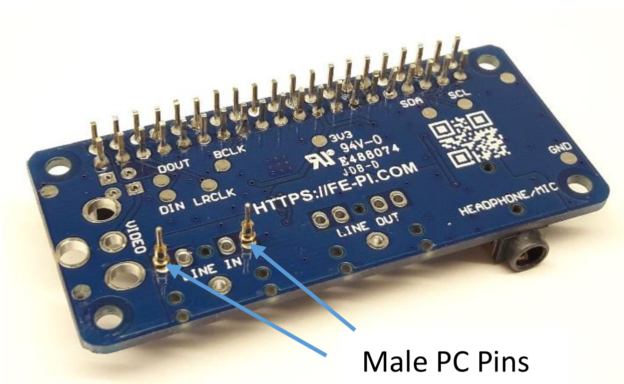

Figure 3.7. Underside of Fe-Pi Audio Z v2 showing the attachment of male PC pins to the left and right channels of the line-input terminal.

As the quality of audio signal must not be compromised, the style of the male PC pins, being a precision fitment, were specifically chosen to form a secure and extremely reliable connection with the female connector counterparts on the Microphone Power Supply Board. As well, the material finish of the PC pins, specifically their gold plating, is well known for its superior corrosion resistance and was hence chosen to once again permit a robust and reliable connection. The male

PC pins were attached such that they extend below the Audio Interface Board and seat firmly into the female connector counterpart when the Audio Interface Board is mounted on the Microphone Power Supply Board. The resulting connection established by the PC pins is compact, not bulky or protruding like the original connector, and additionally supports the use of dual-microphones and the setup with individual connection points required for each microphone, as shown on the Microphone Power Supply Board in Fig. 3.8:

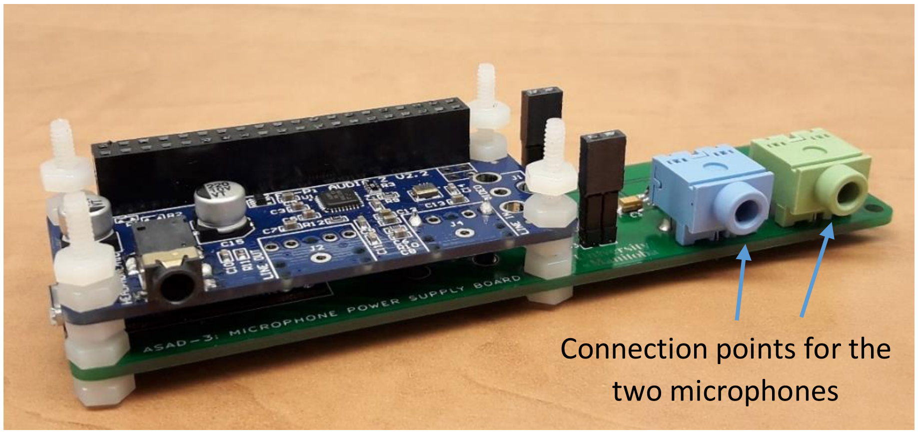

Figure 3.8. Fe-Pi Audio Z circuit board shown attached to the Microphone Power Supply Board where the male PC pins attached to the Audio Z board are seated in the female counterpart on the Microphone Power Supply Board.

The second modification to the Audio Interface Board was the removal of the line-output connector from the circuit board. The connector was removed since the line-output functionality would not be required in the final device and the position and style of the connector, protruding slightly from the audio interface board, would prevent the enclosure design to fit as close as possible to the electronic hardware.

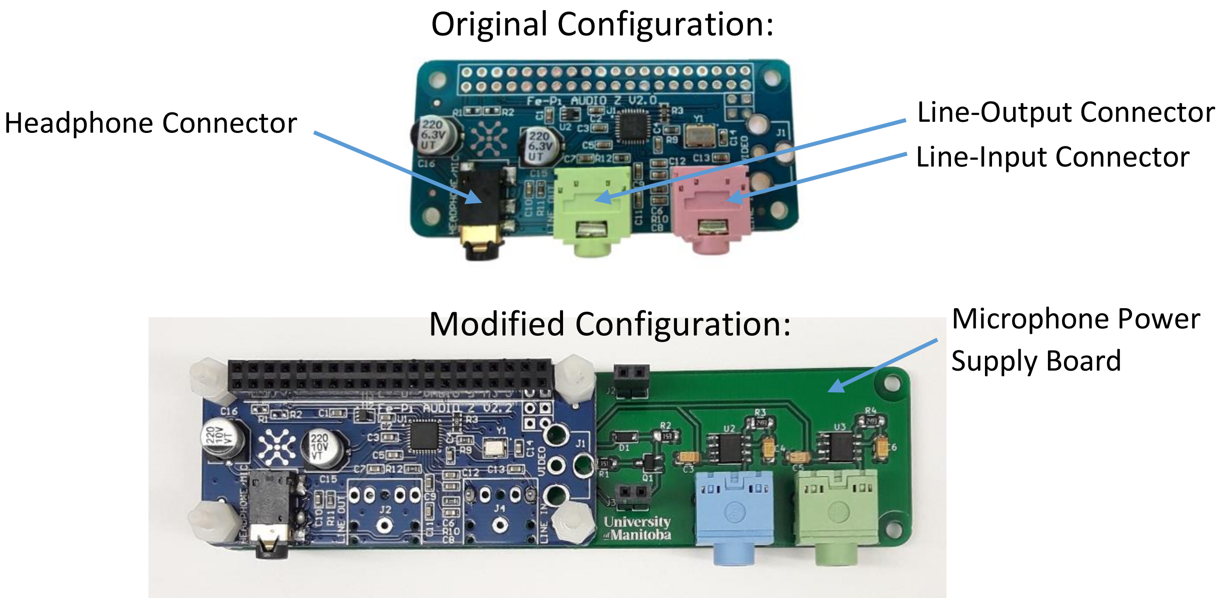

Figure 3.9. Modified Audio Interface Board shown with Microphone Power Supply Board installed below and extending to the right. Source: "Original Configuration" adapted from [50].

The final modification to the Audio Interface board is the addition of a 40-pin female stacking-header receptacle (Manufacturer: Adafruit Industries LLC, Product Number: 2223). The female receptacle was soldered to the 40-pin connector port of the Audio Interface Board (in a 2x20 configuration) to match the configuration of the male header pins installed on the Raspberry Pi connector. With an insulation height of 8.5 mm, the female stacking-header receptacle allows the Raspberry Pi to be mounted in a configuration above the Fe-Pi Audio Z with clearance to avoid contact with all the components of the Audio Interface Board. Similar to the male header pins installed on the Raspberry Pi, the female stacking-header receptacle on the Audio Interface Board has male pins (stacking pins) that extend below the receptacle which are physically connected to the contacts inside the receptacle. The stacking pins of the receptacle were installed such that the pins extend below the Audio Interface Board by approximately 5.0 mm and permit a connection to the Microphone Power Supply Board (via a female header socket installed on the Microphone

Power Supply Board). The installation of the stacking header receptacle is illustrated in the images of the Audio Interface Board shown in Fig. 3.10:

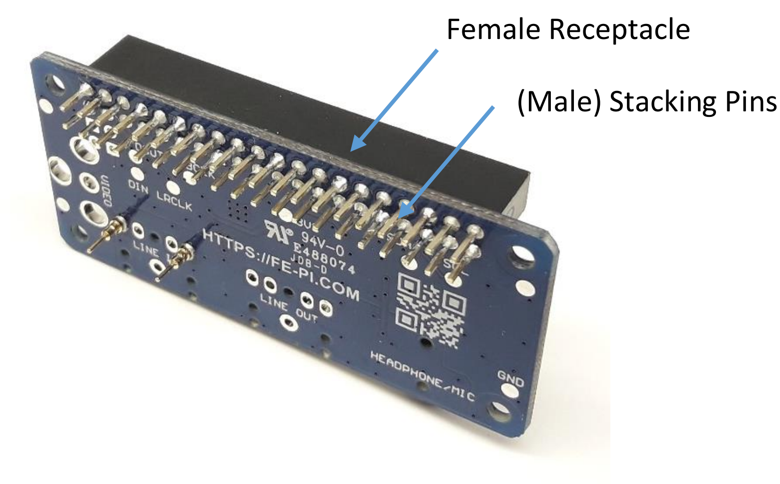

Figure 3.10. Fe-Pi shown with stacking header receptacle installed.

3.3.3. Microphone Power Supply Board

The electret condenser microphones chosen for this device are active electronic components and as such require a power source to operate the field-effect transistor (FET) comprising the internal circuit of the microphone. The microphone power supply board provides regulated DC power to the two peripheral microphones through the microphone cables to operate the active circuitry of each electret condenser microphone. The Microphone Power Supply Board circuit design is an original design and was hand fabricated utilizing a custom designed printed circuit board (PCB) (Dimensions: 30.0 mm x 116.8 mm x 1.6 mm) that spans the overall length and forms the bottom-most layer of the Audio Recorder. The Microphone Power Supply Board makes connections to the Raspberry Pi, Audio Interface Board, the Primary User Interface Board, and the two individual microphones.

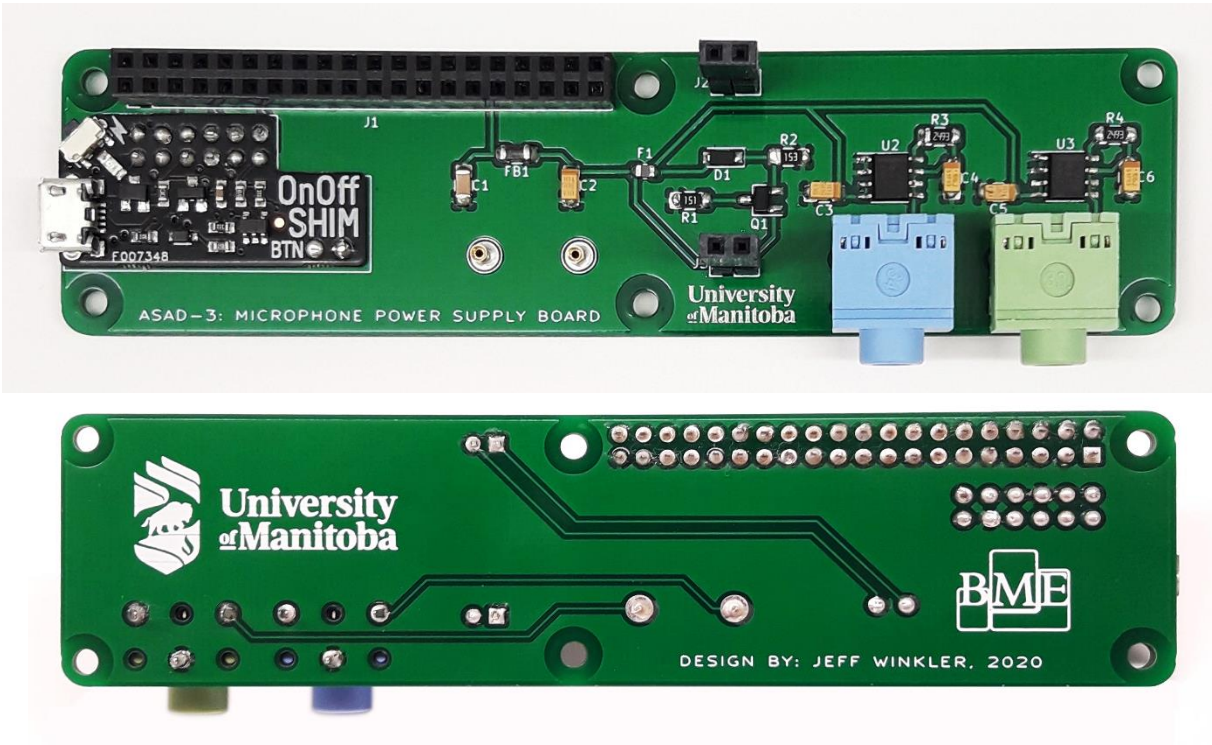

Figure 3.11. Microphone Power Supply Board showing top and bottom views of the circuit board.

Connections to the Raspberry Pi are established by means of a 40-pin female header receptacle (Manufacturer: Adafruit Industries LLC, Product Number: 2243) that contacts the Raspberry Pi through the 40-pin female stacking-header receptacle installed on the Audio Interface Board. The female receptacle was soldered to Microphone Power Supply Board (in a 2x20 configuration) to match that of the connector of the Raspberry Pi connector. With an insulation height of 4.5 mm, the female receptacle allows the Microphone Power Supply Board to be mounted in a configuration under the Audio Interface Board with clearance such that the components of the Microphone Power Supply Board are not in contact with the Audio Interface Board. The installation of the female receptacle is illustrated in the images of the Microphone Power Supply Board shown in Fig. 3.12:

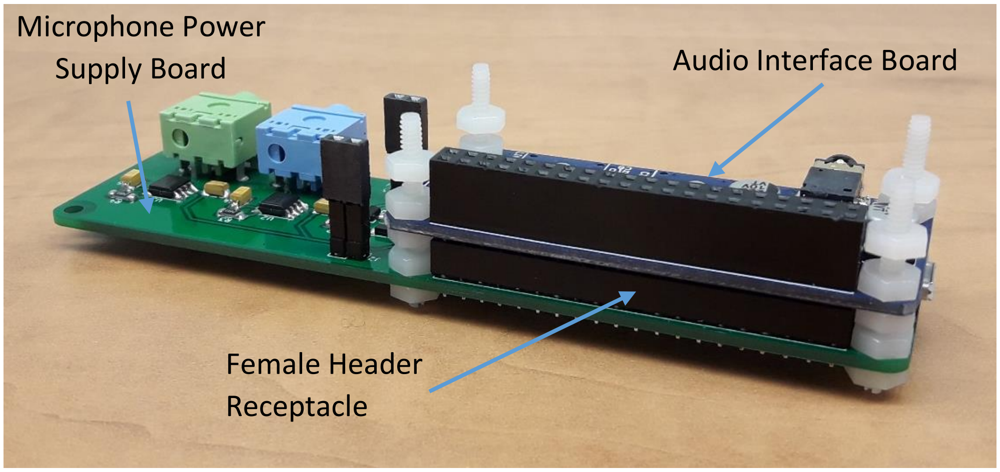

Figure 3.12. Audio Interface Board shown connected to Microphone Power Supply Board.

Connections to the Primary User Interface Board are established via two 2-position female socket connectors (Manufacturer: Samtec Inc., Product Number: ESQ-102-33-G-S, Insulation Height: 16.13 mm) installed on the Microphone Power Supply Board. The 2-position female socket connectors permit connectivity to the Primary User Interface Board to allow the functionality of the “ON/OFF” push-button (which communicates with the OnOff SHIM circuitry on the Microphone Power Supply Board) and the “FAULT” LED status indicator (which communicates with the transistor circuitry on the Microphone Power Supply Board).

The two external microphones connect to the Microphone Power Supply Board via two 3.5 mm female stereo connectors (Manufacturer: Kycon, Inc., Product Numbers: STX-3120-3B-284C & STX-3120-3B-577C) that are soldered to the Microphone Power Supply Board. The 3.5 mm female stereo connectors were chosen due to their high standard within the audio device industry for forming a secure, but removable connection and additionally for their ability to connect three individual channels per connector which matched the requirement necessitated by the microphones for a means to connect power, ground, and the audio signal.

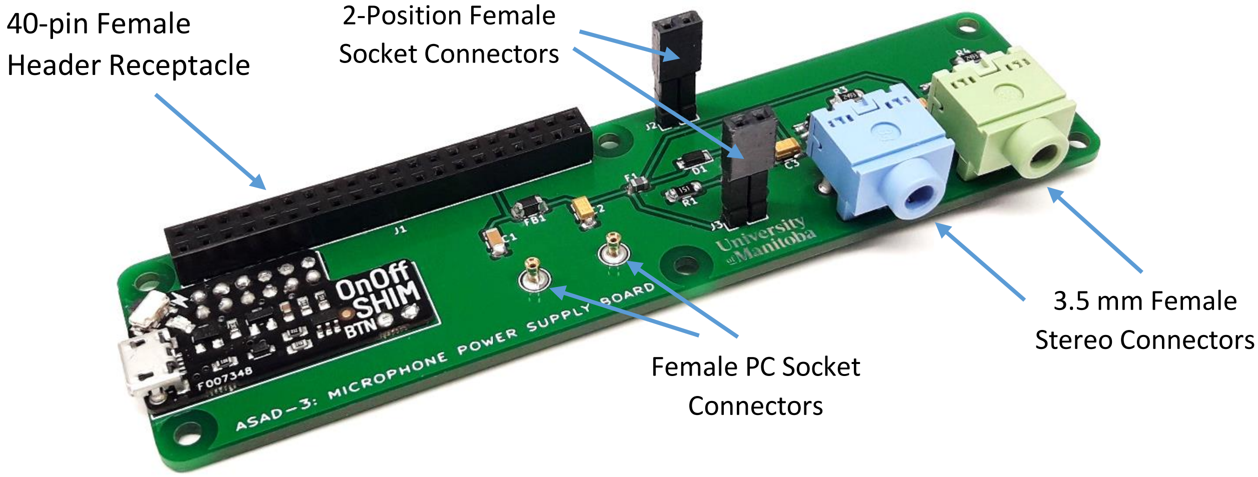

Figure 3.13. Microphone Power Supply Board with connection points illustrated.

As illustrated in Fig. 3.14, the common 3.5 mm male stereo connector has three separate terminals described as the tip, the ring, and the sleeve; commonly abbreviated as a TRS style plug. On the end of each cable connected to each respective microphone is a stereo TRS plug, further detailed within the microphone design described by Chapter 4 of this report.

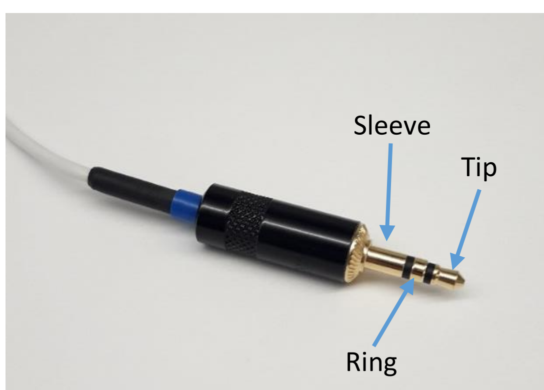

Figure 3.14. TRS (stereo) 3.5 mm plug with connections shown.

The two 3.5 mm female stereo connectors on the Microphone Power Supply Board permit for three individual connections to be made to each microphone, respectively. Filtered and regulated 3.3 V DC power is connected to the tip terminal of each female stereo connector, providing a connection point to provide the power supply for each of the two microphones. Additionally, connected to the sleeve terminal of each respective female stereo connector is ground, providing a reference voltage for each of the two microphones. Lastly, the ring-terminal of each female stereo connector serves as a connection point for the audio signal arising from each respective microphone. The polarity described for the female stereo connectors is complimentary to the polarity for the male stereo connector (present on the end of each microphone cable), such that each individual microphone thus forms three connections with the Audio Recorder for supply voltage, ground, and the audio signal. Figure 3.15 illustrates the two connections which permit the two microphones to connect to the Audio Recorder, respectively.

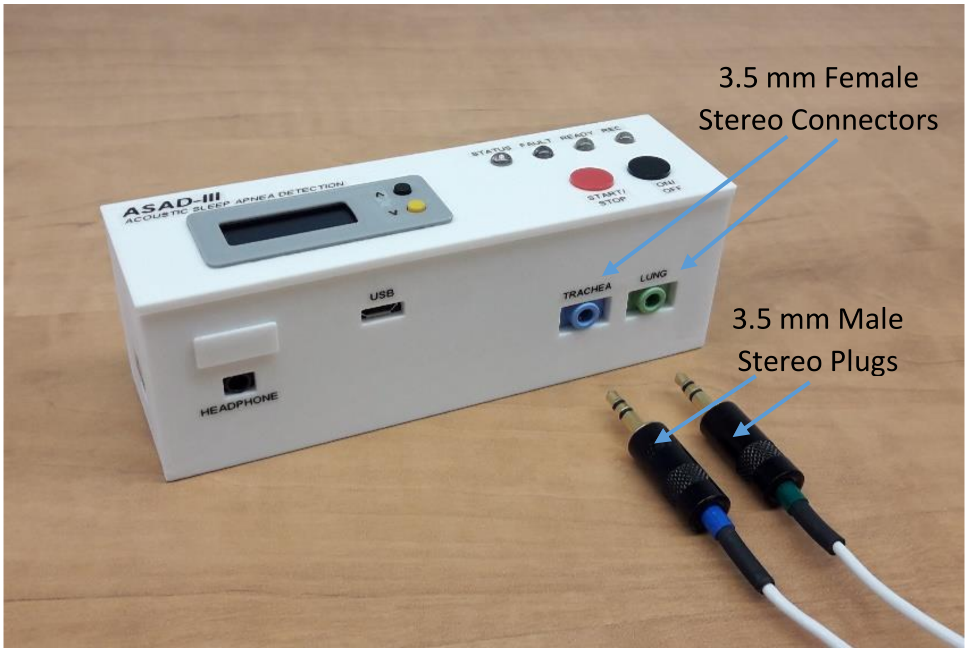

Figure 3.15. Microphone connectors with receptacles on Audio Recorder shown.

Lastly, and as mentioned previously, the Microphone Power Supply Board forms a connection to the Audio Interface Board using two female PC socket connectors (Manufacturer: Mill-Max Manufacturing Corp., Product Number: 310-13-164-41-001000) installed on the Microphone Power Supply Board. As the connection point for the audio signal from the two respective microphones is accomplished via the two 3.5 mm female stereo connectors, the Microphone Power Supply Board has circuit traces that route the audio signal from each respective 3.5 mm female stereo connector to each respective female PC socket connector. The female PC sockets connectors were attached such that they extend above the Microphone Power Supply Board and seat firmly into the male connector counterpart when the Audio Interface Board is mounted on the Microphone Power Supply Board.

3.3.3.1. Power Supply Filter

It was realized that powering the microphones directly via the 5 V power supply BUS of the Raspberry Pi resulted in an audio signal contaminated with high-frequency noise, even when recording in a silent environment. As the microphones are active components, fluctuations in the power supply voltage to the microphones caused artifacts in the audio signal. Upon investigation, the noise was realized to be roughly correlated to the processor load, i.e., higher loads on the processor resulted in a higher probability of noise present in the audio signal. Next, the 3.3 V power supply BUS of the Raspberry Pi was considered, where it was determined to be considerably less contaminated, with smaller fluctuations than the 5 V BUS.

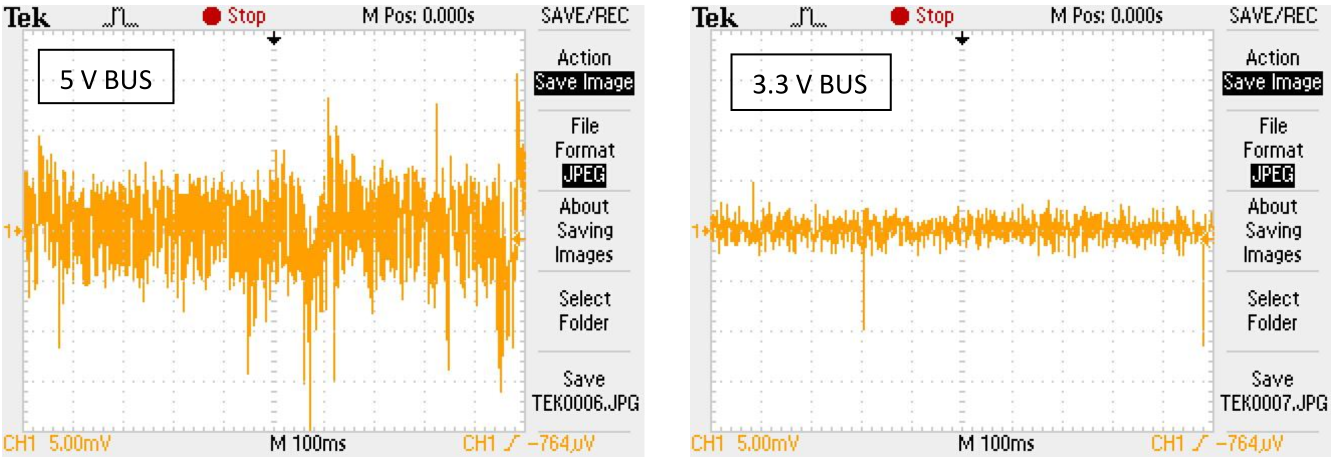

Figure 3.16. Comparison of the noise contamination on the Raspberry Pi Zero W 5 V BUS (left) vs. the 3.3 V BUS (right). Both plots show 5.00 mV divisions vertically, 100 msec divisions horizontally.

As can be noted in Fig. 3.16, the 5 V BUS has noise contamination showing large fluctuations with amplitude surpassing +/- 5 mV (on average) with occasional fluctuations of +/- 10 – 15 mV, whereas the 3.3 V BUS only experiences roughly +/- 2 mV amplitude noise contamination (on average) however still contains several occasional fluctuations of roughly +/- 10 mV. Even as such, the 3.3 V BUS shows roughly a 60% decrease in overall contamination as compared to the 5 V BUS. Since the 3.3 V power supply BUS of the Raspberry Pi was determined to be the least noisy power source available, it was hence utilized as the initial source of power for driving each of the two respective microphones.

The first stage of the Microphone Power Supply Board thus consists of a power supply filter. Sourcing power initially from the 3.3 V power supply BUS of the Raspberry Pi, the power supply is next filtered by the power supply filter; a low-pass filter consisting of an inductor and capacitor (LC-configuration) to remove remaining noise contamination from the 3.3 V power supply BUS.

An image of the implemented filter is provided in Fig. 3.17 where the complete circuit diagram for the filter is shown in the Appendix, Section 8.7.

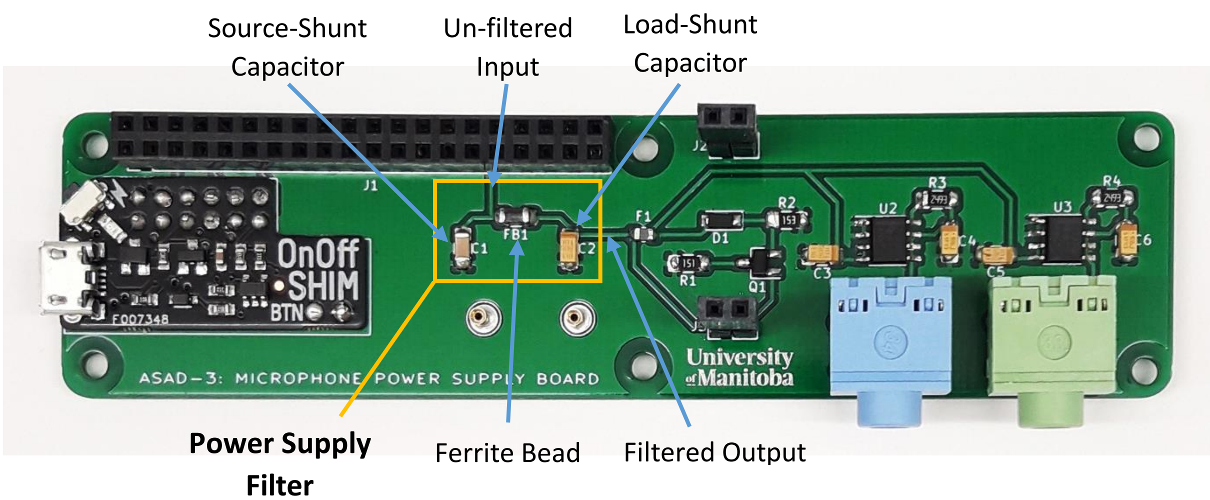

Figure 3.17. Microphone Power Supply Board with Power Supply Filter outlined.

The filter design was adapted from the Future Technology Devices International Ltd. Application Note: AN_146 titled: USB Hardware Design Guidelines for FTDI ICs [20]. The filter design incorporates a ferrite bead in series with the load and two separate capacitors, the first of which in shunt with the source, the second in shunt with the load.

For the implemented filter, a ferrite bead (Manufacturer: Taiyo Yuden, Product Number: FBMH3216HM221NT, Impedance: 220 Ohms @ 100MHz) along with capacitor (Manufacturer: KEMET, Product Number: C1206C103JARACTU, Capacitance: 10 nF) in shunt with the source (i.e., Raspberry Pi) and capacitor (Manufacturer: KEMET, Product Number: T491A104M035AT, Capacitance: 100 nF) in shunt with the load (i.e., Microphone Power Supply) were utilized.

The filter is able to reduce high noise contamination in the power signal yet pass DC components of the signal due to the configuration of the components and the differing electrical reactance of the various components. Electrical reactance is a measure that quantifies a components opposition to a change in current or voltage as a result of the inherent capacitance or inductance of the given component. The mathematical expression for the reactance of an inductor is described by Eq. 1:

Inductor Reactance $X_L = 2\pi f L$ (Eq. 1)

where X_L is the reactance (in Ohms) of the inductor, f is the frequency (in Hz) of the signal applied to the inductor, and L corresponds to the inductance value of the inductor. As can be inferred from the equation above, the ferrite bead (inductor) permits low frequency (i.e., DC) components of the applied signal to pass since the reactance of the ferrite bead at low frequencies is very small, however at larger frequencies, the reactance of the inductor increases (proportional to an increase in frequency), effectively blocking the signal due to the high reactance.

Conversely, the mathematical expression for the reactance of a capacitor is described by Eq. 2:

Capacitor Reactance $X_C = \frac{1}{2\pi f C}$ (Eq. 2)

where X_C is the reactance (in Ohms) of the capacitor, f is the frequency (in Hz) of the signal applied to the capacitor, and C corresponds to the capacitance value of the capacitor. As can be inferred from the equation above, the capacitor permits AC components of the applied signal to pass since the reactance of the capacitor decreases (proportional to an increase in frequency), however at very low frequencies (i.e., DC), the reactance of the capacitor is very large effectively blocking the signal due to the high reactance.

By configuration of the filter components then, the ferrite bead acts to pass DC components of the signal from the 3.3 V power supply BUS, but blocks the AC components (i.e., fluctuations in the 3.3 V signal). Conversely, the capacitors in shunt with the source and load, respectively, provide a path for the AC components of the signal from the 3.3 V power supply BUS to ground, but appear as an open-circuit to DC components of the signal and hence further act to remove high-frequency fluctuations from the 3.3 V power supply BUS. The result of the Power Supply Filter is indicated by the plots shown in Fig. 3.18:

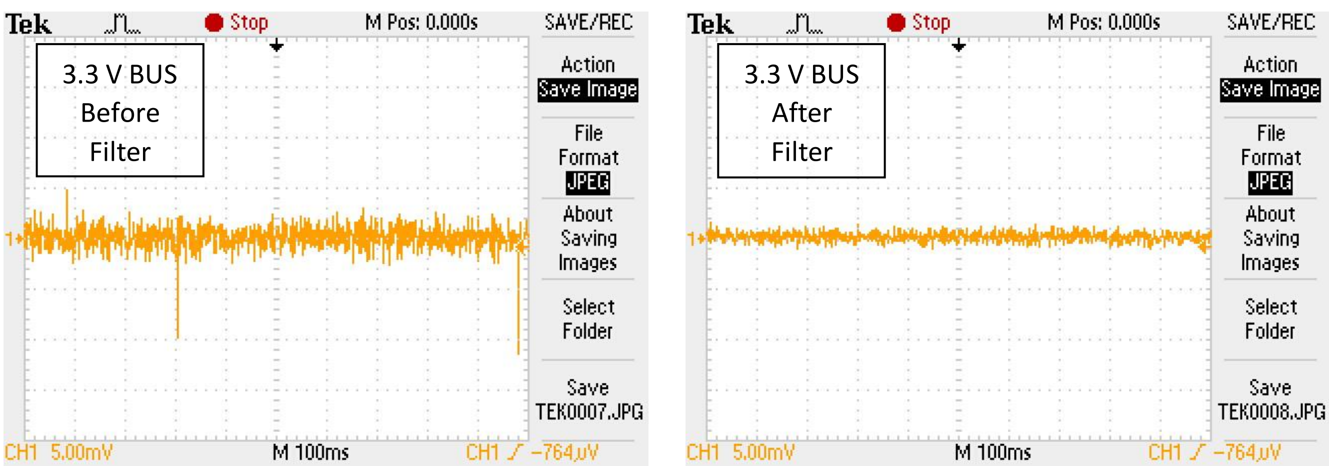

Figure 3.18. Comparison of the noise contamination on the Raspberry Pi Zero W 3.3 V BUS before filtering (left) vs. after applying the Power Supply Filter (right). Both plots show 5.00 mV divisions vertically, 100 msec divisions horizontally.

The plots in Fig. 3.18 show the 3.3 V BUS both before and after the Power Supply Filter. The effect of the Power Supply Filter is easily noticed; namely the minor fluctuations in the 3.3 V BUS are reduced from +/- 2 mV (on average) to roughly +/- 1 mV on average, with all major fluctuations on the signal completely removed after the filter.

One additional source of noise leading to artifacts in the audio signal became evident when using the Raspberry Pi with wireless networking (i.e., Wi-Fi) turned on. Specifically, high-frequency noise was observed on the audio signal correlated to network usage, i.e., higher network usage resulted in a higher probability of noise present in the audio signal. As one of the criteria for mounting the Audio Interface Board involved keeping the communication lines short, this also had the effect of placing the Wi-Fi antenna of the Raspberry Pi very near to, and directly above that of the Audio Interface Board. Due to the proximity, when the Wi-Fi antenna of the Raspberry Pi is in use it was found that the radiated energy from the said antenna was introducing artifacts on the audio signal. Although the Audio Recorder device in its current state does not require the wireless networking feature and the issue could have been mitigated by keeping the feature turned off, it was instead decided to combat the issue to permit future development that could see the Audio Recorder utilize the benefits offered by wireless connectivity.

A solution was thus developed to reduce the interference on the Audio Interface Board, but still permit wireless connectivity on the Raspberry Pi. To prevent the radiated energy from the Wi-Fi antenna of the Raspberry Pi from introducing noise on the Audio Interface Board, a flexible sheet of powdered ferrite (Manufacturer: Laird-Signal Integrity Products, Product Number: MHLL12060-200, Thickness: 0.20 mm) was inserted in-between of the bottom of the Raspberry Pi and the top of the Audio Interface Board, as shown in Fig. 3.19:

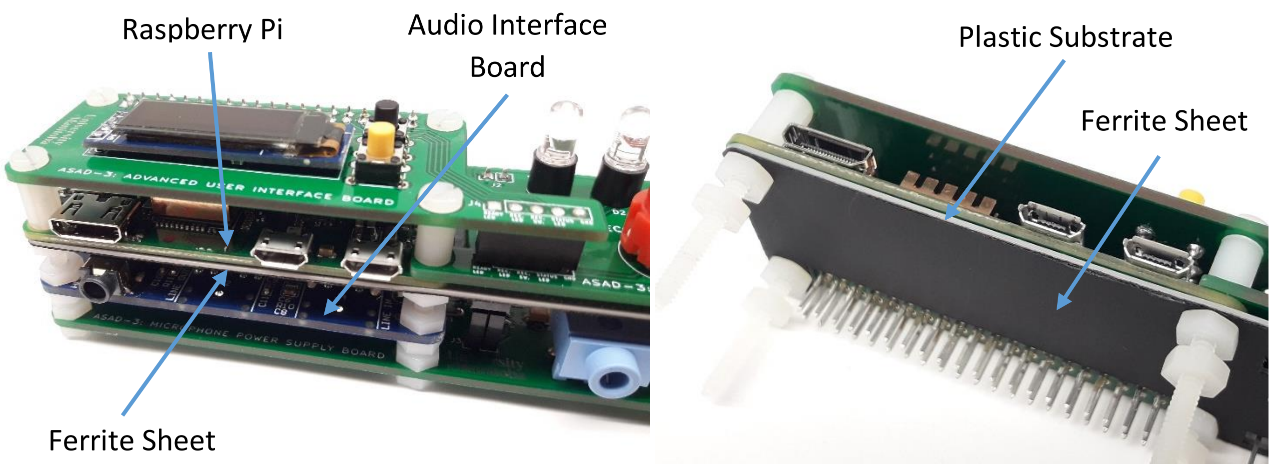

Figure 3.19. Audio Recorder with ferrite sheet installed between the Raspberry Pi and the Audio Interface Board.

The ferrite sheet works by absorbing the radiated energy from the antenna and hence shields the Audio Interface Board from the radiated energy. Since the ferrite sheet is placed below the Raspberry Pi, it effectively blocks the radiated energy from the sensitive electronic circuits mounted on the Audio Interface Board below the Raspberry Pi, yet still allows the Wi-Fi antenna to radiate in the upper-plane (above the ferrite sheet) and hence still able to maintain wireless connectivity.

The ferrite material comes as a thin, flexible, self-adhesive sheet. To provide strength and a method to mount the material between the appropriate circuits, the ferrite material was adhered to a piece of plastic substrate (Material: polylactic acid (PLA), Thickness: 1.0 mm). The plastic substrate was custom-designed, and 3D printed to match the contours of the circuit with provisions for header-pin connectors, while spanning the length of the device to provide shielding for all circuits below the Raspberry Pi. The ferrite-sheet, adhered to the plastic substrate spanning the length of the Audio Recorder is pictured in Fig. 3.20:

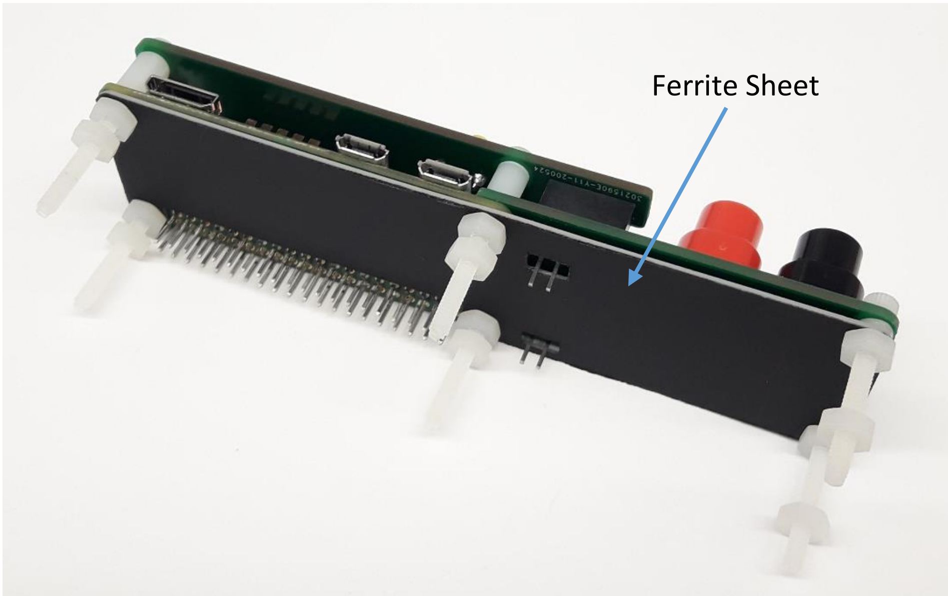

Figure 3.20. Audio Recorder with lower circuits removed showing the installation of the ferrite sheet spanning the overall length with provisions for connectivity.

3.3.3.2. Fault Protection Circuit

Since the two microphones are required to be affixed on the surface of the skin during recording, it is imperative the safety of the user is maintained for all possible scenarios. Thus, following the Power Supply Filter, supply power for the microphones next passes through a Fault Protection Circuit consisting of a resettable fuse that will be tripped if there is a fault, i.e., a short circuit where a high current flows between power and ground supplied to the microphones. The resettable fuse (Manufacturer: Murata Electronics, Product Number: PRG21AR220MS1RK, Trip Current: 195 mA) is a two-terminal device (input and output), the input of the fuse is connected to the output of the Power Supply Filter, whereas the output of the fuse is connected to the input of the Voltage

Regulation Stage. In the event of a short circuit with the microphone or microphone connection leads, the placement of the fuse will immediately and automatically disconnect power from both microphones.

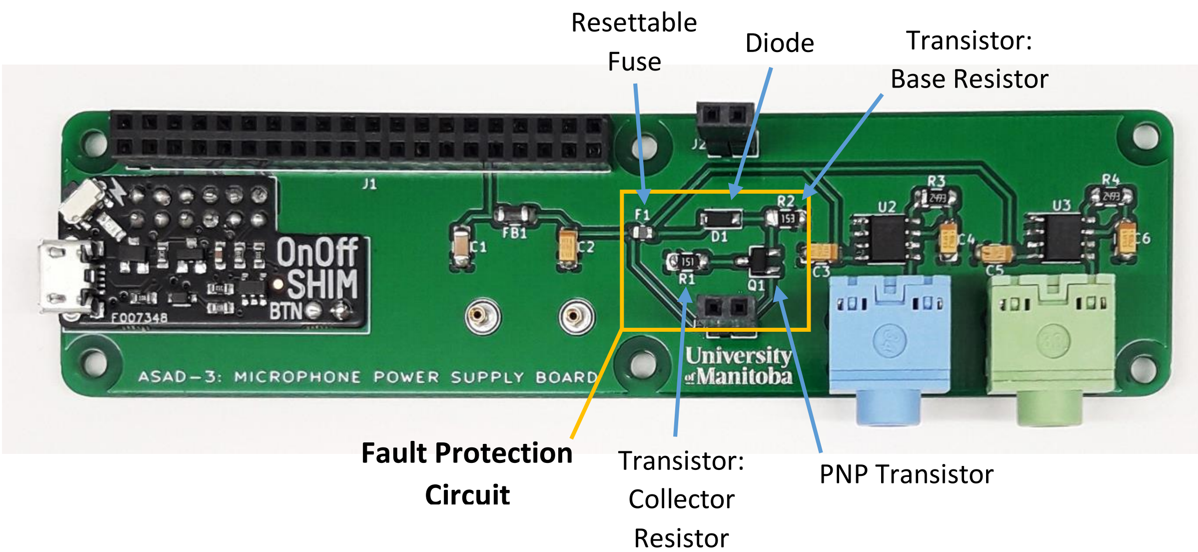

Figure 3.21. Microphone Power Supply Board with Fault Protection Circuit outlined.

The chosen fuse has a hold current value of 75 mA (at +25 °C) capable of supporting the normal demands of the Voltage Regulation stage of the Microphone Power Supply Board with both microphones attached and powered on, yet with sufficient headroom to allow for fluctuations in the demand without erroneously causing the fuse to trip.

Additionally, the Fault Protection Circuit employs an LED indicator that will illuminate and thus notify if there has been a fault and the fuse has been tripped. The "FAULT" LED indicator is controlled by a circuit consisting of a PNP transistor (PNP indicating a transistor with one n-type material doped with two p-type materials) (Manufacturer: Diodes Incorporated, Product Number: ZXTP19100CFFTA), diode (Manufacturer: Diodes Incorporated, Product Number: 1N4148W-7-

F), 150 Ω resistor (Manufacturer: Yageo, Product Number: RC1206JR-07150RL), 15 kΩ resistor (Manufacturer: Yageo, Product Number: RC1206JR-0715KL), and LED (Manufacturer: Adafruit Industries LLC., Product Number: 2700). The fuse protection circuit is shown in analogous form by Fig. 3.22 with the full circuit diagram for which is shown in the Appendix, Section 8.7.

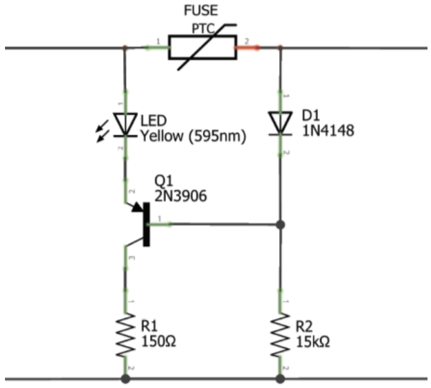

Figure 3.22. Fault Protection Circuit

The transistor utilized in the circuit is a three terminal device having the terminals of emitter (E), base (B), and collector (C) as indicated in Fig. 3.23:

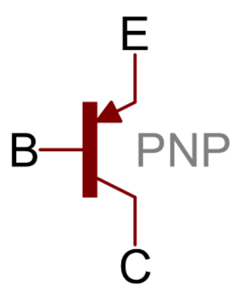

Figure 3.23. PNP transistor circuit element with pins labelled. Source: [45]

The transistor is utilized as a switch to turn the LED indicator on when the fuse has been tripped based upon the operating principle of the transistor. Principally, the current that can flow from the emitter to the collector is controlled by the base terminal; where the voltage (potential) difference between the emitter and the base controls the behaviour of the transistor. If the potential of the emitter is 0.7 V or greater than the potential of the base, current flows from emitter to collector. If, however the potential of the emitter is less than 0.7 V above the potential of the base, no current flows from the emitter to collector.

Thus, in the implemented configuration shown in Fig. 3.22, when the fuse is conducting (i.e., it has not been tripped), there is a path for the 3.3 V supply to both the emitter and base, thus the potential of the emitter is equal to the potential of the base and hence no current can flow from the emitter to collector. As a result, there is no path for current flow through the LED indicator and it remains unlit. When the fuse has been tripped however, the path for 3.3 V to the base is broken and the potential at the base becomes approximately 0 V. There is still a path for the 3.3 V supply to the emitter such that the potential difference between the emitter and base is greater than 0.7 V. As a result, current can now flow from the emitter to the collector, providing a path for current to flow through the LED indicator and hence the LED is illuminated. The 150 Ω resistor limits the current through the resistor such that the LED is not damaged with excessive current when lit. The 1N4148 diode ensures the current flowing out of the base can only flow to ground while the 15 kΩ resistor ensures said current to ground remains small.

3.3.3.3. Voltage Regulation

Provided that the resettable fuse has not been tripped, the power from the output of the power supply filtering stage flows through the fuse and is then split and provided to dual, low-dropout linear voltage regulators (Manufacturer: Texas Instruments, Product Number: TPS7133QDR), each respective regulator to power each of the two microphones independently. In addition to the power supply filter, the addition of the dual, low-dropout linear voltage regulators were implemented to further ensure that the supply voltage to each respective microphone is maintained at a steady 3.3V without large artifacts arising from fluctuations in the 3.3 V power supply BUS on the Raspberry Pi. Although a single voltage regulator could have been implemented to power both microphones; the dual voltage regulator setup was chosen to isolate the two supplies where the demand on one supply would not directly affect the other and vice versa.

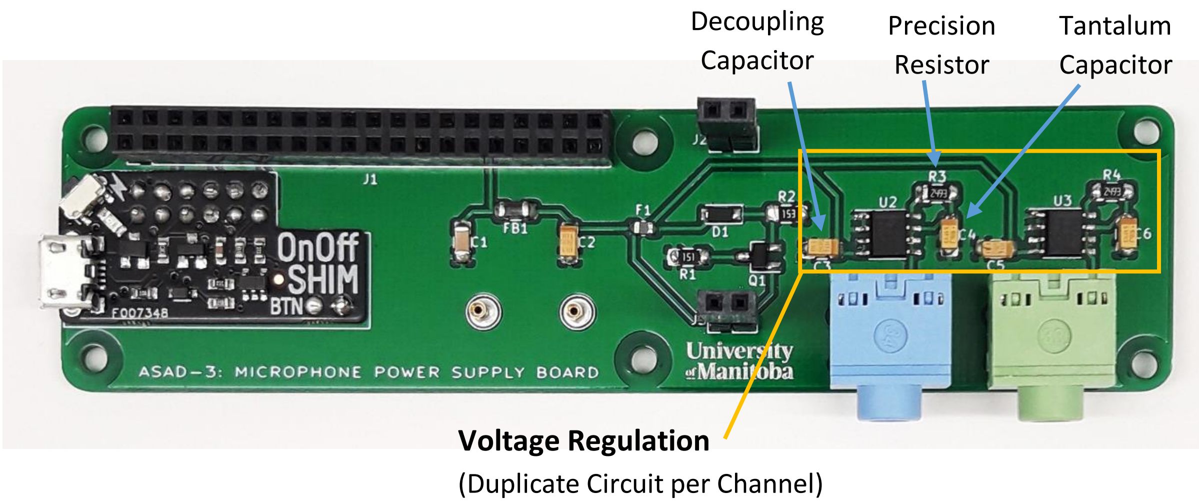

Figure 3.24. Microphone Power Supply Board with Voltage Regulation Circuit outlined.

The voltage regulators are implemented using the recommended circuit provided in the application information section of the regulator datasheet where each regulator utilizes a tantalum capacitor (Manufacturer: AVX Corporation, Product Number: TAJA106K006SNJ, Value: 10 uF) and precision resistor (Manufacturer: Yageo, Product Number: RT1206BRD07249KL, Value: 249 kOhm, 0.1% tolerance, 1/4 W). The schematic illustrating the implementation of each respective voltage regular can be found in the Appendix, Section 8.7. Additionally, each voltage regulator circuit implements a decoupling capacitor (Manufacturer: KEMET, Product Number: T491A104M035AT, Value: 0.1 uF) mounted as close as possible to the input pin of the voltage regulator to further help reduce noise and stabilize the input voltage.

3.3.3.4. OnOff SHIM

By default, the Raspberry Pi does not have an on/off switch and when used as a single board, initiates the start-up procedure immediately when a 5 V power supply is connected to the on-board micro-USB power supply connector. Additionally, the shutdown and power off process of the Raspberry Pi is a critical procedure since corruption of the OS can occur when power to the Raspberry Pi is abruptly halted instead of the proper shutdown technique used. Normally, when used in the single-board configuration, the user would be utilizing a mouse and monitor to navigate the desktop environment and would select the shutdown option through the main menu on-screen. Since a desktop environment is unnecessary for the intended purpose of the device, an alternative solution was implemented to easily power on and off the Raspberry Pi.

The OnOff SHIM (Manufacturer: Pimoroni, Product Number: PIM269) is a circuit component having a 5 V micro-USB connector for power input and monitors the state of an external push-button to latch and un-latch the 5 V power supply to the power input to the Raspberry Pi. Additionally, prior to un-latching the power supply, the OnOff SHIM signals the Raspberry Pi to initiates a shutdown procedure when wanting to turn off the device. The OnOff SHIM has on-board contacts for attaching an external normally-open, momentary switch. The attached switch, when pressed, connects to the two contacts effectively signalling the OnOff SHIM to turn on, or turn off, the Raspberry Pi.

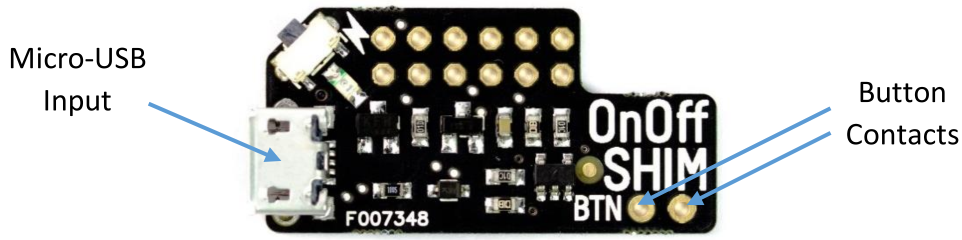

Figure 3.25. OnOff SHIM shown in original, as purchased configuration. Source: Adapted from [48].

The OnOff SHIM was installed on the left side of the Microphone Power Supply Board with the micro-USB connector easily accessible. When a battery or other 5V DC power supply is connected to the micro-USB power input of the OnOff SHIM, pressing the "ON/OFF" push-button latches the 5 V power supply from the micro-USB input to the Raspberry Pi and initiates the boot procedure for the OS to load onto the Raspberry Pi. Similarly, once the OS is loaded, pressing the "ON/OFF" push-button again initiates a shut-down procedure that unlatches the 5 V power supply from the Raspberry Pi by pulling GPIO/BCM pin 4 low after the shut-down sequence concludes with the overall result of completely removing power from the Raspberry Pi.

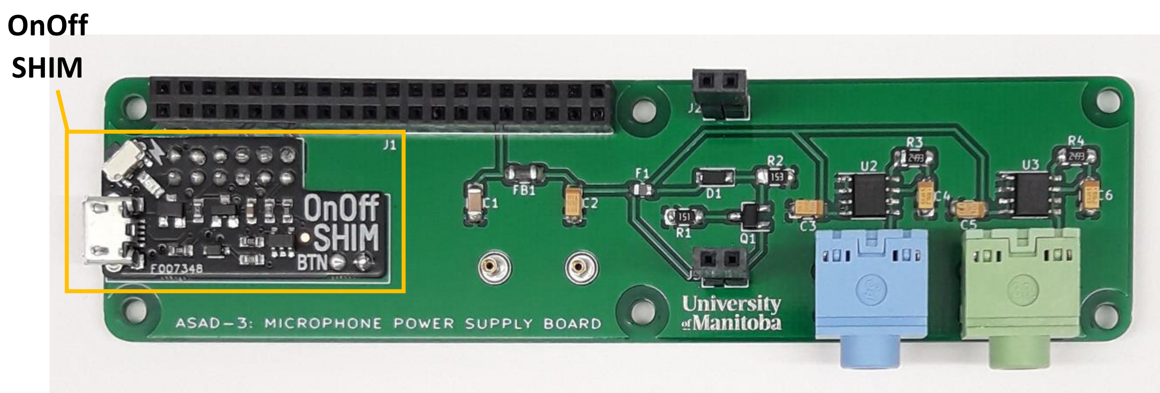

Figure 3.26. OnOff SHIM installed on Microphone Power Supply Board.

3.3.4. User-Interface Boards

To control the recording device Audio Recorder and provide feedback about system status and the recording progress there are two user-interface boards that communicate with the Raspberry Pi; identified as the Primary User Interface Board and the Advanced User Interface Board, respectively, they are indicated in Fig. 3.27:

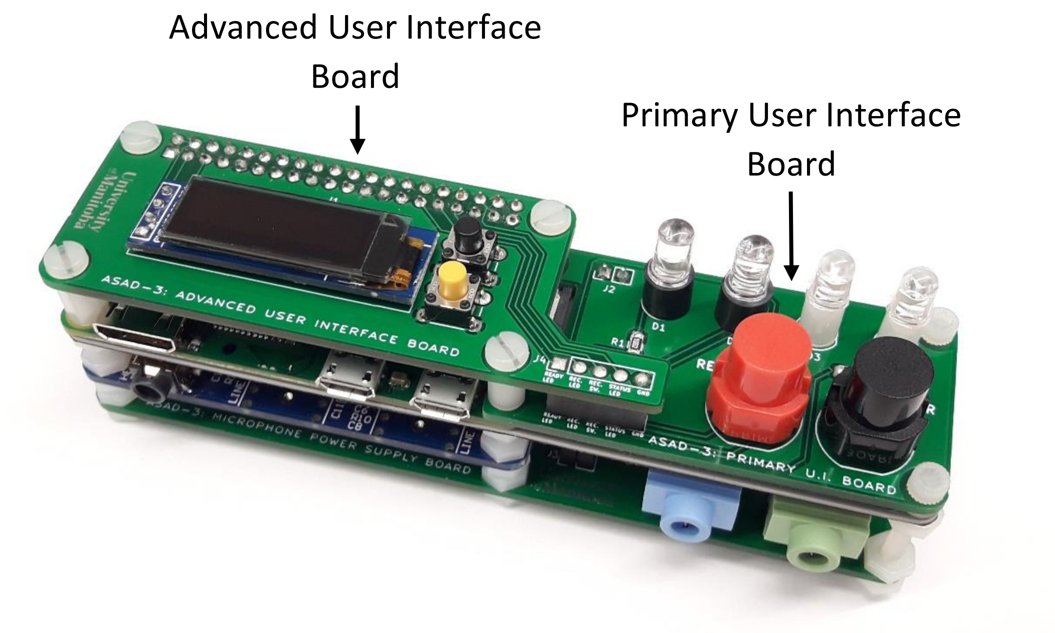

Figure 3.27. Top view of Audio Recorder with Primary and Advanced User Interface Boards illustrated.

The Primary User Interface Board is critical to control all functions of the device and provides the necessary system status feedback utilizing simple LED indicators. The Primary User Interface Board circuit design is an original design and was hand fabricated utilizing a custom designed printed circuit board (PCB) (Dimensions: 30.0 mm x 57.8 mm x 1.6 mm). To keep overall dimensions constrained to a minimum, the Primary User Interface Board is positioned adjacent to the Raspberry Pi and the end of the PCB is finished to accurately match the profile of the Raspberry Pi board to enable a secure and close-fitting overlap when assembled.

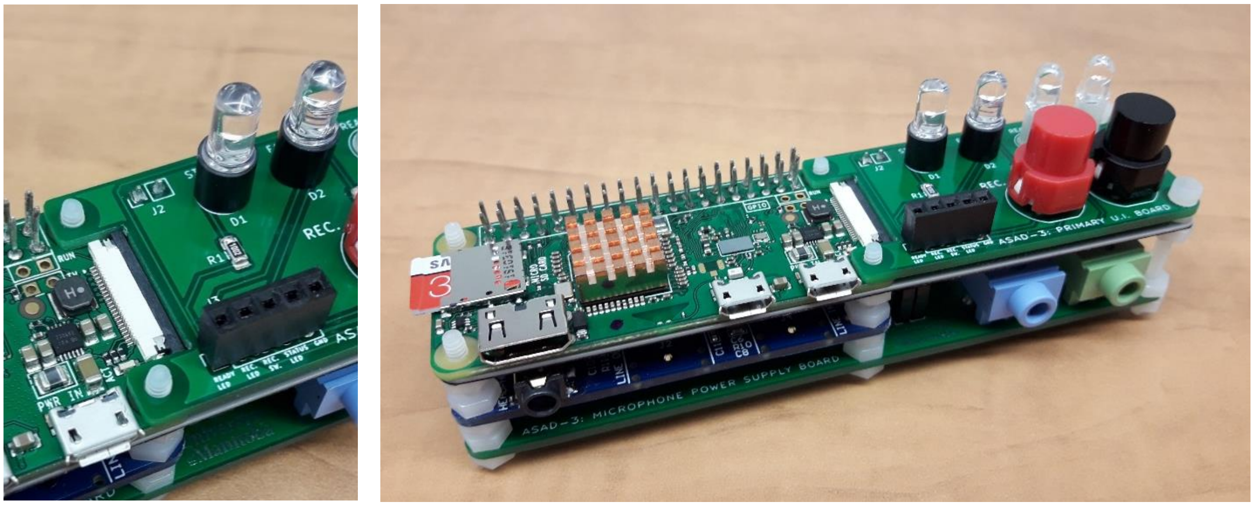

Figure 3.28. Illustration of fit-up of Primary User Interface Board to Raspberry Pi (left) and overall view of the Audio Recorder with Advanced User Interface Removed (right).

The Advanced User Interface Board is utilized to control advanced device features and display in-depth system feedback. The Advanced User Interface Board is positioned directly on top of the Raspberry Pi with a small extension of the PCB that overlaps the Primary User Interface Board. The extending section of the Advanced User Interface Board provides a connection point for the Primary User Interface Board to connect with the Advanced User Interface Board. The connection point between the two interface boards is implemented using a 5-pin header pin connector to connect five circuit traces from the Primary User Interface Board to the Advanced User Interface Board. After the connection formed by the 5-pin header, the circuit traces originating from the Primary User Interface Board are then routed to the appropriate pins of the 40-pin header connector on the Advanced User Interface Board to permit connectivity of the Primary User Interface Board with the Raspberry Pi. The choice of position for the Primary User Interface Board, adjacent to the

Raspberry Pi as opposed to stacked on top/below, avoided the necessity to add another 40-pin header socket to make connectivity to the Raspberry Pi which would have made the device unnecessarily tall. Additionally, the choice of position for the Primary User Interface Board was permitted since high-frequency communication between the Raspberry Pi and the Primary User Interface Board was not required and hence latency (and thus length of conductor) was of no concern.

The Advanced User Interface Board circuit design is an original design and was hand fabricated utilizing a custom designed printed circuit board (PCB) (Dimensions: 30.0 mm x 81.5 mm x 1.6 mm). Installed on the Advanced User Interface Board are several components: an OLED display screen, two push buttons, and a 40-pin female header socket that plugs into the male header pins of the Raspberry Pi. The OLED display communicates with the Raspberry Pi via the I^2C communication protocol and is connected to GPIO/BCM pins 2 and 3 of the 40-pin header socket for connecting to the serial data (SDL) and serial clock (SCL) pins of the Raspberry Pi. Additionally, the OLED display is connected to the 40-pin header socket for connecting to the 5 V and ground pins of the Raspberry Pi; the 5 V power supply was used in favor of the 3.3 V supply to limit the number of devices and hence avoid added noise on the 3.3 V BUS. The two push buttons on the Advanced User Interface Board are also connected to the 40-pin header socket and connect to GPIO/BCM pins 25 and 26 of the Raspberry Pi.

As mentioned above, the Primary User Interface Board first interfaces with the Advanced User Interface Board which then enables the Primary User Interface Board to connect with the Raspberry Pi. Specifically, the 5-pin header pin connector (Manufacturer: TE Connectivity AMP

Connectors, Product Number: 5-535541-3) permits the Primary User Interface Board to make a connection with GPIO/BCM pins 5, 6, 13, 16, and ground of the Raspberry Pi.

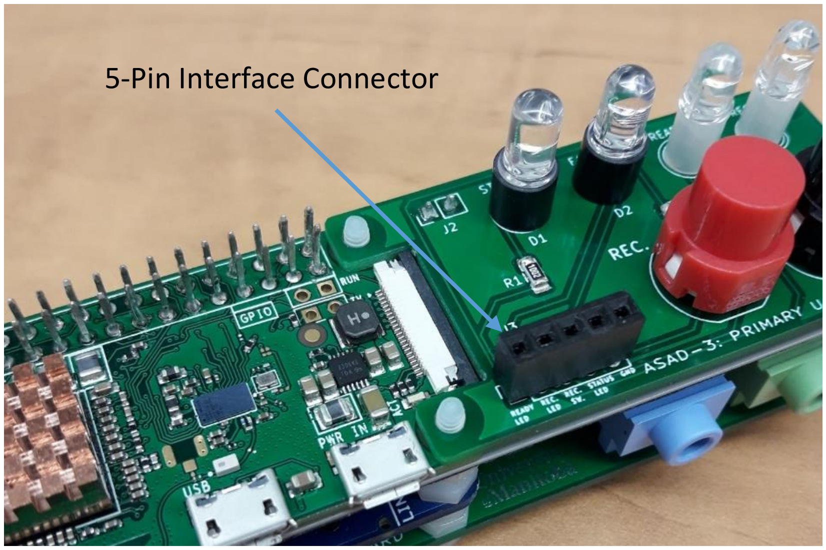

Figure 3.29. Top-view of Audio Recorder showing 5-wire connection between the Primary User Interface Board and the Advanced Used Interface Board.

Pins in the 5-pin connector, from left to right, perform the following functions: first from left connects GPIO/BCM pin 5 to the anode of the “READY” LED, effectively turning on the LED when GPIO/BCM pin 5 is set to high. Second from the left connects GPIO/BCM pin 6 to the anode of the “REC.” LED, effectively turning on the LED when GPIO/BCM pin 6 is set to high. Third from the left connects one terminal of the red-colored “REC.” push-button to GPIO/BCM pin 13. Fourth from the left connects GPIO/BCM pin 16 to the anode of the “STATUS” LED, effectively turning on the LED when GPIO/BCM pin 16 is set to high. The final pin, fifth from the left, provides a connection from the ground BUS of the Raspberry Pi to the Primary User Interface Board.

3.3.4.1. Push Buttons

In total, there are four push buttons that control all functions on the Audio Recorder device: the black-colored push-button (on the Primary User Interface Board) functions as the power “ON/OFF” button, the red-colored button (on the Primary User Interface Board) functions as the recording “START/STOP” button, and the two smaller black and yellow-colored push-buttons (on the Advanced User Interface Board) function to scroll and select options as displayed on the OLED screen.

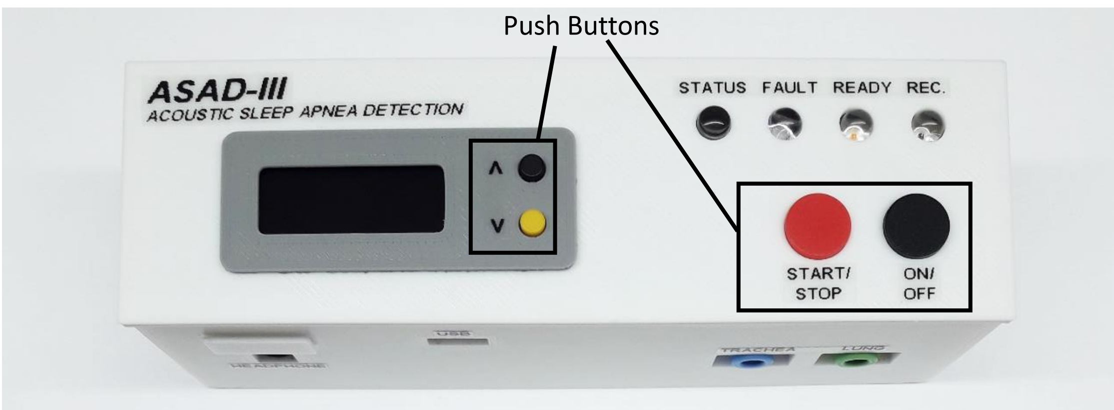

Figure 3.30. Audio Recorder with the four push-buttons illustrated.

The black-colored “ON/OFF” push button (Manufacturer: C&K, Product Number: D6R90 F2 LFS) on the Primary User Interface Board exclusively connects to the OnOff SHIM located on the Microphone Power Supply Board, specifically to two labelled button contact pins on the OnOff SHIM. The black-colored push button is a normally-open, momentary switch that closes the connection between the two button contact pins of the OnOff SHIM when pressed. The two button contact pins of the OnOff SHIM route to the 40-pin header connector of the Microphone Power Supply Board which permits communication with the Raspberry Pi. One of the button contact pins of the OnOff SHIM connects to GPIO/BCM pin 17 of the Raspberry Pi, whereas the second button contact pin is connected to ground of the Raspberry Pi. In addition, the internal circuitry of the OnOff SHIM monitors the activity of the black-colored push button and facilitates the latching and unlatching of the 5 V input power supply from the Raspberry Pi during device start-up and shut-down.

The state of the three other push buttons, the red-colored “START/STOP” push button, as well as the smaller black and yellow-colored push-buttons are monitored directly by the Raspberry Pi and act on the device via the Python command-script described within section 3.3.1 above. The record “START/STOP” push button (Manufacturer: C&K, Product Number: D6R40 F2 LFS) is also a normally-open, momentary switch; it connects the GPIO/BCM input pin 13 (configured in a pull-up configuration) of the Raspberry Pi to ground when pressed. The Python command-script monitors the state of GPIO/BCM pin 13 for a change of logic state, when a transition in logic state is sensed, the Python command-script initiates the start of the audio recording and halts the recording when the next state transition is sensed, i.e., when the record “START/STOP” button is pressed the next time. The smaller, black and yellow-colored push-buttons located next to the device display play a less critical role and hence reflect their minimal size and placement on the device. Like the other two push buttons, both the black and yellow-colored push-buttons are also normally-open, momentary switches. The small, black-colored push-button (Manufacturer: Omron Electronics Inc-EMC Div, Product Number: B3F-1060) connects the GPIO/BCM input pin 26 (configured in a pull-up configuration) of the Raspberry Pi to ground when pressed. Similarly, the small, yellow-colored push-button (Manufacturer: Omron Electronics Inc-EMC Div, Product Number: B3F-1062) connects the GPIO/BCM input pin 25 (configured in a pull-up configuration) of the Raspberry Pi to ground when pressed. The Python command-script monitors the state of GPIO/BCM pins 25 and 26 for a change of logic state, and additionally also monitors the duration the button has been pressed to allow the user to control advanced device functions as shown on the Display Screen. As detailed in the Display Screen section below, when the Audio Recorder is powered on, there are a total of 6 display screen pages that can be displayed on the Display Screen. A short-press (i.e., a press less than 1 second in duration) of the black-colored button once toggles the display to the next display screen page. Similarly, a short-press of the yellow-colored button once toggles the display to the previous display screen page. While on any of the display screen pages, parameters relevant to the device or recording setup can be controlled by a long-press (i.e., a press longer than 1 second in duration) of either the small black-colored or yellow-colored push-buttons, as necessary, on the respective screen pages. For example, to adjust microphone gain, the user would navigate to the Microphone Gain Control screen page (page 2) by a short-press of the black-colored push-button once to advance from the first screen page to the second screen page. Once on the Microphone Gain Control page, the user can adjust microphone gain by a long-press of either the small black-colored or yellow-colored push-buttons. A long-press of the black-colored push-button increases microphone gain by one increment, whereas a long-press of the yellow-colored push-button decreases microphone gain by one increment. Once finished adjusting microphone gain as required, the user can then navigate through the pages as desired by a short-press of either the small black-colored or yellow-colored push-buttons.

3.3.4.2. Status Indicator LEDs

In addition to the display screen on the device, there are 4 additional LED indicator lights located on the upper right corner of the device for “at-a-glance” system status monitoring.

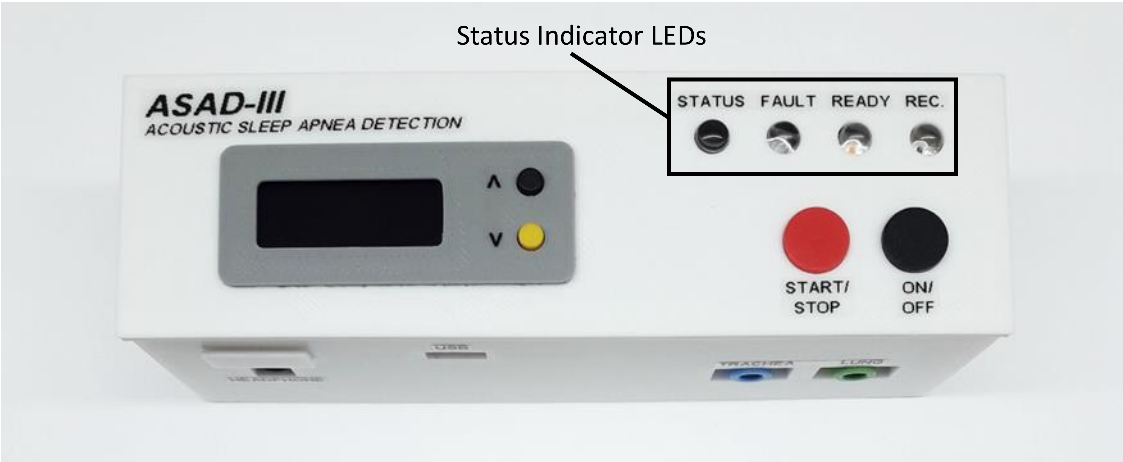

Figure 3.31. Audio Recorder with Status Indicator LEDs illustrated.

The first LED from the left, the “STATUS” LED (Manufacturer: Broadcom Limited, Product Number: HLMP-DB25-B0000, Size: 5mm) is a blue-colored indicator which displays the status of the processor’s disk activity. Disk activity (an indirect measure of processor load) is indicated by the LED, where disk activity will result in the LED being illuminated for the duration of the activity. This indicator lets the user know the approximate load on the processor, and thus if the processor is working or idle at the current moment, but for the general user without specialized knowledge, simply lets them know the device is on and working.

The second LED from the left, the “FAULT” LED (Manufacturer: Adafruit Industries LLC, Product Number: 2700, Size: 5mm) is a high visibility, super-bright (18,000 mcd) yellow-colored indicator which displays if there has been a fault with the microphones or Microphone Power

Supply Board. The Fault Protection Circuit detects if the resettable fuse has triggered or not, where the connection of the resettable fuse to the transistor circuit controls the lighting of the “FAULT” LED. If the fuse has not been triggered and the connection is intact, the LED remains unlit, however once the fuse is triggered, the “FAULT” LED is immediately illuminated to let the user know that there has been a problem and that the device is not ready to be used.

The third LED from the left, the “READY” LED (Manufacturer: Rohm Semiconductor, Product Number: SLA-560MT3F, Size: 5mm) is a green indicator that displays if the device is ready to begin recording or not. Since the recorded audio information is stored exclusively on the removable USB drive, the custom Python command-script has been configured to monitor if the dedicated USB drive has been inserted into the USB connector of the device or not. If the USB drive is not present, the “READY” LED remains unlit, power is not supplied to the Microphone Power Supply Board at this time (a power saving measure for when the device is in stand-by mode) and the record “START/STOP” button will not be sensed when pressed so a recording may not be started if the USB drive is forgotten. Once the USB drive is inserted and mounted to the device, the “READY” LED is illuminated indicating that the device is ready to begin recording. At the same time, power is then provided to the Microphone Power Supply Board and the record “START/STOP” button once again will be sensed if pressed.

The above-mentioned steps and the implementation of the “READY” LED are as a result of the recorded audio data being stored exclusively on the dedicated removable USB drive; a compatibility feature that allows the user to easily transfer the recorder audio information to a PC for analysis by the AWakeOSA algorithm or other evaluation methods. The process described is a preventative measure to ensure that the USB drive is not forgotten when performing a recording.

If the USB is incorrectly removed (i.e., without unmounting) or removed after properly unmounting; the “READY” LED is unlit once again and power is disconnected from the Microphone Power Supply Board to conserve energy during this time when a recording cannot take place.

The fourth LED from the left, the “REC.” (abbreviation for record) LED (Manufacturer: Rohm Semiconductor, Product Number: SLA-560LT3F, Size: 5mm) is a red indicator that displays if the device is currently recording or not. When the “START/STOP” button is pressed (provided the system is ready to begin recording) the custom Python command-script initiates the data creation and capturing process for data received from the two microphones and illuminates the red “REC.” LED. When the record “START/STOP” button is pressed a second time, the custom Python command-script halts the data capturing and closes the file; also turning off the red “REC.” LED to indicate recording has stopped.

To match the standing height of the push buttons and protrude through the device enclosure at the appropriate height, each respective LED was spaced off the Primary User Interface Board using an appropriate nylon spacer. The “STATUS” and “FAULT” LEDs utilize a 6 mm tall spacer (Manufacturer: Essentra Components, Product Number: LEDM-3-06, Height: 6 mm); whereas due to differing height of the LEDs, the “READY” and “REC.” LEDs utilize a 7 mm tall spacer (Manufacturer: Keystone Electronics, Product Number: 8320, Height: 7 mm). The resultant spacing of the LEDs from the Primary User Interface Board permit all four LEDs to protrude slightly through the device enclosure at the same height, creating a uniform yet functional overall design.

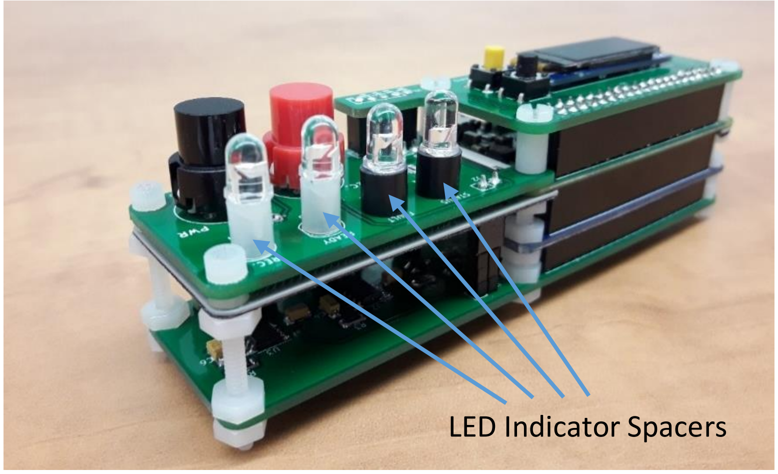

Figure 3.32. Audio Recorder removed from enclosure showing LED indicator spacers.

3.3.4.3. Display Screen

In addition to the status indicator LEDs, a 0.91” organic LED (OLED) display (Manufacturer: TinySine, Product Number: G5780D31C08EE9, Illumination Color: White) was implemented on the Advanced User Interface Board to provide more detailed feedback and an interface to relay and adjust advanced device and recording parameters.

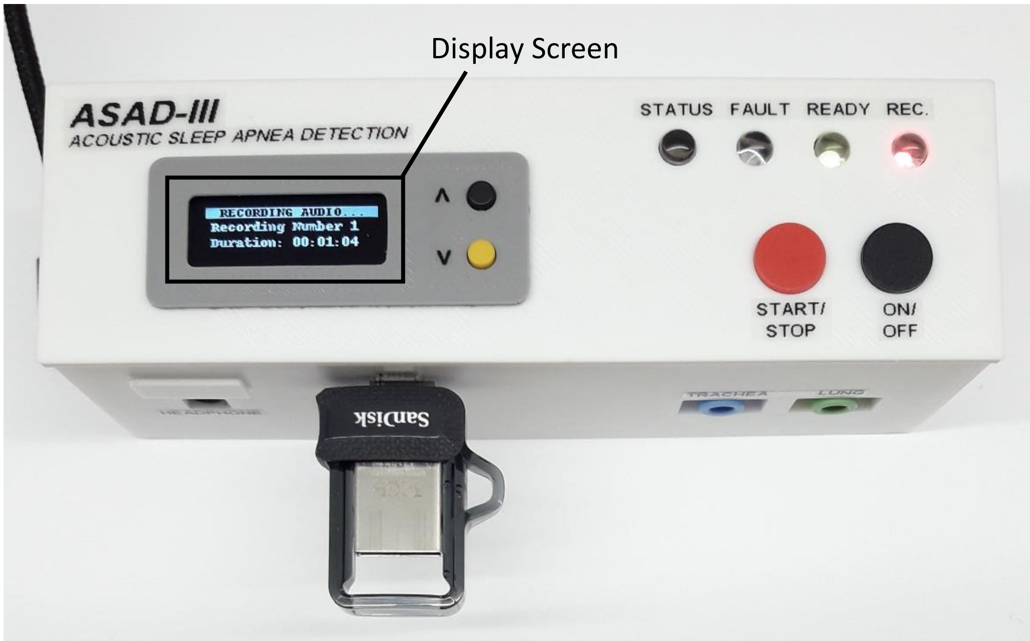

Figure 3.33. Audio Recorder with Display Screen illustrated.

An OLED screen was chosen for its high-contrast and ultra low power consumption. Power consumption is optimized due to the fact black elements on an OLED display do not consume power, only elements producing light consume power (in comparison to LCD screen where a backlight illuminates the whole display, and a filter is used to obstruct light emitted from the backlight to create near-black elements). The OLED display screen powered via the 5 V BUS of the Raspberry Pi and additionally makes connections to the Raspberry Pi for ground as well as serial data and clock communication (via BCM pins 3 and 5, respectively), and thus communicates data via the I^2C communication protocol. Display information is managed via the Python command-script where the information is updated at each iteration of the main program loop.

When first powered on and loading, the Audio Recorder initially shows a splash screen followed by a device information screen showing the device firmware version and unique serial number:

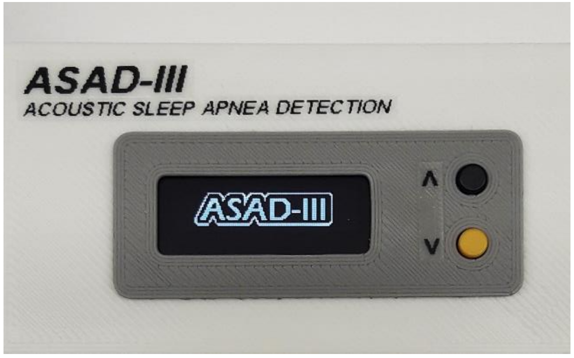

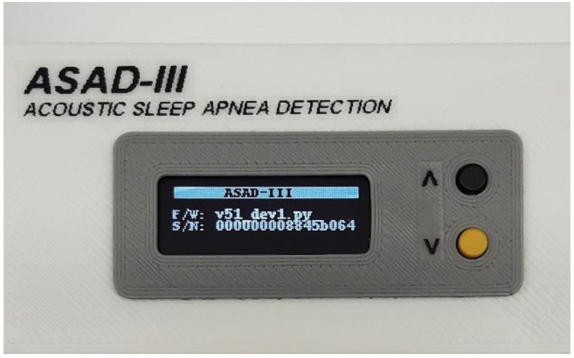

Figure 3.34. Audio Recorder shown powered on demonstrating the information presented by OLED display on start-up and loading of the OS. Left shows the splash screen, right shows the device information screen.

Both the splash screen and the device information screen display for a few seconds until loading of the device is complete. Once loading of the device is complete, the device is ready to be used and the display screen is refreshed to show page 1 in a series of 5 individual pages that may be navigated by the user at any time. By default, the Audio Recorder always shows the first display screen, the Recording Screen Page showing the status of audio recording, whether stopped or started. In total there are 5 display screens: Page 1 - the Recording Screen page (showing the recording status: started or stopped, file name, and recording duration), Page 2 - the Microphone Gain Control page (showing the current microphone gain value and allows the user to increase or decrease microphone gain), Page 3 – the USB Drive Status page (showing the mount status of the USB drive and also allows the user to un-mount the USB drive to remove it), Page 4 – the Device Lights page (showing the status of the 4 LED indicators and allows the user to enable or disable them), and Page 5 – the Device Statistics page (showing critical CPU statistics: memory usage, disk usage, and CPU temperature). The series of information pages are shown as presented on the OLED screen in Fig. 3.35 on the following page:

Page 1: Recording Screen (Stopped)

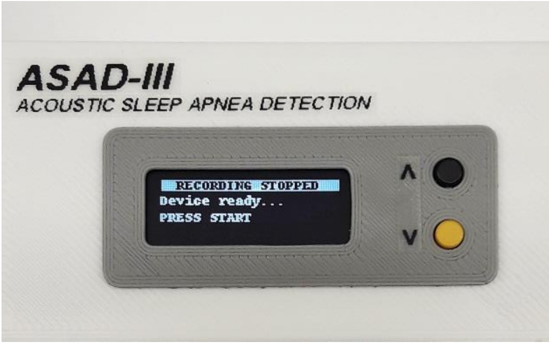

Page 1: Recording Screen (Started)

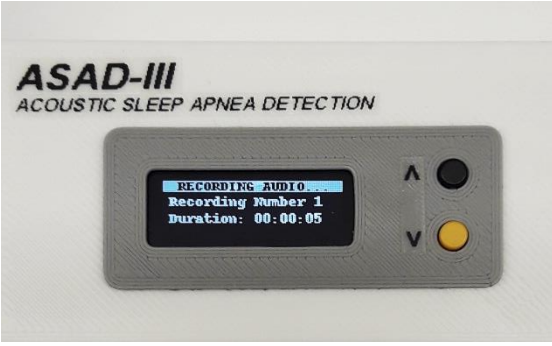

Page 2: Microphone Gain Control

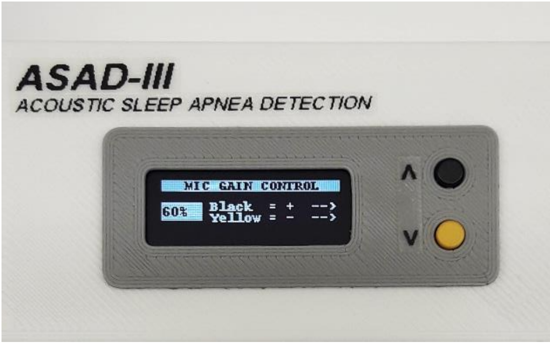

Page 3: USB Drive Status

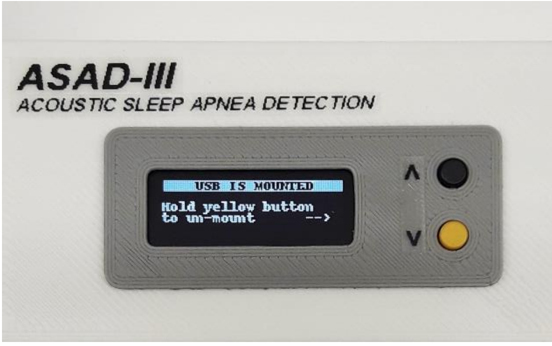

Page 4: Device Lights

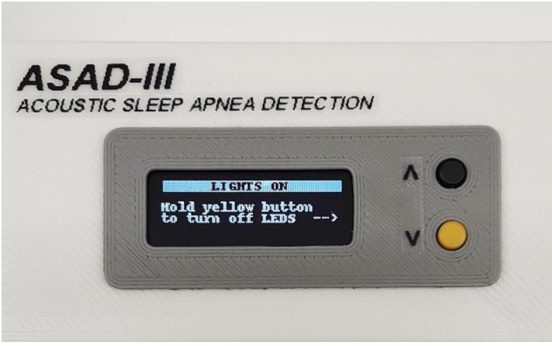

Page 5: Device Statistics

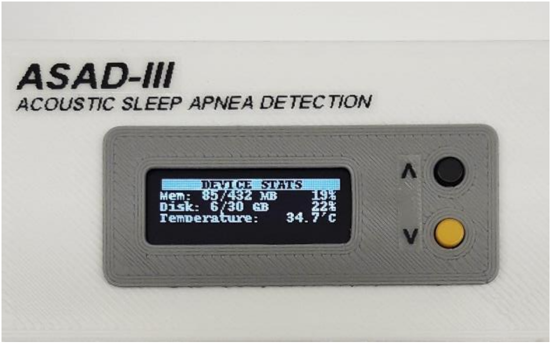

Figure 3.35. Audio Recorder shown powered on demonstrating the information presented by OLED display on various display screen pages.

The user can navigate through the pages by operating the small black-colored and yellow-colored push-buttons next to the Display Screen and additionally control the parameters with the same push-button by a long-press of the respective button and the on-screen instructions.

As was mentioned previously, the USB drive is critical to the recording process as it is used to exclusively store the recorded data. If at any time the USB drive is not inserted into the Audio Recorder, the functionality of the device becomes limited and the recording may not be started if the USB drive is not present. Additionally, the Display Screen shows an error message and indicates to the user that the USB drive is missing and must be inserted to use the device. Once the USB drive is inserted and mounted to the device, limitations to device functionality are lifted and the error message on the Display Screen is removed returning the user back to the set of 5 display screen pages.

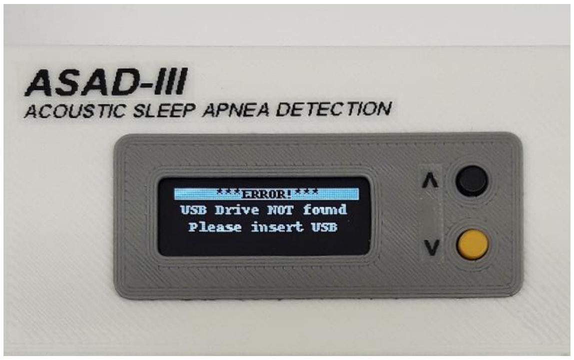

Figure 3.36. Audio Recorder shown powered on demonstrating the error message presented by OLED display when the USB drive is not inserted into the Audio Recorder.

3.3.5. Enclosure

Throughout the design and fabrication process of the internal circuitry comprising the Audio Recorder, two objectives were consistently adhered to, both of which influenced the final design for the device enclosure. The first objective was to constrain the size of circuit boards (when possible) as much as possible while maintaining a modular configuration. The second objective was to organize the access to connectors and user interface components in a simple and organized manner that would be extremely straight forward to use. Adhering to these objectives, the hardware/circuit design process was completed with the task of designing the enclosure immediately following. Realizing that there were no pre-existing enclosures that would be a perfect fit for the completed custom Audio Recorder hardware, it was decided to design a 3-dimensional (3D) custom case that could be printed via additive manufacturing techniques (i.e., 3D printing) to enclose the hardware within. Following this decision, both the method for 3D printing and the types of available print material used for the printing were examined and evaluated. Due to the large cost differential among printing techniques, the technique of fused deposition modeling (FDM) was chosen for its relatively low cost and large popularity, making the print of the enclosure both easy to acquire and nominal in cost. Print materials were next examined and compared with thermoplastic materials being selected first and foremost since they are non-electrically conductive (a major importance since the circuit boards inside would be in direct contact with the enclose), for their robust durability and strength, and overall low-cost. The thermoplastic filament materials acrylonitrile butadiene styrene (ABS), nylon, and polylactic acid (PLA) were examined for their properties. Characteristics of the thermoplastics including strength, stiffness, durability, and printability (a measure of how accurate the 3D printed part matches the original design specifications) were compared and the PLA material was selected for its high strength and increased stiffness, and high printability in comparison to both ABS and nylon which are both decreased in strength, stiffness, and printability aspects.

Precise dimensions of the overall hardware, as well as every location for the buttons, display, and connectors was taken from the fabricated Audio Recorder hardware and imported into a 3D modeling suite. Structural tolerances for the PLA thermoplastic filament material were selected at 150% - 250% to ensure the durability and strength of the enclosure would last for years to come without damage. A means of accessing the interior of the enclosure was needed to be able to insert the electronic hardware and to permit access to the hardware if servicing were to be required. It was thus decided to split the enclosure into 2 components: the primary component would form the two side walls, back-side wall, and top of the enclosure; the secondary component would form the front-side wall and bottom of the enclosure.

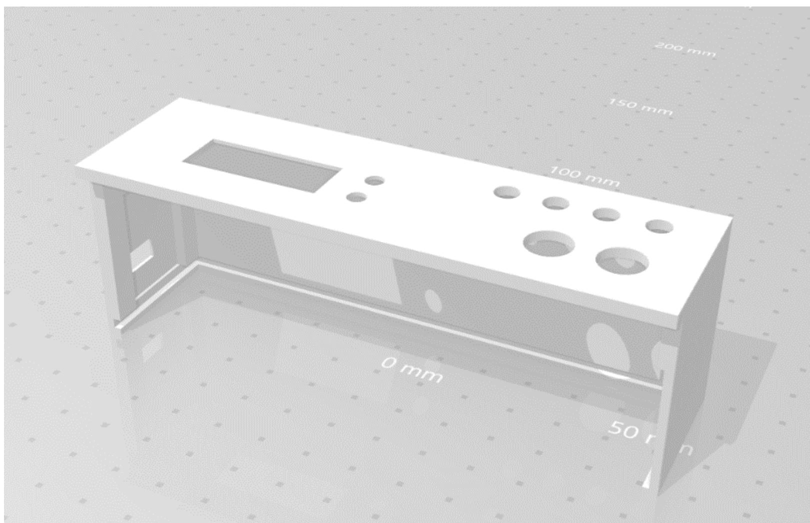

Figure 3.37. Enclosure model with primary component shown, including the two side walls, back-side wall, and top.

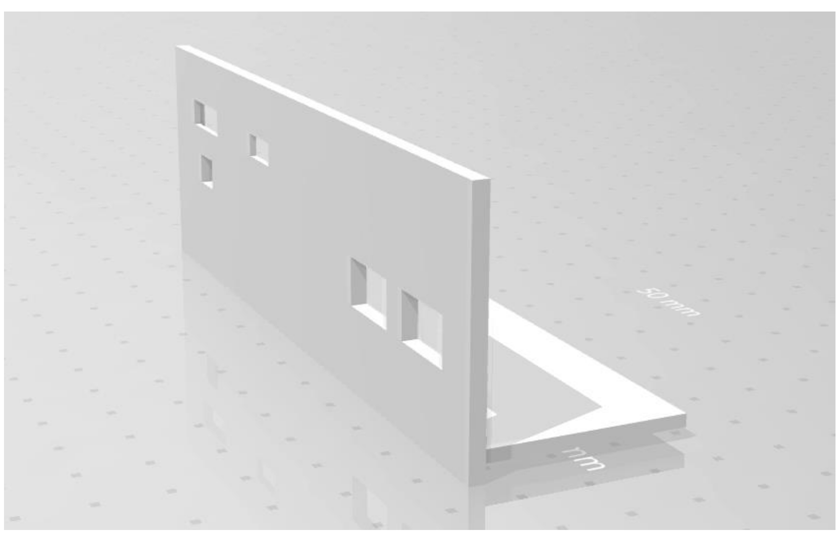

Figure 3.38. Enclosure model with secondary component shown, including the front-side wall and bottom.

Next the task of attaching the two components of the device enclosure was examined. Traditional techniques using metallic fasteners were avoided to avoid supports and provisions for such, which would have made the device enclosure larger in size; and additionally, could potentially contact exposed sections of the electric circuits inside resulting in short circuits and probable damage. As such, the secondary component of the enclosure (front and bottom) was designed such that the bottom of the enclosure slides into channels present on the two side walls of the primary component. The secondary component slides from front to back with a snug, friction-fit with a "latch" segment integrated into the primary component that holds the secondary component securely in place when fully inserted.

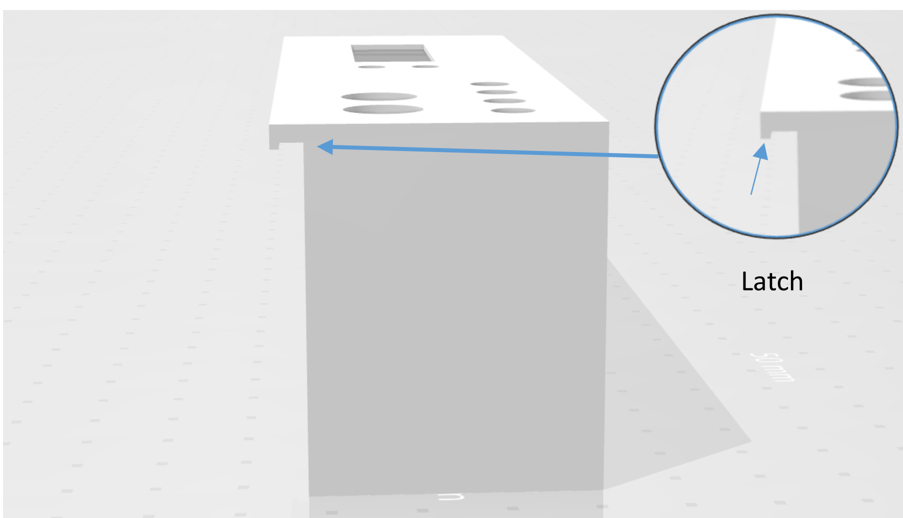

Figure 3.39. 3D model of enclosure, side view showing the integrated latch.

Provisions inside the enclosure were also integrated to allow for the quick and easy removal of the electronic hardware; especially important from the prototype aspect since final device configuration and hardware tests/checks were on-going. Specifically, cut-outs were implemented inside to permit the insertion of the hardware such as to allow clearance for the protruding micro-

SD card, as well as clearance for the entire circuit to slide "up and into" the primary component without excessive friction yet hold the electronic hardware securely once in final position.

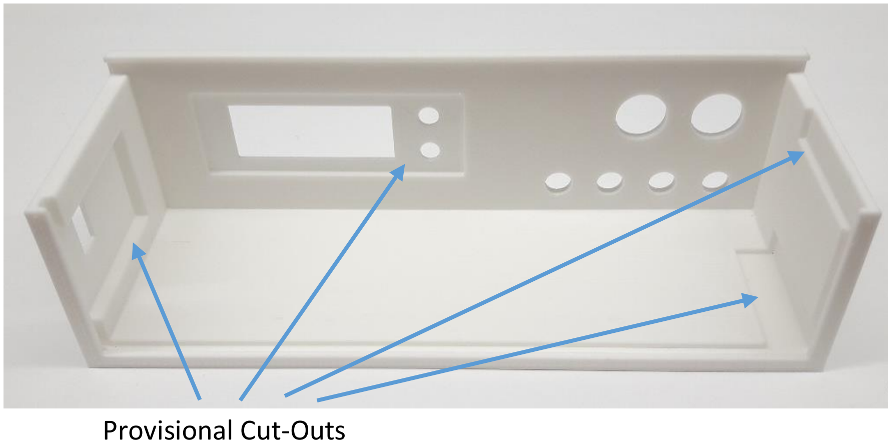

Figure 3.40. Primary component of Audio Recorder enclosure illustrating internal provisional cut-outs.

The photo shown in Fig. 3.41 illustrates the installation of the Audio Recorder hardware into the primary component of the enclosure with the major components illustrated:

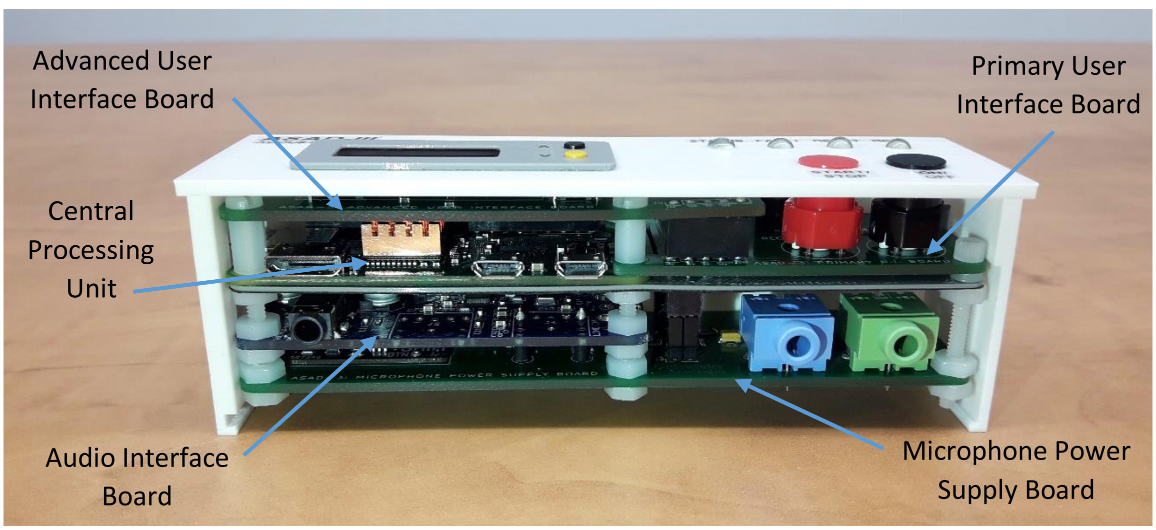

Figure 3.41. Audio Recorder with front cover removed showing the internal components of the device installed into the enclosure.

3.4. Evaluation

Evaluation of the Audio Recorder is somewhat challenging due to the specialized purpose of the device and a lack of commercial respiratory sound recording devices of which could be used for comparison. In this regard, the Audio Recorder was assessed for performance in sound capture by comparison to a Class 1 sound level meter. A Class 1 sound level meter is designed to adhere to the international standard defined by IEC 61672 which specifies the tolerances in the sound level measured for a set of frequencies of capture by the device. IEC 61672 describes tolerances by two categories of either Class 1 or Class 2, where Class 1 tolerances are stricter than those described within Class 2. The tolerances are summarized within Table 3.4-1:

Table 3.4-2. IEC 61672-1 Tolerances

Frequency:	**Class 1 Tolerance:**	**Class 2 Tolerance:**
16 Hz	+2.5 dB, -4.5 dB	+5.5 dB, -∞ dB
20 Hz	+2.5 dB, -2.5 dB	+3.5 dB, -3.5 dB
1 kHz	+1.1 dB, -1.1 dB	+1.4 dB, -1.4 dB
10 kHz	+2.6 dB, -3.6 dB	+5.6 dB, -∞ dB
16 kHz	+3.5 dB, -17 dB	+6.0 dB, -∞ dB

The Class 1 sound level meter used was a Brüel & Kjær (B&K) model: Type 2250-S. For the ASAD-III device, we used the Primo EM172Z1 microphone, the selected microphone from the analysis conducted and described by Chapter 4 of this report. To evaluate the performance of the ASAD-III device, we positioned a microphone of the ASAD-III device next to the microphone of the B&K 2250-S, applied a sound stimulus played over speaker, and recorded from the two devices simultaneously.

Figure 3.42. Brüel & Kjær (B&K) model Type 2250-S sound level meter. Source: [53]

The audio recording was conducted in an anechoic chamber (> 30 dB noise reduction) with all ulterior sound sources being silenced during the recording. In addition, the microphones were placed inside a Microphone Isolation Box, the design and use of which is described further within the Appendix, section 8.8.

The speaker used to generate the sound stimulus was placed at the opening of the Microphone Isolation Box. The sound stimulus used was a full-spectrum (10 Hz – 20,000 Hz) sine sweep which is a sinusoidal waveform with frequency that increases (i.e., sweeps) gradually with time. The sweep duration for the sound stimulus was 10 seconds. The sine sweep was chosen since it generates only a pure tone (i.e., a tone with a single frequency) for each frequency that is swept through. This is advantageous since for each individual frequency that is swept through, tones with high energy are produced since the full signal power is used purely for that tone. Contrary, other analyses using for example white or pink noise sound stimuli, generate tones of many frequencies simultaneously and thus the signal power is divided amongst all the tones as a result. With the high energy tones generated by the sine sweep, this provides the best scenario to eliminate background noise from interfering with the response of the system.

Ideally, the frequency response of the system being tested in response to a sine sweep would exhibit a completely flat response with the same amplitude/sound level measured for each frequency. However, because the ASAD-III as well as the B&K sound level meter are audio recording devices, many factors influence the resulting frequency response captured with an audio recording device. First and foremost, speakers generate a non-flat output frequency response (i.e., when generating sounds). Similarly, microphones also generate a non-flat input frequency response (i.e., when capturing sounds). In both cases, the non-flat frequency response is a physical property inherent to the design, where although the design can influence the response to be relatively flat or flat in a specific frequency range, it is impossible to achieve a completely flat frequency response for all frequencies. As well, the shape and construction of the room in which the recording takes place influences the frequency response of the audio recorder. Sharp corners and hard surfaces within the room produce sound reflections which can reach to the microphone and combine with the sound waves emitted from the source and thus influence the frequency response recorded.

The sound level meter, being a Class 1 certified device, provides the best means to establish a baseline to which we can compare the response and thus assess the performance of the ASAD-III device. With the sound level meter and the ASAD-III recording the same sounds at the same time, in the same room, and in nearly the identical spatial location, the sound level meter provides an accurate frequency response with tolerances meeting the Class 1 criteria. Hence, in the recorded frequency response presented, it is the differences in the response of the ASAD-III compared relative to the frequency response of the B&K sound level meter that are important. The frequency response of the B&K sound level meter along with the frequency response of the ASAD-III system is presented in Fig. 3.43:

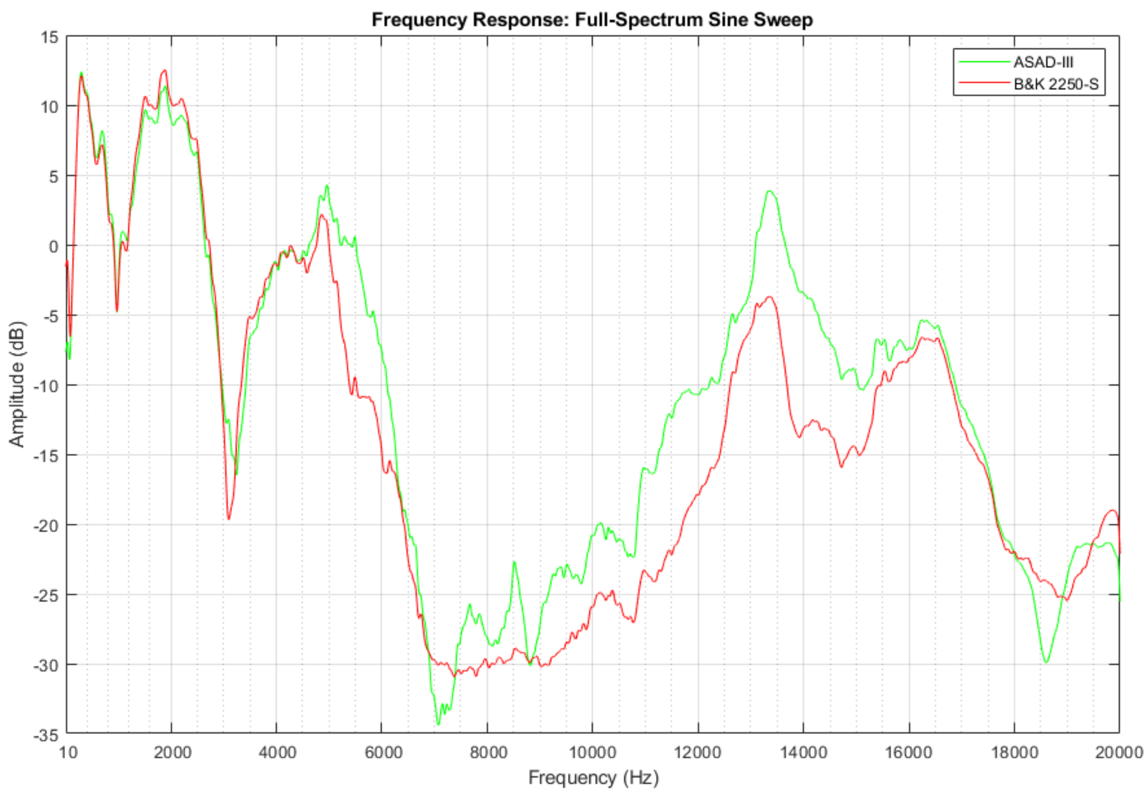

Figure 3.43. Frequency response of the Brüel & Kjær (B&K) model Type 2250-S sound level meter as well as the ASAD-III Audio Recording System when a full-spectrum sine sweep was applied.

From Fig. 3.43, initially and up to 5000 Hz, the response of the ASAD-III system follows the response of the B&K 2250-S quite closely with variations of only 1-2 dB observed. However, following from 5000 Hz and through to 6300 Hz, the response of the ASAD-III shows a higher amplitude response relative to the response of the B&K 2250-S with maximum deviation of approximately +9 dB observed at 5500 Hz. From 6300 – 6900 Hz, the response of the ASAD-III once again very closely follows the response of the B&K 2250-S with minor deviations of +1-2 dB observed. Following from 6900 Hz, the ASAD-III initially undershoots the response of the B&K 2250-S until 7400 Hz where a sharp increase in response is observed. From 7400 Hz and until 16,500 Hz the ASAD-III response displays a higher amplitude response relative to the B&K 2250-S by +7-8 dB. From 16,500 Hz through to 18,000 Hz, the response of the two systems is once again very similar with +1-2 dB deviation observed. From 18,900 – 19,500 Hz, the ASAD-III overshoots the B&K 2250-S response with maximum +2 dB deviation. Finally, from 19,500 – 20,000 Hz the ASAD-III undershoots the B&K 2250-S response by maximum -2.5 dB deviation.

In summary, the two frequency response curves show varying degrees of variation in signal amplitude but are observed to show the same general overall trend for the frequency span measured. This result was not unexpected, since no two devices can be manufactured identical as a result of individual electronic component tolerances and manufacturing variances. The international standard defined by IEC 61672 makes clear reference to such behaviour as indicated by the tolerances allowed to adhere to performance criteria. Hence the two frequency response curves can be compared at the frequencies identified within the IEC 61672 standard to provide a relative sense of performance. Table 3.4-2 on the following page shows the amplitudes for the two frequency response curves at the frequencies defined within the IEC 61672 standard:

Table 3.4-2. Measured Sound Levels

Frequency:	ASAD-III	B&K 2250-S	Delta*
16 Hz	-7.65 dB	-1.52 dB	-6.13 dB
20 Hz	-7.34 dB	-1.25 dB	-6.09 dB
1 kHz	-3.39 dB	-3.65 dB	+0.26 dB
10 kHz	-20.81 dB	-25.95 dB	+5.14 dB
16 kHz	-7.39 dB	-8.17 dB	+0.78 dB

*Delta = (ASAD-III) – (B&K 2250-S)

Comparing the delta column of Table 3.4-2 is relative to Table 3.4-1, the ASAD-III meets the criteria for Class 2 tolerances at the frequencies of 16 Hz, 1 kHz, 10 kHz, and 16 kHz, but does not quite meet the Class 2 tolerances for the frequency of 20 Hz as the signal amplitude is outside the tolerance. This result can be explained by the fact the frequency range of the EM172Z1 microphone utilized with the ASAD-III device is from 60 – 20,000 Hz; hence, it does not begin to effectively capture sound below 60 Hz.

3.5. Discussion

Following from the above sections presented, the Audio Recorder has been shown to meet the desired specifications, including the required technical criteria with exceptional performance. Although the ASAD-III device is fully functional, it is important to note that the device is still a prototype and naturally there are a few aspects that could be developed further to bring the device to an even higher standard. Possible improvements for the Audio Recorder have been mentioned in the concluding remarks, specifically within Chapter 7.3: Suggestions for Future Work.

Chapter 4

4. Microphones

4.1. Introduction

The design of the ASAD-III device described by this report utilizes two microphones, one to record tracheal sounds, and the second to record lung sounds. A microphone, in the most general sense, is a transduction device that converts sound into an electrical signal. Sound is merely a propagation of pressure waves through a medium, typically of which is air. By design, microphones operate by utilizing a sensitive diaphragm that becomes deflected due to air-pressure changes and produces a corresponding electrical signal as a result of the deflection. During breathing, air flowing into or out of the lungs becomes turbulent as it travels through the respiratory tract; and such turbulence produces vibrations in tissues surrounding the airway walls. Such vibrations transfer to the surface of the skin and can effectively be captured by a microphone if there is a medium such as air, between the skin surface and diaphragm of the microphone [21]. Hence, tracheal and other respiratory sounds can thus be recorded by a microphone placed over the airway, provided there is a sufficient air medium.

4.2. Design Specifications

Microphone selection was one of the most critical design decisions of the ASAD-III recording device. With so many microphones available on the market, establishing a set of criteria to narrow down the list of microphones to a reasonable amount that could be practically tested and evaluated for performance for use with the Audio Recorder was essential. Basic criteria were established by considering two factors: first and foremost, microphone performance criteria, i.e., the ability of the microphone to capture the desired spectrum of tracheal and lung respiratory sounds. Secondly, microphone compatibility criteria, i.e., the ability of the microphones to function with the Audio Recorder hardware, as well as alignment with the overall objectives of maintaining a small size, and cost-effective overall device were considered.

Placement of the two microphones was carefully considered and the locations of the tracheal suprasternal notch, and the right mid-clavicular 2^{nd} intercostal space are selected for capturing tracheal and lung sounds, respectively. These two locations are the most commonly used locations for capturing tracheal and lung sounds. The tracheal suprasternal notch provides a convenient place for the microphone to be affixed on the trachea away from arteries, and the right mid-clavicular 2^{nd} intercostal space over the chest is the best location to provide the largest difference between respiratory phases with minimum interference from heart sounds (the purpose of using such sounds in the AWakeOSA algorithm) [22].

The anatomical locations for the placement of the two respective microphones are identified on Fig. 4.1.

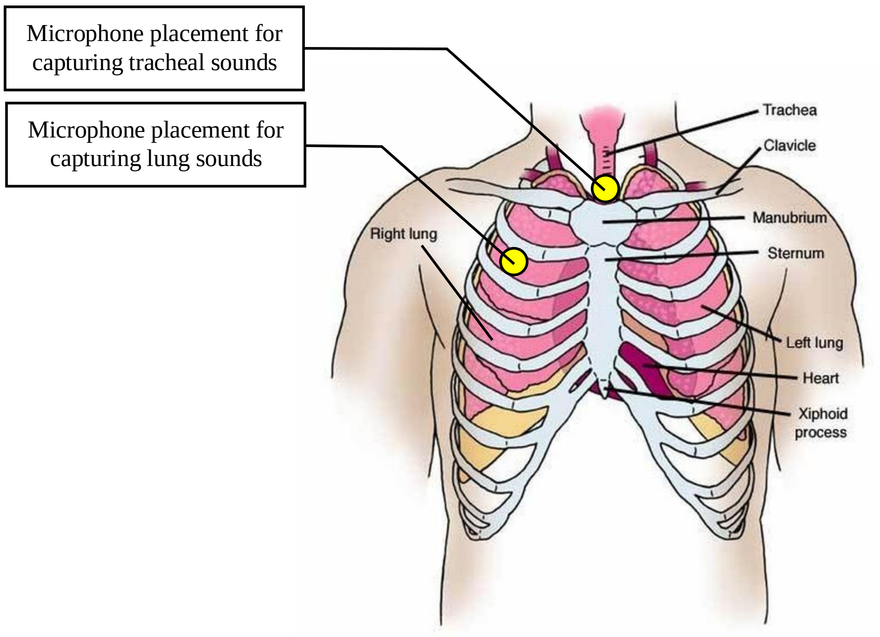

Figure 4.1. Placement of the two microphones for capturing tracheal and lung sounds respectively. Source: [42]

In this study, the Sony ECM-77B microphone was used as a benchmark as it was used in many of our team's and many other research teams' studies. Based on the experience of our research group, as one of the pioneers in respiratory sounds analysis, a set of requirements for desired performance criteria of the microphone are presented in Table 4.2-1.

Table 4.2-1. Microphone Performance Criteria

Feature:	**Value or Range:**	**Explanation:**
Frequency Range	100 – 20,000 Hz	The range of frequencies capable of capture by the microphone.
Directivity	Uni-directional or Omni-directional	The capture pattern of the microphone.
Sensitivity	≥ (- 50 dB)	The smallest sound pressure capable of being measured by the microphone.
Signal-to-Noise Ratio (SNR)	≥ 50 dB	The ratio of the signal power compared to the power of the electrical noise.

As a first performance criterion, the range of frequencies that could be captured by the microphone was established. To facilitate the high-frequency analysis and permit the Audio Recorder to record frequencies up to 20 kHz, the microphone would need to have a frequency range spanning up to 20 kHz as well. On the other hand, low-frequency components of tracheal and lung sounds are well known to have components lower than 100 Hz [12] which is normally the low cut-off frequency of most voice audio recorders. Therefore, to encapsulate the whole spectrum of respiratory sounds, microphones with a range of at-least 100 - 20,000 Hz only were chosen and tested.

The directivity of the microphone refers to the spatial pattern in which the microphones can detect sounds. Omni-directional refers to the fact that a microphone senses sound equally from all spatial positions around the microphone, whereas uni-directional refers to the ability of the microphone to detect sound from one direction (typically from in front of the sensing element) more than any other spatial position around the microphone. Studies in the past had used omni-directional microphones but it was hypothesized that uni-directional microphones should produce a better result given the intended purpose for capturing sounds from the surface of the skin. Hence, both types were tested and examined for their performance.

The sensitivity of the microphone refers to the amount of output produced by the microphone for a given input. The input for sensitivity measurements is standardized as a reference of 1 Pascal of pressure or 94 dB sound pressure level. Negative dB values are used to describe the output relative the reference. A sensitivity of -50 dB was considered as the minimal performance criteria value for microphone selection.

Since all electronic devices and components have some level of electrical noise when in operation, the SNR is a standard measure used to express the ratio of the output signal power with respect to the electrical noise power. Such electrical noise cannot be avoided; as long as the signal power is much greater than the power of the electrical noise, the output signal is usable and accurate to a great extent. A value of 50 dB minimum was selected to ensure high accuracy and thus performance of the microphone.

Additional criteria regarding the compatibility and suitability requirement of the microphones for use with the Audio Recorder were next outlined and are thus summarized and presented in Table 4.2-2.

Table 4.2-2. Microphone Compatibility Criteria

Feature:	**Value or Range:**	**Explanation:**
Function Type	Electret Condenser Microphone	The mechanism for how the microphone functions.
Output Format Type	Analog Output	The format of the data being output by the microphone.
Supply Voltage	≤ 5 V	Input power required for the microphone to function.
Output Impedance	≤ 600 Ω	Electrical resistance to current flow from the microphone into the connected load.

As a first compatibility criteria, the functional type of microphone to be used was decided upon as the electret condenser style microphone. Condenser microphones in general were selected because they utilize smaller and lighter mass diaphragms to capture sound. The smaller and lighter diaphragm is a significant benefit for capturing higher frequency sounds since high frequencies are known to have less energy than lower frequencies. With less energy, high frequency sounds have less ability to act upon a mass (i.e., the diaphragm); hence, the smaller and lighter the diaphragm, the better that high frequency sounds can be captured. The sub-category of electret condenser microphones was selected for its ease of application and low supply voltage required. Traditionally, condenser microphones need a supply voltage large enough to charge two plates inside the microphone, where the two plates, once charged, act as a capacitor. In the microphone construction, one of the internal plates is formed by the diaphragm and the other plate remains stationary a certain distance away from the diaphragm inside the microphone. When the two plates are charged, an electric field is created between the plates, proportional to the spacing between them. When the diaphragm is deflected by sound pressure, the distance between the plates produces a corresponding change in voltage across the plates, which in turn, generates the output of the microphone.

Electret condenser microphones do not require the typically large supply voltage; instead, they utilize a permanently charged electret material, i.e., a polarized dielectric material (analogous to a permanent magnet), to form one of the charged plates (typically the stationary plate). The diaphragm of an electret condenser microphone is metalized and connected to the gate input of a field-effect transistor (FET) such that when the diaphragm is deflected, the potential of the gate input of the FET is varied. The variation in the gate input of the FET alters the conductivity between the drain and source terminals of the FET; hence, it produces a voltage output corresponding to the deflection of the diaphragm. Although the electret condenser microphone does not require an externally applied voltage to charge the internal plates, a small voltage supply is still required to power the FET circuitry. Typically, a DC voltage of less than 10 V is sufficient to power the FET circuit and hence the topic of supply voltage was next considered. As the microphones are desired to be adhered to the skin in our applications, microphones that have bulky batteries or other voltage sources attached are avoided in favor of microphones that could be powered directly through a connection to Audio Recorder. As a result, the supply voltage for the microphones is required to be 5 V or less due strictly to the power supplies available on the Raspberry Pi.

Equally as important, the choice for the data output type of the microphones was examined. Regarding electret condenser microphones, three output types are available: digital output, pulse density modulation (PDM) output, and lastly analog output. Digital output microphones would have avoided the need for the Audio Interface Board provided they could directly interface with the Raspberry Pi via the available communication protocols, however support for recording from digital microphones via the Linux based Raspberry Pi OS at the time of designing the device was extremely limited and deemed unfeasible. PDM output microphones are a subset of digital microphones in that they produce a digital output that relays information by variation of the pulse density of a digital signal. PDM output microphones are not supported by the Raspberry Pi directly, and there are no available interface boards to accommodate PDM output microphones available at the time of designing the ASAD-III device. In the end, the traditional analog output style microphone was chosen due to its widespread support and known functionality with the Raspberry Pi, specifically with the Linux based Raspberry Pi OS.

Output impedance of the respective microphones was also considered to ensure the best quality audio could be captured by the Audio Recorder from the microphones. To achieve the best audio signal microphone, the output impedance should be low, whereas input impedance of the recording circuit should be considerably much higher. The SGTL5000 audio codec implemented by the Audio Interface Board has a corresponding line-input input impedance of 29 kΩ. Hence, for the selection of microphones, only the ones with low impedance (less than 2.9 kΩ) were selected for evaluation.

The physical size of the microphone is also a defining factor due to the intended use of the device. Large, heavy microphone are difficult to keep in contact with the surface of the skin for individuals being recorded. One of the design characteristics borrowed from the Biopac System was the use of the Microphone Coupler to act as a fixture to hold and mount the microphone to the skin (via double sided adhesive). For our application, the microphone must be small and light enough to fit inside a considerably small-sized Microphone Coupler to permit the adhesive rings to be firmly adhere the microphone and Microphone Coupler to the surface of the skin.

Due to the overlap and similarity of criteria required for capturing tracheal and lung sounds, it was decided to use the same selected microphone model for both microphones used with the ASAD-III Audio Recorder. This has a practical implication with the device and its use as well since there is no concern of applying the incorrect microphone to the recording location. Either of the microphones can be placed at either recording location and will function exactly as intended.

4.3. Microphones

With the above design specifications established, the following five different capsule-style electret condenser microphones were chosen to examine their performance for capturing respiratory sounds.

i. AOM-5024 (Manufacturer: PUI Audio Inc., Product Number: AOM-5024L-HD-R)
ii. AUM-5247 (Manufacturer: PUI Audio Inc., Product Number: AUM-5247L-C3310-R)
iii. CMI-5247 (Manufacturer: CUI Inc., Product Number: CMI-5247TF-K)
iv. EM172 (Manufacturer: Primo Co. Ltd., Product Number: EM172Z1)
v. EM264 (Manufacturer: Primo Co. Ltd., Product Number: EM264Y)

Abbreviated microphone product names are used going forward. A table summarizing the general properties for each respective microphone is displayed in Table 4.3-1, as well as technical properties displayed in Table 4.3-2, both on the following page:

Table 4.3-1. Microphone General Properties

Microphone:	Function Type:	Output Format Type:	Supply Voltage:	Size Format:	Diameter:	Height:
PUI Audio Inc. AOM-5024L-HD-R (AOM-5024)	Electret Condenser Microphone	Analog Output	1 – 10 V DC	Capsule-Style	9.7 mm	5.0 mm
PUI Audio Inc. AUM-5247L-C3310-R (AUM-5247)	Electret Condenser Microphone	Analog Output	1 – 10 V DC	Capsule-Style	9.7 mm	5.0 mm
CUI Inc. CMI-5247TF-K (CMI-5247)	Electret Condenser Microphone	Analog Output	1.5 - 10 V DC	Capsule-Style	9.7 mm	5.2 mm
Primo EM172Z1 (EM172)	Electret Condenser Microphone	Analog Output	3 V DC	Capsule-Style	10.0 mm	4.5 mm
Primo EM264Y (EM264)	Electret Condenser Microphone	Analog Output	3 V DC	Capsule-Style	10.0 mm	4.5 mm

Table 4.3-2. Microphone Technical Properties

Microphone	Directivity	Frequency Range	Sensitivity [b]	SNR [c]	Output Impedance [d]
PUI Audio Inc. AOM-5024L-HD-R (AOM-5024)	Omni-directional	20 – 20,000 Hz	-24 dB ±3 dB	80 dB	2.2 kΩ
PUI Audio Inc. AUM-5247L-C3310-R (AUM-5247)	Uni-directional	20 – 20,000 Hz [a]	-47 dB ±3 dB	55 dB	0.68 kΩ
CUI Inc. CMI-5247TF-K (CMI-5247)	Uni-directional	70 – 20,000 Hz [a]	-47 dB ± 3 dB	60 dB	0.68 kΩ
Primo EM172Z1 (EM172)	Omni-directional	60 – 20,000 Hz	-28 dB ± 3 dB	80 dB	1.5 kΩ
Primo EM264Y (EM264)	Uni-directional	60 – 20,000 Hz [a]	-37 dB ± 3 dB	74 dB	1.4 kΩ

[a] Directional on-axis 0° measurement
[b] Frequency = 1 kHz, 0 dB = 1 V / Pa
[c] Frequency = 1kHz, A-weighted network
[d] Frequency = 1kHz

As noted by Table 4.3-1, general properties of the five microphones selected are similar; this is a direct result of choosing microphones that were suitable and compatible with the Audio Recorder and in-line with overall design objectives. However, distinct differences between the microphones can be noted within Table 4.3-2. Firstly, the choice in directivity of the selected microphones is either omni-directional or uni-directional. Uni-directional microphones seem the logical choice for capturing respiratory sounds from the surface of the skin since there would theoretically be a reduction in sounds captured from other sources (i.e., background noise, etc.). However, the three microphones with uni-directional directivity exhibit relatively lower sensitivity and lower SNR as compared to the two omni-directional microphones. Thus, the choice in microphone directionality was not straight forward as each choice has its benefits. Therefore, testing all the respective microphones for the intended purpose of capturing respiratory sounds was conducted and evaluated to select the best microphone for our application.

4.4. Evaluation

Microphone selection is inherently a relatively challenging task as there is not one best microphone for capturing all sounds or that is best for every application. The performance characteristics of a microphone relate to the physical properties of the microphone and its manufacture; hence, there will always be trade-offs in performance characteristics when one of the characteristics is emphasized. This understanding thus led to the evaluation technique for selecting the optimal microphone from the set of five selected microphones that is best for our desired signals to record (respiratory breathing sounds, in particular, tracheal sounds). Specifically, each of the selected microphones was used to capture tracheal breathing sounds while following a recording procedure and the results processed and then compared relative to one another.

4.4.1. Recording Device Setup & Procedure

One at a time, each of the five microphones was affixed to the skin over the suprasternal notch using double-sided adhesive. For each microphone, the same custom-designed Microphone Coupler with Air-Chamber was used to hold the microphone and capture tracheal breathing sounds.

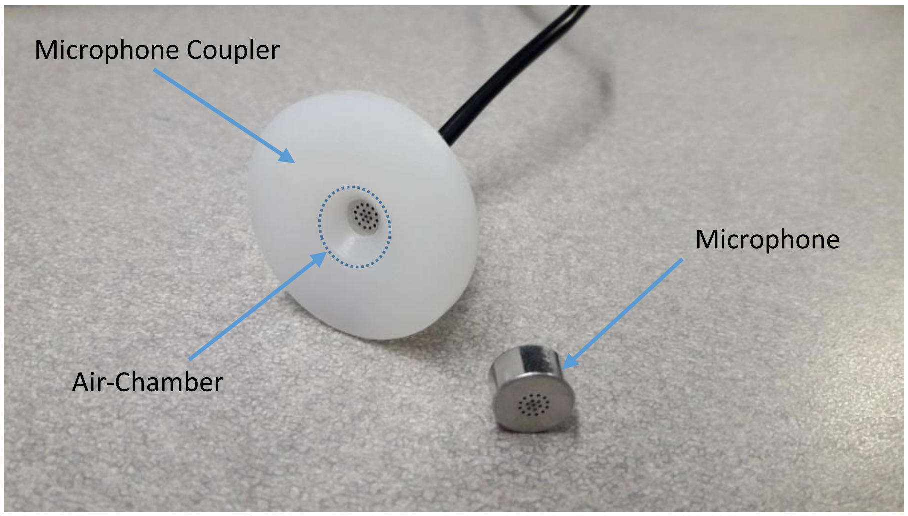

Figure 4.2. Microphone Coupler with Air-Chamber. Microphone inserted into the coupler (left), and microphone without coupler (right).

The Air-Chamber design was made to match with the one used previously with the Biopac system in our research team; that was a conical and cylindrical compound design and had dimensions of 2.6 mm overall depth, 8.00 mm aperture diameter at the opening (i.e., at the surface of the skin) and 4.65 mm aperture diameter at the microphone capsule [23]. For each recording, the subject (a 29-year-old healthy male) was guided by the researcher to follow a breathing pattern that consisted of 5 complete breathing cycles at their normal flow rate starting with inspiration and breathing exclusively through the mouth. The subject was also instructed to hold his breath for 5 seconds at the end of the 5 breathing cycles to capture the background noise and calculate the SNR during the breathing cycles compared to the background noise.

The five different microphones were implemented using the recommended drive circuit described within the respective datasheet for each microphone. All microphones were analog output and hence digitization of the analog signal from the microphone was performed using the custom-designed Audio Recorder hardware device described in Chapter 3 of this thesis. Recordings from each microphone were stored in the lossless (uncompressed) WAV file format at a sampling rate of 44,100 Hz with 16-bit resolution. All recordings were completed in an anechoic chamber (> 30 dB noise reduction) with all ulterior sound sources being silenced during the recording.

The recorded data was then pre-processed and normalized using the procedure mentioned in our previous work [3] [24]. First, each recording was manually investigated in the time–frequency domain to exclude artifacts, vocal noises, tones, interruptions or very low signal-to-noise ratio compared to the background noise. Next, recordings were band-pass filtered (75– 20000 Hz) with a Butterworth filter of 4th order. As well, each signal was normalized to its energy to remove the effect of plausible airflow fluctuation between the breathing cycles [3].

The power spectra of the normalized data were then estimated using the Welch method with a window size of 1024 samples (~23.22 ms) and 50% overlap between the adjacent windows. The average power spectrums are thus presented and evaluated in the following pages.

4.4.2. Results

The power spectra for the audio signal collected by the selection of electret condenser microphones during both inspiration (Fig. 4.3) and expiration (Fig. 4.4) when tested by the procedure described above are presented. Normal tracheal breathing sounds, when recorded on the surface of the skin over the suprasternal notch, are described as broad spectrum, covering a frequency range from less than 100 Hz to greater than 3,000 Hz [12]. The characteristic power spectrum exhibits relatively high amplitude until a sharp decline occurring at approximately 900 Hz [4]. The relative peaks and troughs of the power spectrum have been explained as a result of resonances related to airway dimensions and gas density in the upper airway [12]. As well, the power spectrum of normal tracheal sounds during inspiration exhibits only slight differences in the amplitude and the point of sharp decline as compared to that during expiration [4].

The frequency response of a microphone can be described as the inherent frequency-specific output sensitivity of the microphone that is a result of the microphone's design and construction. Ideally, a microphone that has optimal output sensitivity at all frequencies is desired. However, in practice, such a microphone is not possible to be constructed. Instead, manufacturers create microphones that exhibit an optimal output sensitivity for specific frequency range(s). In doing so, this results in a decreased output sensitivity at some other frequency range(s). Thus, for the respective power spectra plots for both inspiration and expiration, the differences of signal power observed for the selection of microphones is a direct result of each of the microphone's unique frequency responses.

To interpret the plots, the variations in the signal power relative to the frequency for each of the selected microphones are described and compared. The optimal microphone is the microphone that has the higher signal power. It can be noted from the plots that no one microphone performs best for all frequencies, each respective microphone performs slightly better or slightly worse at given frequencies compared to other microphones. Hence, a careful analysis was considered to select the microphone best suited to the intended application.

4.4.2.1. Comparison of Microphones for Inspiratory Sounds:

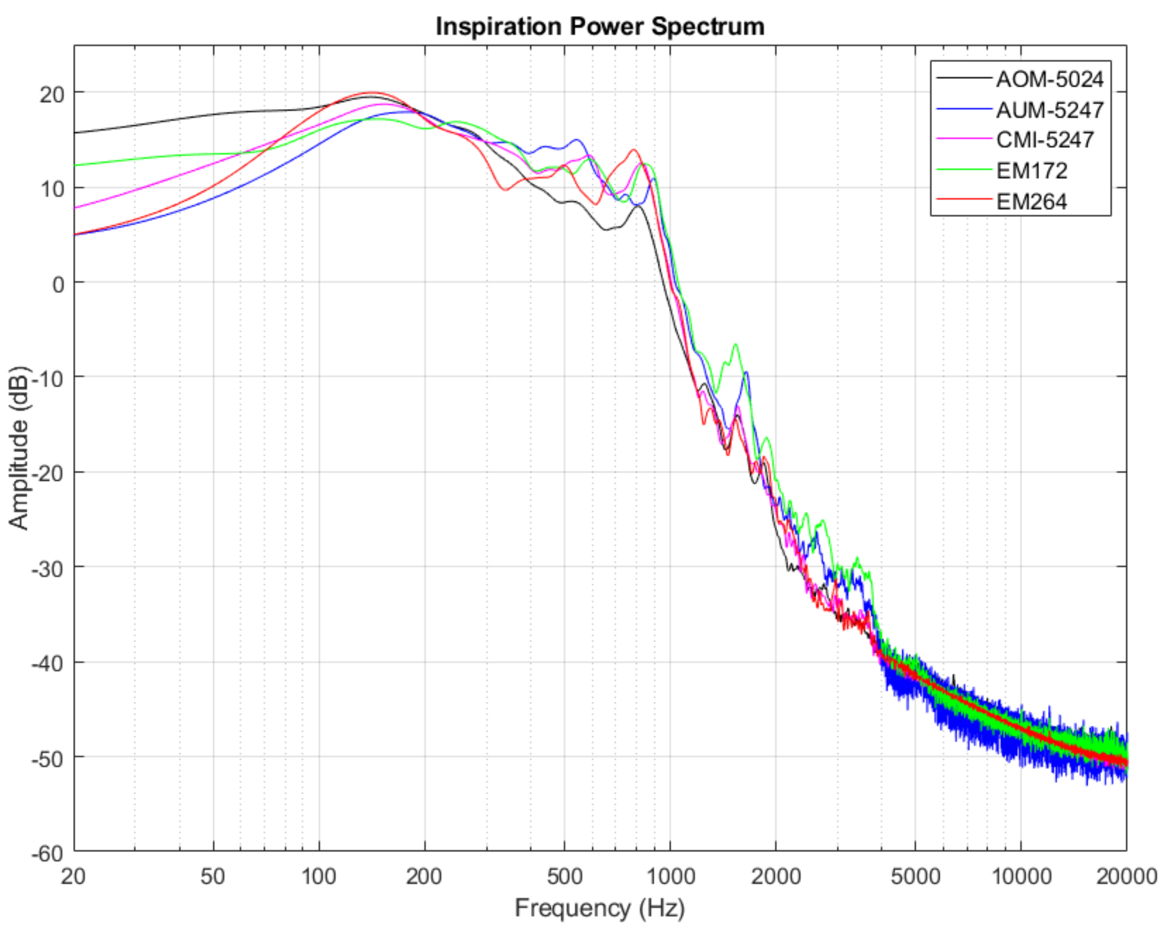

Figure 4.3. Microphone response captured during inspiration showing the response of various microphones.

AOM-5024: The low frequency components, up to 105 Hz, are best captured by this microphone. Up to 300 Hz, the AOM-5024 still displays near to the best response; however, past 300 Hz, a sharp decline in response is observed and the microphone shows decreased power relative to the other microphones. From 400 – 1100 Hz, the AOM-5024 shows the lowest signal power of all microphones. Following from 1100 Hz, the AOM-5124 continues to display lower performance with signal power being the lowest or near to the lowest relative to the other microphones throughout the higher frequencies and remainder of the spectrum.

AUM-5247: This microphone shows near to the lowest relative signal power at frequencies below 100 Hz; however, this microphone's response increases sharply past 100 Hz and displays the highest power of all the microphones between 350 – 650 Hz. After which, the response decreases slightly compared to the other microphones, but has good signal power (second best) past 1000 Hz, with only the EM172 microphone displaying improved response past 1000 Hz in comparison (aside from two minor regions where the AUM-5247 signal power is best: 1620 – 1700 Hz and 1710 – 1790 Hz).

CMI-5247: The microphone shows moderate signal power relative to other microphones at frequencies below 100 Hz. Much like the AUM-5247, this microphone's response increases sharply past 100 Hz and displays relatively high signal power between 350 – 650 Hz (though not as good as the AUM-5247), but from 700 – 870 Hz shows noticeable improvement in response with higher signal power compared to the AUM-5247. Past 1000 Hz, this microphone shows lower performance with signal power remaining near to the lowest relative to the other microphones throughout the higher frequencies and remainder of the spectrum.

EM172: Although this microphone initially shows relatively moderate signal power at frequencies below 100 Hz, its response decreases for the small range between 130 – 200 Hz and shows the lowest signal power of all microphones for that range. Past 200 Hz, the microphone's response increases sharply, and it has the best response of all microphones between 230 – 350 Hz. Past 350 Hz, the EM172 remains a good choice with response very similar to the CMI-5247 up to 850 Hz. Following from 850 Hz, the EM172 shows the highest signal power of all microphones and continues to perform very well with higher signal power relative to the other microphones throughout the higher frequencies and remainder of the spectrum (aside from two minor regions where the AUM-5247 signal power is best: 1620 – 1700 Hz and 1710 – 1790 Hz).

EM264: This microphone initially shows poor performance with lower relative signal power at less than 50 Hz; however, past 70 Hz, this microphone shows a dramatic increase in response and shows the best signal power of all mics between approximately 110 – 180 Hz. Past 200 Hz the microphone's response decreases and shows the second-lowest signal power. Another sharp increase is seen again around 650 Hz, at which point the EM264 once again shows the optimal response between 650 – 830 Hz. Continuing past 1000 Hz, the EM264 shows similar response as the CMI-5247 which along with the AOM-5024 form the 3 least optimal performing microphones in this range.

4.4.2.2. Comparison of Microphones for Expiratory Sounds

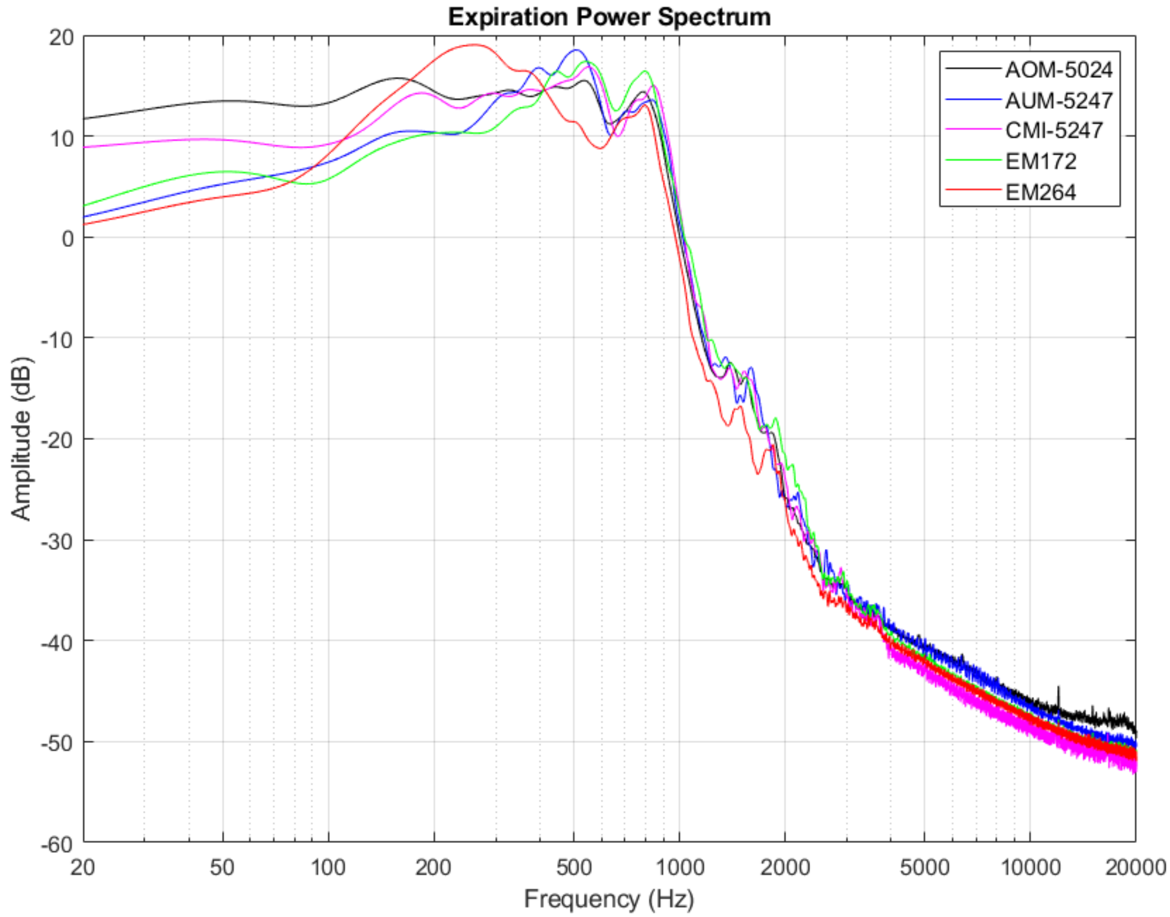

Figure 4.4. Microphone response captured during expiration showing the response of various microphones.

AOM-5024: Much like during inspiration, this microphone has the optimal response for capturing low frequency components, namely below 170 Hz. Past 170 Hz, the response of the microphone is moderate remaining relatively flat until 600 Hz. The response increases greatly between the range of 600 – 800 Hz showing the second-highest signal power of all microphones where only the EM264 performs better. From 800 Hz through to approximately 2000 Hz, the AOM-5024 shows relatively moderate response again generally in between the best and worst signal tracings. Yet, past 2000 Hz, the microphone proves to provide good signal power and past 10,000 Hz is observed to provide the highest signal power.

AUM-5247: This microphone shows the second-worst response at frequencies below 70 Hz. This microphone's response increases steadily from 100 – 380 Hz and displays the highest sensitivity of all the microphones between 380 – 550 Hz. Following 550 Hz, the sensitivity decreases rather sharply relative to the other microphones, and then performs moderately from approximately 800 – 1400 Hz. Following from 1400 Hz the response of the AUM-5247 steadily increases. Past 2000 Hz the increasing trend continues the microphone performs second-best behind the EM172. Finally, from 4000 Hz onwards, the microphone exhibits near-to the best performance along with the AOM-5024 until the AOM-5024 is observed to provide the clearly greater signal power past 10,000 Hz.

CMI-5247: This microphone starts out with the second-best response until 110 Hz and then forms the middle ground with a moderate response until approximately 600 Hz. From 650 – 710 Hz this microphone shows the least optimal response with the lowest signal power. Following, the microphone's response sharply increases and shows the best response of all microphones from 850 – 1000 Hz. From 1000 Hz through until 4000 Hz the microphone shows moderate to good response, however, the CMI-5247 shows the lowest signal power past 4000 Hz and onwards.

EM172: This microphone demonstrates near-to the lowest signal power at frequencies below 250 Hz. Following from 250 Hz, the microphone's response increases sharply and between 550 – 840 Hz has the best response of all microphones. From 1030 – 1160 Hz, 1200 -1300 Hz, and 800 – 2400 Hz, the EM172 once again demonstrates the overall best response with highest signal power of all the microphones. Past 2500 Hz, the EM172 remains an excellent choice with near-to the best response until 4,000 Hz where past this point the AOM-5024 and AUM-5247 both perform slightly better.

EM264: Like the EM172, this microphone initially has poor response in less than 80 Hz; however, past 80 Hz, this microphone shows a sharp increase in response and even demonstrates the best response of all mics between approximately 170 – 380 Hz. Past 380 Hz the microphone response takes a sharp decline and demonstrates the worst response of all microphones from 415 - 640 Hz. The microphones response increases slightly from 640 – 710 Hz but remains less than optimal. Following from 710 Hz, the EM264 shows as the least optimal microphones with the lowest signal power for the range of 710 – 3850 Hz (aside from the small region 1800 – 2000 Hz where the AUM-5247 shows slightly lower signal power). From 3850 Hz onwards, the EM264 is the shows the second-worst response with only the CMI-5247 showing lower signal power.

4.4.3. Conclusion

In conclusion, the results show clear differences for selecting an optimum microphone dependent upon the frequency range of interest. For recording low frequency components (i.e., < 150 Hz), likely the AOM-5024 or the CMI-5247 are the best choice of microphone. For recording higher frequency components (i.e., > 1000 Hz), either the AUM-5247 or the EM172 are the best choice. And for recording in the mid-range (i.e., 150 – 1000 Hz), likely the EM264 would be the best choice.

Following the evaluation of the selection of microphones described above it was decided to proceed with the **Primo EM172** microphone for the remainder of this research to be used with the Audio Recorder device. The Primo EM172 was selected for its high performance in the higher frequency range which is complimentary to the secondary objective of the research regarding the investigation of tracheal breathing sound spectral components with frequency greater than 5 kHz. Although the PUI Audio Inc. AUM-5247L-C3310-R proved to perform well at the higher frequency range, the Primo EM172 was selected in favor of the PUI Audio Inc. AUM-5247L-C3310-R for its exceptional properties, namely its higher sensitivity (-28 dB in favor of -47 dB) and increased SNR (80 dB in favor of 55 dB).

Figure 4.5. Primo EM172 electret condenser microphone backside (left) and front (right) shown.
Source: [51]

4.5. Microphone Driver Circuit

An additional design aspect regarding implementation of the microphones requires the use of a simple circuit to appropriately power and operate each microphone, aptly named the Microphone Driver Circuit. The Microphone Driver Circuit is required to power the internal FET circuitry within the microphone and is described by the technical data/usage instructions document provided by the manufacturer of each microphone. The technical data sheet details the components required and the appropriate electronic circuit diagram but leaves it up to consumers to implement the circuit. As such, this section details the fabrication of the Microphone Driver Circuit that is used with the implementation of the Primo EM172 microphones as part of the Audio Recorder.

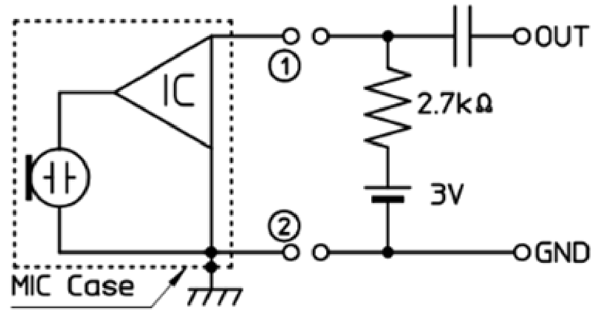

Figure 4.6. Microphone Driver Circuit as illustrated by the technical data sheet for the Primo EM172 electret condenser microphone. Source: [49]

Figure 4.6 illustrates the Microphone Driver Circuit as described within the technical data sheet for the Primo EM172 electret condenser microphone. As can be noted from Fig. 4.6, the microphone has two terminals to which the Microphone Driver Circuit connects. As part of the Microphone Driver Circuit are two passive components: a 2.7 kΩ resistor and a capacitor. As well, the Microphone Driver Circuit requires a 3V (DC) voltage source and a connection point to ground.

Terminal 2 is supplied with a connection to ground, which provides the reference voltage for the microphone as well as the reference for the voltage source. Terminal 1 is used to supply DC voltage to the microphone and serves as the output terminal from which the audio signal is captured. The voltage source is connected to terminal 1 through a 2.7 kΩ resistor where the resistor acts to limit the current supplied to the internal microphone circuitry. As well, a capacitor with one lead connected to terminal 1 of the microphone in conjunction with the resistor forms a high-pass filter which acts to block DC components of the output of terminal 1, thereby separating the audio signal from the DC supply voltage. Since an appropriate value for the capacitor was not explicitly stated by the manufacturer, the value of 1 μF was chosen based upon filter theory for a resistor-capacitor (RC) filter for the high-pass configuration. The mathematical expression for the filters cut-off frequency of the RC high-pass filter is described by Eq. 3 below:

$$\text{Filter Cut-off Frequency } f_c = \frac{1}{2\pi(R)(C)} \qquad \text{(Eq. 3)}$$

where f_c is the cut-off frequency (in Hz) of the filter, R corresponds to the resistance value of the resistor, and C corresponds to the capacitance value of the capacitor. Since the value of R is provided as 2.7 kΩ, and it is desired to utilize the full frequency range of the microphone (from 60 Hz – 20 kHz), C is calculated as 0.982 μF when f_c is 60 Hz. The closest standard value to the result for C is 1 μF, which was used in the Microphone Driver Circuit.

A custom printed circuit board (PCB) (Dimensions: 12.8 mm diameter x 1.00 mm thickness) was designed in a PCB design software suite to implement a compact and robust basis for the Microphone Driver Circuit, the rendering of which is shown in Fig. 4.7:

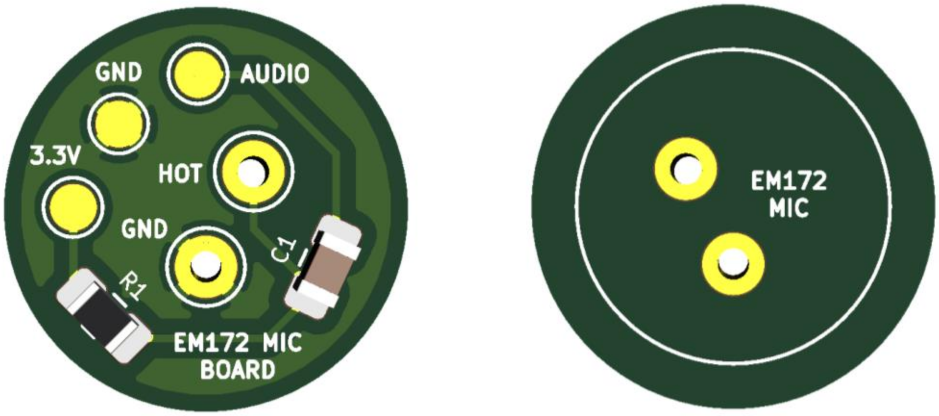

Figure 4.7. Custom designed printed circuit board (PCB) to implement the Microphone Driver Circuit. Front view (left) and back-side view (right).

The PCB incorporates solder pads for the installation of surface mount components, namely the resistor and capacitor, denoted by R1 and C1. As well, the PCB incorporates two plated through holes denoted as “HOT” and “GND” (corresponding to the Primo EM172 microphone terminals, i.e., terminal 1 and terminal 2, respectively) to which male pins that have been soldered to the terminals of the Primo EM172 microphone protrude through the PCB and subsequently the pins are soldered to the plated through holes. Finally, the PCB has circular solder pads labelled as “3.3V”, “GND”, and “AUDIO” to which the individual conductors from a 3-wire cable are soldered to make a connection to the Audio Recorder via the cable. Assembling the PCB to the microphone, the backside of the PCB is designed to sit flush against the back of the Primo EM172 microphone and makes an extremely compact yet functional design.

The PCB design was realized via production by a PCB manufacturer as the process requires highly specialized manufacturing equipment. Following production of the PCB, the circuit was then hand-fabricated to achieve the final working state. Firstly, the two surface-mounted devices (SMDs), namely the resistor (Manufacturer: Yageo, Product Number: RT0805BRD072K7L, Resistance:

2.7 kΩ) and capacitor (Manufacturer: AVX Corporation, Product Number: TAJR105M020RNJ, Capacitance: 1 μF), were precisely soldered to the solder pads on the PCB for each respective SMD. Next, male printed circuit (PC) pins (Manufacturer: Mill-Max Manufacturing Corp., Product Number: 9137-0-00-15-00-00-38-0, Diameter: 0.46 mm) were soldered to the two terminals on the back of the Primo EM172 microphone. After which, the male PC pins affixed to the EM172 microphone were routed through the two plated through holes of the PCB such that the back of the EM172 microphone was flush with the back of the PCB. Once the microphone was in position flush with the PCB, the protruding male PC pins were soldered to the plated through holes and the remaining unnecessary length of the PC pins cut flush with the top of the solder joint to the PCB.

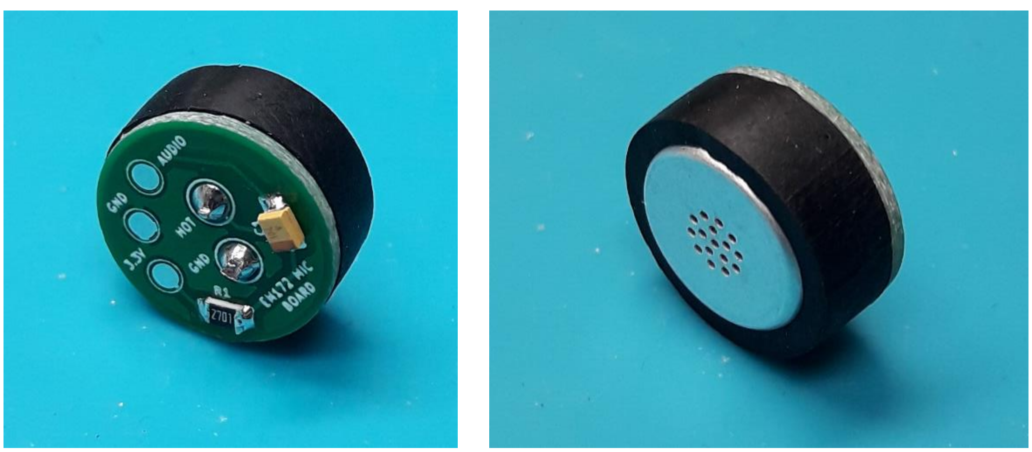

Figure 4.8. Primo EM172 microphone with Microphone Driver Circuit PCB attached. Left shows the back/side profile view, where right shows the front/side profile view. Note: rubber isolator ring (the use of which described by Chapter 5 of this report) is shown around microphone.

The microphone-and-PCB assembly was then connected to a 3-conductor shielded cable (Manufacturer: Tensility International Corp, Product Number: 30-00278, Diameter: 32 AWG) to permit connectivity to the Audio Recorder. The individual conductors of the 3-conductor shielded cable were soldered to the solder pads labelled as “3.3V”, “GND”, and “AUDIO” correspondingly and the opposite end of the 3-conductor shielded cable finished with a 3.5 mm male stereo connector (Manufacturer: Neutrik, Product Number: NYS231BG). When the 3.5 mm male stereo connector is attached to the 3.5 mm female stereo connector on the Microphone Power Supply Board, the Microphone Driver Circuit is provided with a 3.3V voltage source, a connection point to ground, and a connection point to route the audio output signal to the Audio Interface Board.

Figure 4.9. Microphone Coupler with protective cap removed showing the internal connections to the Microphone Driver Circuit PCB attached.

Chapter 5

5. Microphone Coupler & Air-Chamber

5.1. Introduction

When using a microphone to capture respiratory sounds from the skin's surface, a volume of air between the surface of the skin and the sensing element of the microphone is required as the air acts to convert upper airway and chest wall vibrations at the surface of the skin into sound pressure which is measurable by the microphone. A fixture known as a Microphone Coupler is used to allow attaching the microphone in place without touching the skin, and by creating a specifically designed cavity between the microphone and the skin (defined as an Air-Chamber) creates a sealed pocket of air between the microphone sensing element and skin surface. The geometry of the Air-Chamber plays a crucial role in being able capture the optimal response as the air medium acts like a filter. Thus, an appropriate Air-Chamber must be designed to ensure the desired signal components can be collected by the microphone. This chapter explains the design for an appropriate Microphone Coupler and Air-Chamber for respiratory sound recording by the ASAD-III device.

5.2. Design Specifications

The Microphone Coupler and Air-Chamber must be designed to physically accommodate the microphone and be comfortable for the subject. Specifically, the coupler should permit easy and secure attachment to the skin and should also act to position the sensing element of the microphone correctly with the base of the Air-Chamber. Equally as important, the effect of the Air-Chamber should benefit the recorded signal by permitting the full frequency range of the chosen Primo EM172 microphone (60 – 20,000 Hz) having the desired effects of optimal sensitivity at a relatively wide (> 5 kHz) frequency range for sound collection. The Microphone Coupler and Air-Chamber design specifications are summarized in Table 5.2-1 below:

Table 5.2-1. Microphone Coupler/Air-Chamber Specifications

Feature:	**Value or Range:**	**Explanation:**
Compatibility	Primo EM172 Capsule-Style Electret Condenser Microphone	Coupler should securely hold the microphone of this style.
Placement	Suprasternal Notch & 2nd intercostal space of the right lung	Anatomical locations to which the Microphone Coupler will be attached.
Frequency Range	60 – 20,000 Hz	Air-Chamber should permit the full frequency range of the microphone.

5.3. Design

As a first iteration (i.e., Revision 1), the Microphone Coupler was custom-designed and manufactured from a single, solid piece of ultra-high-molecular-weight polyethylene (UHMWPE). The coupler began as UHMWPE rod stock and was cut to the desired dimensions via a machinist's lathe. The Air-Chamber was cut into the front surface of the coupler, whereas on the backside a counter-bore hole was cut to mount and position the microphone correctly with the base of the Air-Chamber. In addition, the flat surface on the front of the coupler surrounding the Air-Chamber was designed to accommodate double-sided adhesive discs (Manufacturer: 3M, Product Number: 2181), traditionally designed for attaching Littmann Stethoscopes to the skin. The 3M double-sided discs provide excellent adhesion for secure attachment and additionally utilize a hypoallergenic adhesive reducing the overall risk of allergic reaction.

Figure 5.1. Revision 1 design of the Microhone Coupler shown affixed at the suprasternal notch for recording tracheal sounds.

The design of the Air-Chamber was firstly divided into three dimensional properties:

i. Diameter at the bottom of the Air-Chamber (i.e., the aperture at the microphone capsule).
ii. Diameter at the top of the Air-Chamber (i.e., the aperture at the surface to be in contact with the skin).
iii. Depth of the Air-Chamber.

The diameter of the aperture at the bottom of the Air-Chamber was selected as 4.85 mm to allow full exposure of the entry ports to the Primo EM172 microphone capsule without obstruction. This dimension is fixed throughout the different Microphone Coupler revisions. The Air-Chamber dimensions for the diameter of the aperture at the skin and the depth of the Air-Chamber are less straight forward in selection. Careful review of previous designs in the literature reveals two competing factors act to maximize the sensitivity of the microphone. Firstly, a small air cavity is desired to have an increased air pressure which results in increased sensitivity at the microphone. Secondly, a maximal aperture diameter (at the surface of the skin) is desired to capture the maximal amount of vibration at the skin surface resulting in higher signal power.

The Air-Chamber depth was selected as 2.60 mm from the recommendations presented previously in [25] where it is clear that sensitivity decreases, especially at higher frequencies, with increasing air-cavity depth which is undesirable. The depth of 2.60 mm is consistent with the Air-Chamber design used within the Microphone Evaluation section described by this report. Furthermore, the Air-Chamber depth of 2.60 mm is fixed throughout the different Microphone Coupler revisions and thus allows for the optimization of the optimal aperture diameter (at the surface of the skin).

The diameter of the aperture at the top of the conical Air-Chamber was established based upon the observation that conical Air-Chambers have been shown to provide 5 to 10 dB more sensitivity than cylindrical Air-Chambers of the same diameter [26]. A conically shaped Air-Chamber design was chosen where the angle of the walls (with respect to center axis of the coupler) was initially selected to be 45°. This resulted in a diameter of the aperture at the top of the Air-Chamber of 10.00 mm. In addition, chambers with diameters of the aperture at the top of the Air-Chamber of 12.50 mm, and 15.00 mm (chamber wall angles of approximately 56°, and 62.5°, respectively) were also fabricated. The three different Air-Chambers with Revision 1 specifications (i.e., each with identical diameter of the aperture at the bottom of the Air-Chamber = 4.85 mm, depth = 2.60 mm, and varying diameter of the aperture at the top of the Air-Chamber: 10.00 mm, 12.50 mm, and 15.00 mm) were then tested and evaluated.

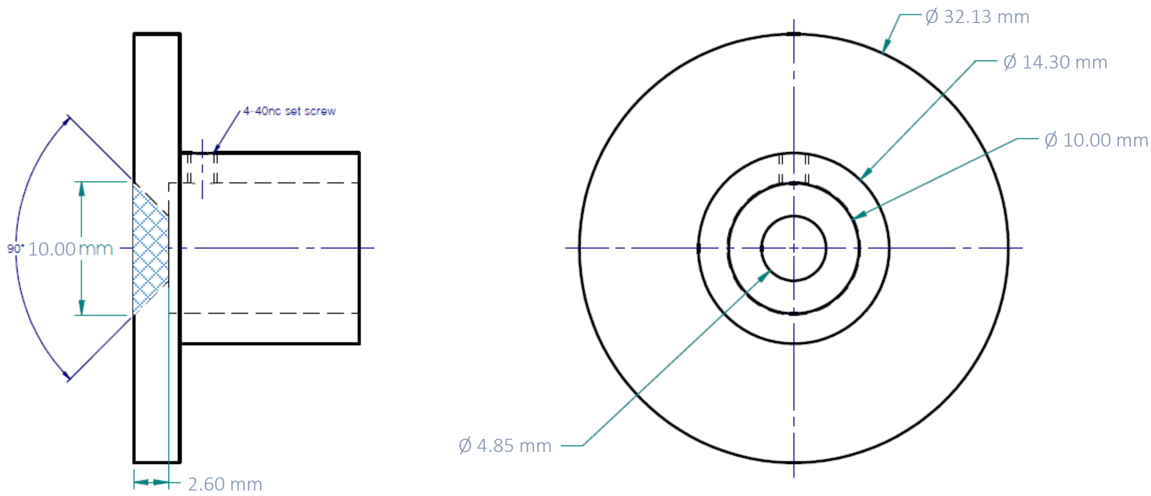

Figure 5.2. Revision 1 drawing of microphone coupler, 10.00 opening diameter shown. Cross-sectional view (left), backside view (right). Air-Chamber is shown by cross-hatched region.

The Revision 1 coupler design, described above, placed the microphone capsule in direct contact with the UHMWPE material of the coupler with no damping or sound isolation. Additionally, the Revision 1 design utilized a small 4-40 (NC) thread nylon setscrew to secure the microphone within the coupler. Since the end goal for this ASAD-III recording device is to use tracheal breathing sounds analysis as a diagnostic screening tool, it must be robust enough to perform well in different environments and conditions such as recording during wakefulness and sleep. Therefore, the next revision (i.e., Revision 2) to the Microphone Coupler design incorporates a slightly larger (12.80 mm) counter-bore hole to accommodate a rubber isolator ring (Manufacturer: Micbooster, Product Number: FC037, Material Thickness: 1.5 mm) around the perimeter of the capsule of the microphone to help dampen background noise from reaching the microphone capsule.

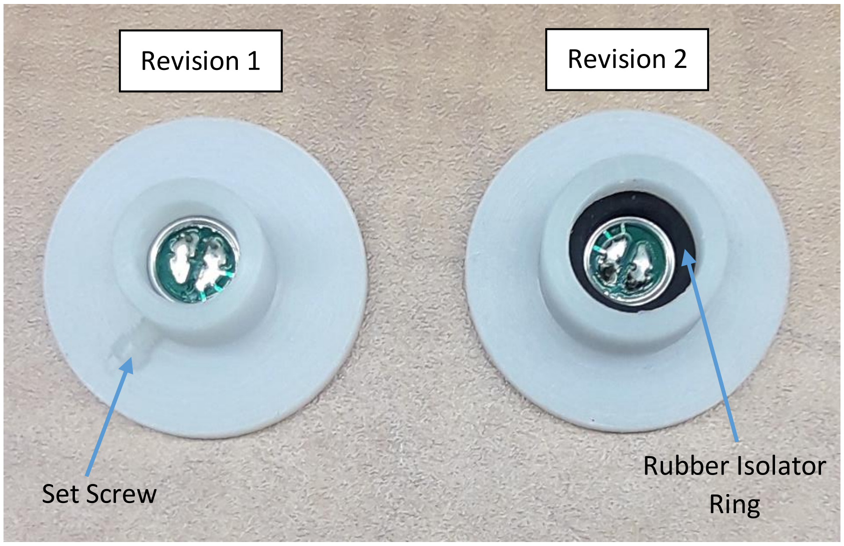

Figure 5.3. Microphone coupler Revision 1 design (left), Revision 2 design (right), both with microphone inserted.

Using the isolator ring, the metal body of the microphone capsule is no longer in direct contact with the UHMWPE material of the coupler. Due to the snug-fit with the rubber isolator, the setscrew was no longer required and removed in the Revision 2 design for the Microphone Coupler.

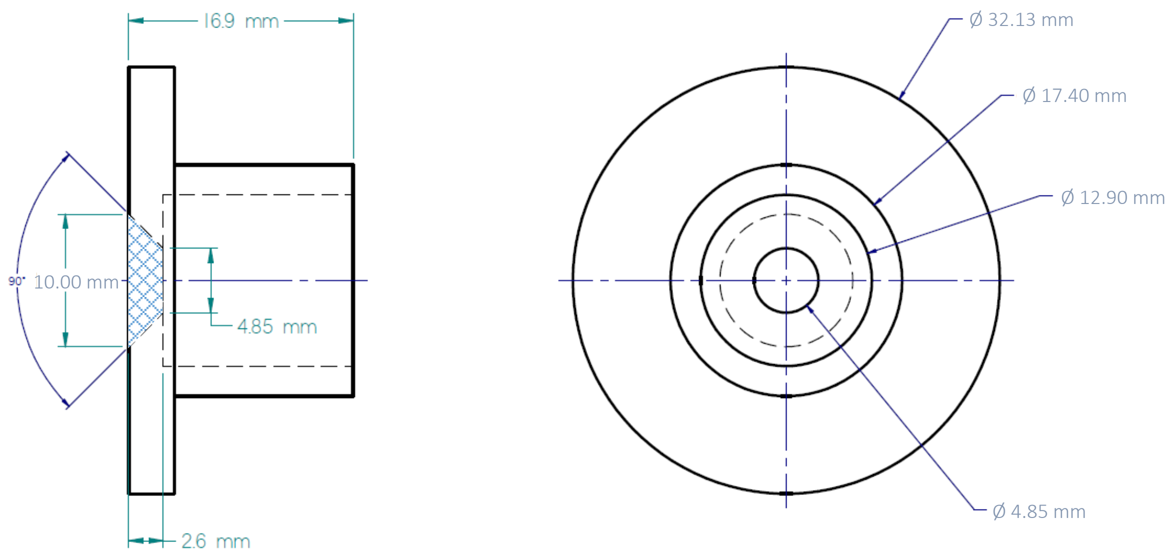

Figure 5.4. Revision 2 drawing of microphone coupler, 10.00 opening diameter shown. Cross-sectional view (left), backside view (right). Air-Chamber is shown by cross-hatched region.

An important result was observed when testing the Revision 2 design, namely the high frequency signal components around 5 kHz became damped with the use of the rubber isolator ring. Since the breathing sound signal has considerably low power at this frequency range, a design change was considered to investigate whether an increase in sound pressure could help to increase the signal power especially around 5 kHz. The design change consisted of changing the Microphone Coupler material to a material of greater hardness, since harder materials act to absorb less sound energy. With a harder material, less of the sound's energy within the Air-Chamber would be absorbed by the material and thus a slightly higher sound pressure should reach to the microphone diaphragm and effectively increase the signal power.

Our third revision design (i.e., Revision 3) utilized the process of fused deposition modelling via 3D printing to construct the Microphone Couplers with the material polylactic acid (PLA). The material hardness of the PLA and the previous UHMWPE were carefully considered. The PLA material used has a hardness of 80 (Shore D), whereas the UHMWPE had a material hardness of approximately 70 (Shore D), indicating that the PLA material is slightly harder than the UHMWPE and thus should act to absorb less sound energy, especially within the Air-Chamber.

Compared to Revision 2, the Revision 3 design of the Air-Chamber remained identical in dimensions, and the new Microphone Coupler design also included the use of the rubber isolator ring positioned around the circumference of the microphone capsule. However, the design of the Microphone Coupler was refined to make it more comfortable to wear and to be more robust. Firstly, the overall outside diameter of the coupler was decreased from 32.13 mm to 26.00 mm to make use of smaller diameter double-sided adhesive discs (Manufacturer: Gereonics, Product Number: 450092, Outside Diameter: 25.70 mm). As well, the back of the Microphone Coupler was revised to include provisions for a protective cover to enclose the counter-bore hole on the back side of the coupler. The protective cover was printed separately from the coupler and via the provisions in the coupler slides into position to ensure the delicate electrical circuit contained inside the counter-bore hole remains protected.

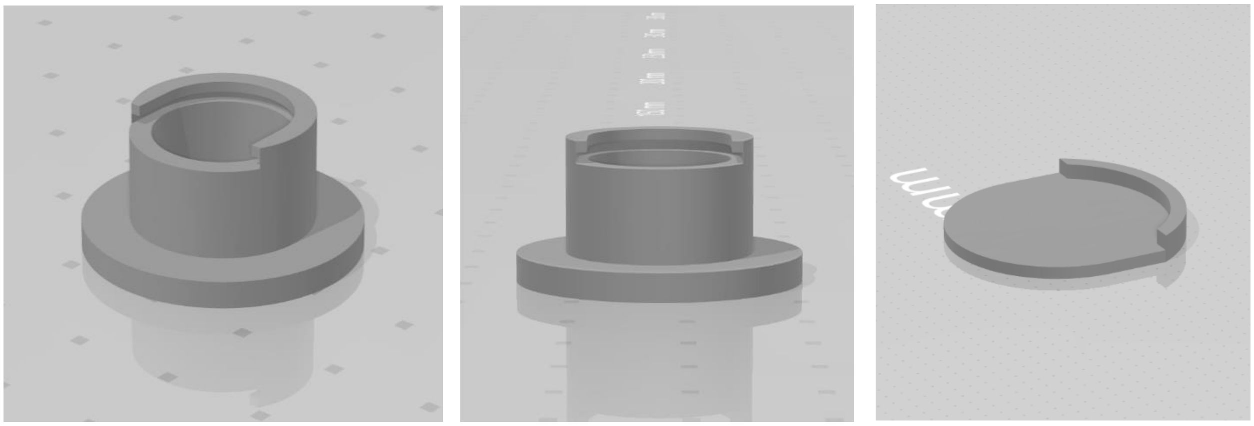

Figure 5.5. Microphone coupler Revision 3 design model (left and middle), Coupler cap model (right).

For this design, the microphone shielded connection cable (Manufacturer: Tensility International Corp., Product Number: 30-00278) was also directed to come out of the side of the Microphone Coupler at a 90° angle to aid in strain relief for the cable and increase its wearability, especially when placed under clothing. With these minor changes, the Revision 3 design of the Microphone Coupler has an overall height of just 13.00 mm making it comfortable and unobtrusive to wear even for an extended period of time during sleep.

Figure 5.6. 3D printed microphone couplers (left) and showing how the protective cover is removed for access to the microphone and circuit components inside (right).

5.4. Evaluation

Similar to the evaluation procedure for microphone selection, all recordings regarding the microphone Air-Chamber were completed in an anechoic chamber (> 30 dB noise reduction) with all ulterior sound sources being silenced during the recording. For all tests, the same microphone was utilized to record. Additionally, for all tests the Microphone Coupler was affixed to the skin over the suprasternal notch of the trachea using double-sided adhesive rings to seal the Air-Chamber to the skin. While capturing data, for each respective recording the subject was guided by the researcher to follow a breathing pattern that consisted of 5 complete breathing cycles at his normal flow rate breathing through the mouth with a nose clip in place followed by a 5-second breath-hold at the end to have a measure of background noise. Signals were recorded at 44.1 kHz sampling rate. Post-recording analysis included filtering the breathing sounds with a band-pass (75– 20000 Hz) filter (Butterworth) of 4^{th} order. Afterwards, each respiratory phase signal was normalized to its energy to compensate for the plausible airflow fluctuation between the breathing cycles [3].

The power spectra of the normalized data were then estimated using the Welch method with a window size of 1024 samples (~23.22 msec) and 50% overlap between the adjacent windows. The average power spectrum was generated for each respiratory phase (inspiration and expiration) and for the varying aperture diameter at the top of the Air-Chamber (10.00 mm, 12.50 mm, and 15.00 mm), addition of the rubber isolator ring, and finally for the Revision 3 Microphone Coupler fabricated by additive manufacturing. The variations in the signal power relative to the frequency for each of the Air-Chamber designs are described and compared.

5.4.1. Air-Chamber Opening Diameter

Investigation of the optimal opening diameter of the Air-Chamber for capturing tracheal breathing sounds was determined utilizing the design described by Revision 1 for the Microphone Coupler with Air-Chamber. Figures 5.7 and 5.8 display the power spectra of the inspiratory and expiratory phases, respectively, for the electret condenser microphone when used in conjunction with the three Air-Chambers of aperture diameter at the top of the air chamber of 10.00 mm, 12.50 mm, and 15.00 mm as tested by the procedure described above.

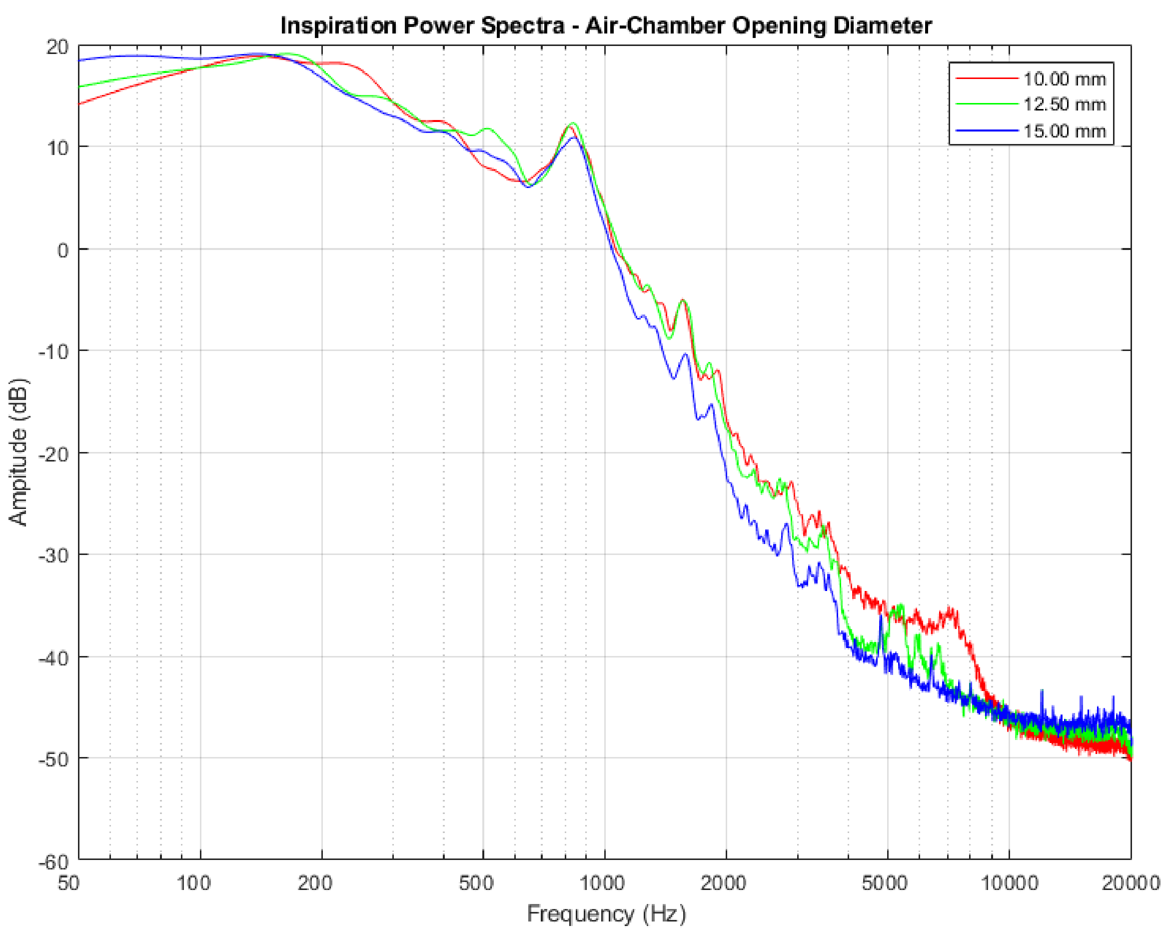

Figure 5.7. Microphone Air-Chamber response captured during inspiration showing the effect of the varying Air-Chamber opening diameter dimensions.

During the inspiratory phase (Fig. 5.7), below 150 Hz, the 15.00 mm chamber provides the best response with the highest signal power. On the other hand, below 150 Hz, the Air-Chamber design of opening aperture 10.00 mm displays the lowest signal power, and the 12.50 mm chamber design displays moderate signal power between the 15.00 mm and 10.00 mm signal tracings. At 150 Hz, the response of the three chamber designs converges and then following, the 10.00 mm chamber design shows an improved response and displays the highest signal power until 300 Hz. At the same time, the 15.00 mm chamber design shows a decline in response and shows the lowest signal power from 150 – 460 Hz. From 300 – 635 Hz, the 10.00 mm chamber design shows a sharp decline in response and shows the lowest signal power from 460 – 635 Hz. As well, from 430 – 600 Hz, the 12.50 mm chamber design shows a sharp increase in response and provides the highest signal power for this range. The three chamber designs converge in response at approximately 735 Hz. From 735 Hz, the 15.00 mm chamber design shows another decline in response and continues to display the lowest signal power up to 9500 Hz with as much as a 5.1 dB decrease in signal power observed relative to the 10.00 mm chamber design. From 735 – 2800 Hz the 10.00 mm and 12.50 mm chamber designs show a very similar response with marginal difference in signal power and numerous small regions in which the two chambers alternate with the optimal response. Following from 2800 Hz, a noticeable change is observed, and the 10.00 mm chamber response shows an increase with roughly 2 dB higher signal power observed relative to the 12.50 mm chamber design. The 10.00 mm chamber design continues to show the optimal response through to 9500 Hz, aside from the small range between 5200 – 5500 Hz where the 12.50 mm chamber design has higher signal power as a result of a sharp spectral peak. Following from 9500 Hz, the 10.00 mm chamber design experiences a sharp decline in response and displays the lowest signal power through to 20,000 Hz. Contrary, from 9500 – 20,000 Hz the 15.00 mm chamber design displays the highest signal power and the 12.50 mm chamber displaying a signal power in-between the response for the 10.00 mm and 15.00 mm chamber designs.

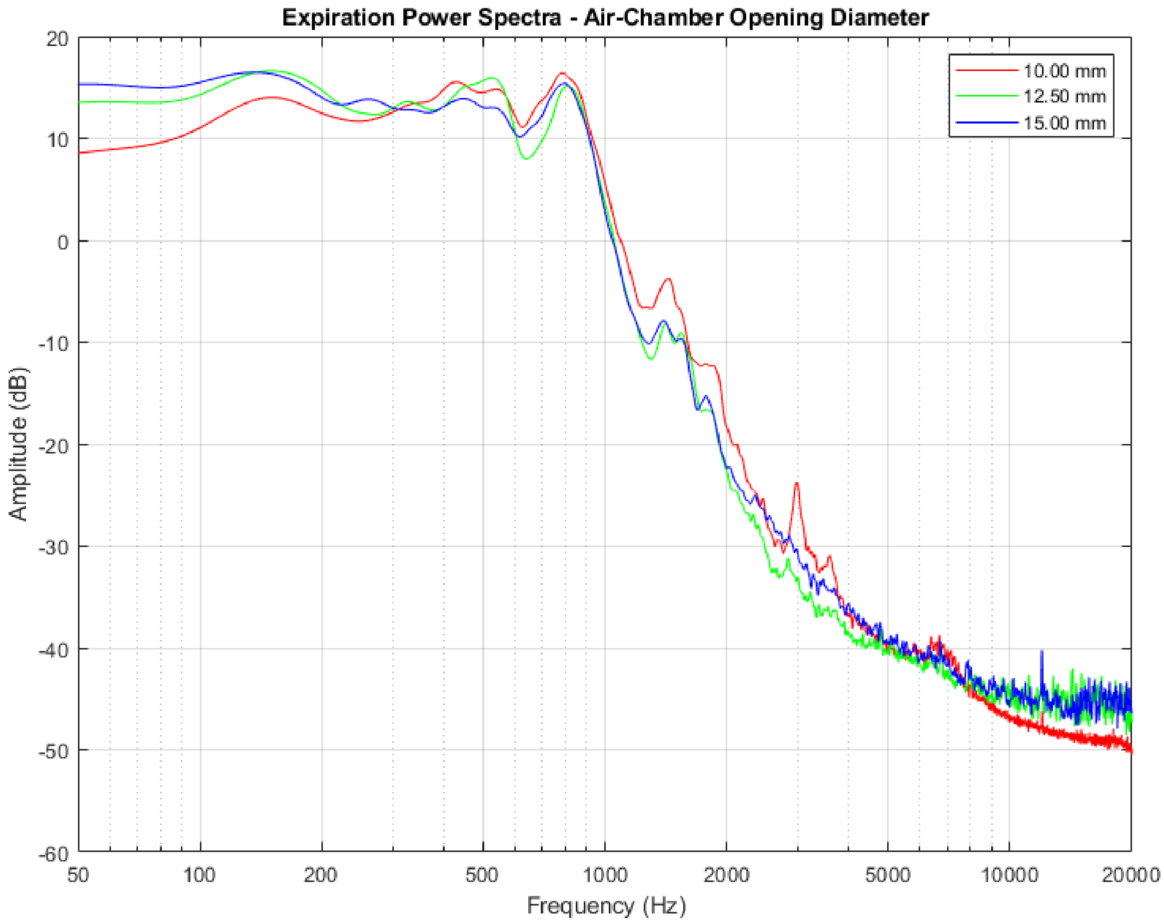

Figure 5.8. Microphone Air-Chamber response captured during expiration showing the effect of the varying Air-Chamber opening diameter dimensions.

During the expiratory phase (Fig. 5.8), similar to the trend observed for the inspiratory phase, below 140 Hz, the 15.00 mm chamber provides the best response with the highest signal power; the response of the 12.50 mm design relatively close behind and the 10.00 mm design showing the lowest signal power. At 300 Hz the response of the three chamber designs converges and then following, the response of the 15.00 mm design experiences a decline and displays the lowest signal power of the three designs from 300 – 600 Hz. From 340 Hz, the 10.00 mm chamber design displays a sharp increase in response with the highest signal power until 460 Hz. From 460 Hz to 560 Hz the 12.50 mm chamber experiences an increase in response displaying the highest signal power in this range. From 560 Hz through to 3900 Hz (aside from 2500 – 2830 Hz where the 15.00 mm chamber design displays slightly higher signal power), the 10.00 mm clearly shows the optimal response with as much as a 4.6 dB increase in signal power observed. On the other hand, from 560 Hz, the 12.50 mm chamber shows a sharp decline in response displaying the lowest signal power of the three designs until 820 Hz. From 820 Hz to 1200 Hz, the response of the 12.50 mm and 15.00 mm chamber designs remains relatively converged although the 12.00 mm chamber design shows marginally improved response. At 2000 Hz, a noticeable change is observed, and the 15.00 mm chamber design shows an increase in response near to the response of the 10.00 mm chamber design although the 15.00 mm chamber design fails to show similar spectral peaks as observed with the 10.00 mm chamber, namely around 3000 Hz. From 5000 Hz to 8000 Hz the response of the three chamber designs once again converge. Following from 8000 Hz, similar again to the trend observed during inspiration, the 12.50 mm and 15.00 mm chamber designs show a similarly higher signal power relative to the 10.00 mm chamber design.

5.4.2. Rubber Isolator Ring

Figures 5.9 and 5.10 display the response curves for the Air-Chamber design of 10.00 mm aperture diameter with and without the addition of the rubber isolator ring around the perimeter of the microphone during inspiration and expiration, respectively. The 10.00 mm chamber design was chosen to test the addition of the isolator ring because that design showed the most optimal response for the majority of the frequency range when testing the Revision 1 design. The Air-

Chambers both with and without the isolator ring were used to record tracheal breathing sounds, the power spectra generated, and the responses compared.

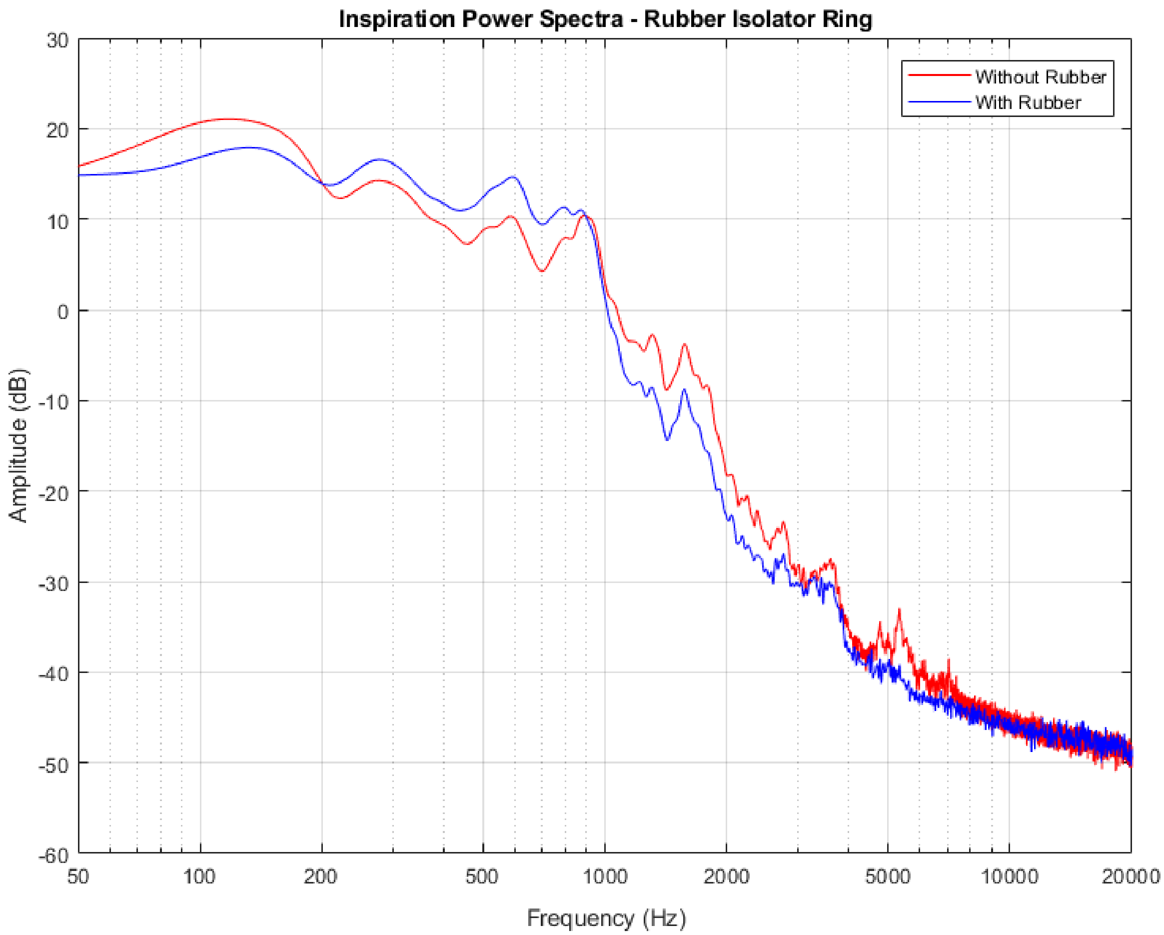

Figure 5.9. Microphone Air-Chamber response captured during inspiration showing the effect of the rubber isolator ring.

During the inspiratory phase (Fig. 5.9), prior to 200 Hz the Microphone Coupler design excluding the rubber insulator ring provides the better response. However, between approximately 200 – 900 Hz, the Microphone Coupler design including the rubber insulator ring provides a noticeably improved response with an increase in signal power up to 4 dB observed. Following past 900 Hz, the Microphone Coupler design without the rubber insulator once again provides the better response. At 3700 Hz, the response of the two designs briefly converges with near equal performance. Past 3700 Hz, the Microphone Coupler design excluding the rubber insulator continues to display the higher signal power until 10,000 Hz where the response of each chamber designs then shows as roughly equal through to 20,000 Hz.

Important to note are the spectral peaks near to 5 kHz that can be observed best with the coupler excluding the rubber isolator rings; namely at the frequencies: 4800 Hz, 5300 Hz, and 7000 Hz. The peaks are also somewhat visible with the chamber design including the rubber isolator ring but damped in amplitude and less apparent as a result.

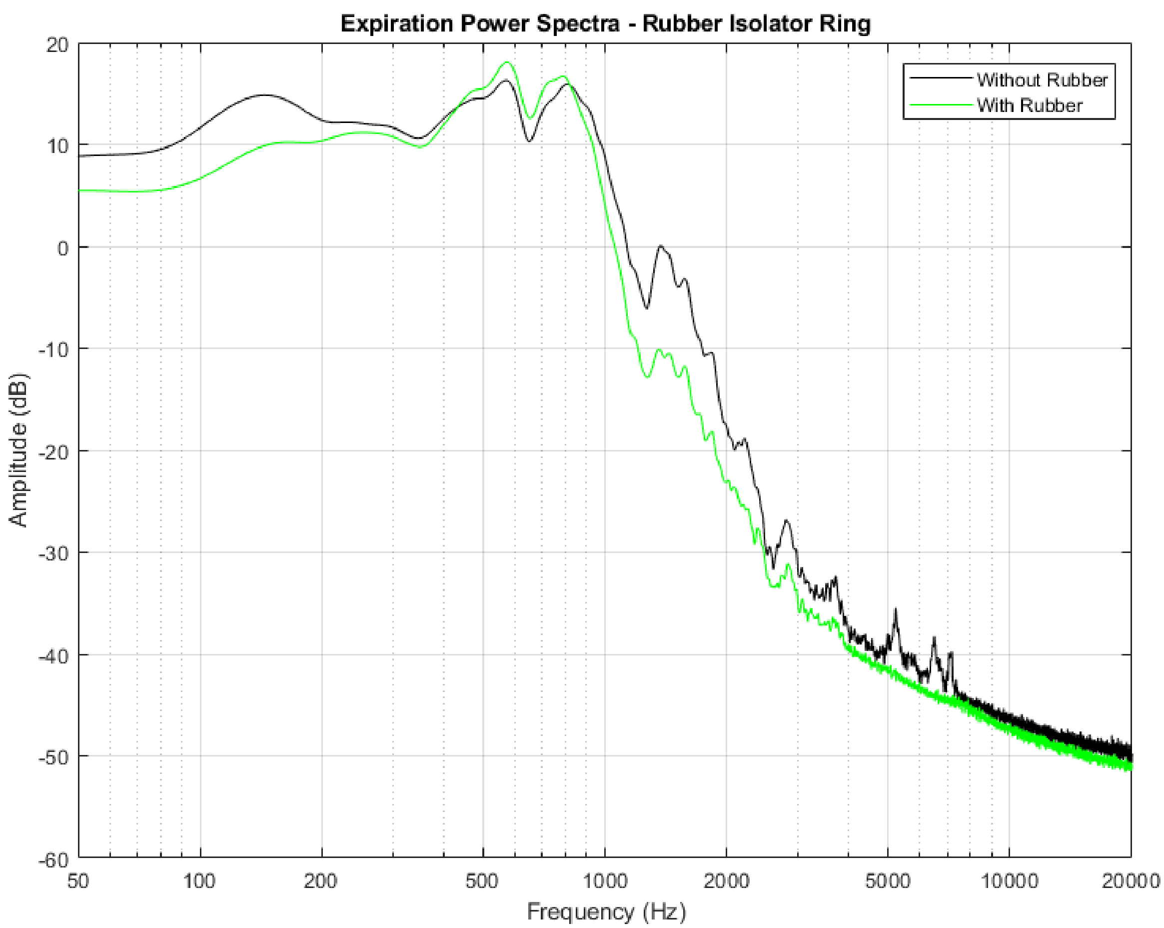

Figure 5.10. Microphone Air-Chamber response captured during expiration showing the effect of the rubber isolator ring.

During the expiratory phase (Fig. 5.10), prior to 435 Hz the Microphone Coupler design excluding the rubber insulator ring is observed to provide the more optimal response. However, between the range of 435 – 815 Hz, the Microphone Coupler design including the rubber insulator ring provides an improved response with an increase in signal power up to 2 dB relative to the design without the rubber insulator ring. Past 815 Hz, the Microphone Coupler design without the rubber insulator once again provides the more optimal response. The Microphone Coupler design excluding the rubber isolator ring continues to show the improved response through to the end of the spectrum. Once again, a feature to note are the spectral peaks near to 5 kHz that can be observed with the coupler excluding the rubber isolator ring, namely at the frequencies: 5200 Hz, 6500 Hz, and 7000 Hz. The spectral peaks are not visible with the chamber design including the rubber isolator ring.

5.4.3. Microphone Coupler Material

Investigation of the Microphone Coupler produced of PLA material via the technique of 3D printing was determined utilizing the design described by Revision 3 and comparatively assessed for performance to the Microphone Coupler produced of UHMWPE described by Revision 2. Figures 5.11 and 5.12, respectively shown on the following pages, display the power spectra of tracheal breathing sounds when recorded with the electret condenser microphone used in conjunction with the Microphone Couplers during inspiration and expiration described by the procedure mentioned above.

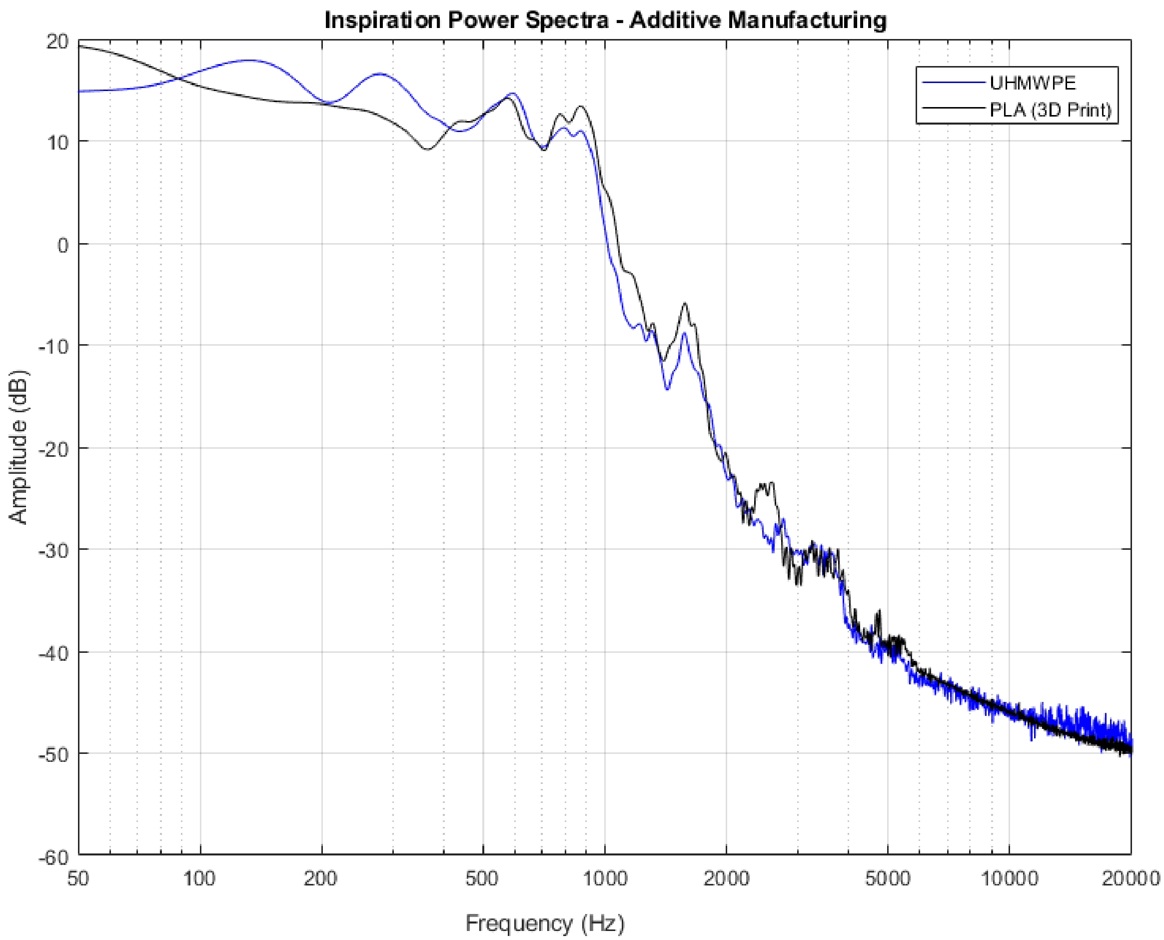

Figure 5.11. Microphone Air-Chamber response captured during inspiration showing the comparison of the UHMWPE material vs. the PLA material.

During the inspiratory phase (Fig. 5.11) prior to 90 Hz, the Microphone Coupler manufactured of PLA material provides the more optimal response. From 90 – 415 Hz, the Microphone Coupler of UHMWPE material provides better response. Between 415 – 730 Hz, the response of the two coupler designs matches quite closely with less than 1 dB difference in the amplitude observed. Following from 730 Hz, the PLA design shows a sharp increase in response and provides the better response with 3-4 dB increase in signal power observed. The responses for the two designs converge briefly at 1360 Hz, and then the PLA design shows again a 3-4 dB increase in signal power relative to the UHMWPE design until 1800 Hz. At 1800 Hz the response of the two designs converges again and the response of the two designs remain very similar until a sharp increase in response for the PLA design is observed from 2290 – 2700 Hz. Following from 2700 Hz, the PLA design shows a sharp decline in response and shows the lower signal power from 2700 – 3000 Hz. The response of the two designs converges for the range 3000 – 3700 Hz and following, the PLA design shows higher signal power through to 6500 Hz. Past 6500 Hz, the response of the two designs remains very similar for the remainder of the frequency spectrum, until 20,000 Hz.

As can be seen in Fig. 5.11, the response of the Microphone Coupler fabricated from PLA material shows higher signal power for much of the frequency spectrum, specifically within 700 – 6500 Hz. The spectral peaks near to 5 kHz that were previously damped and indiscernible using the rubber isolator ring are once again discernible with the use of the harder PLA material and can be noted at 4700 Hz and 5300 Hz, respectively.

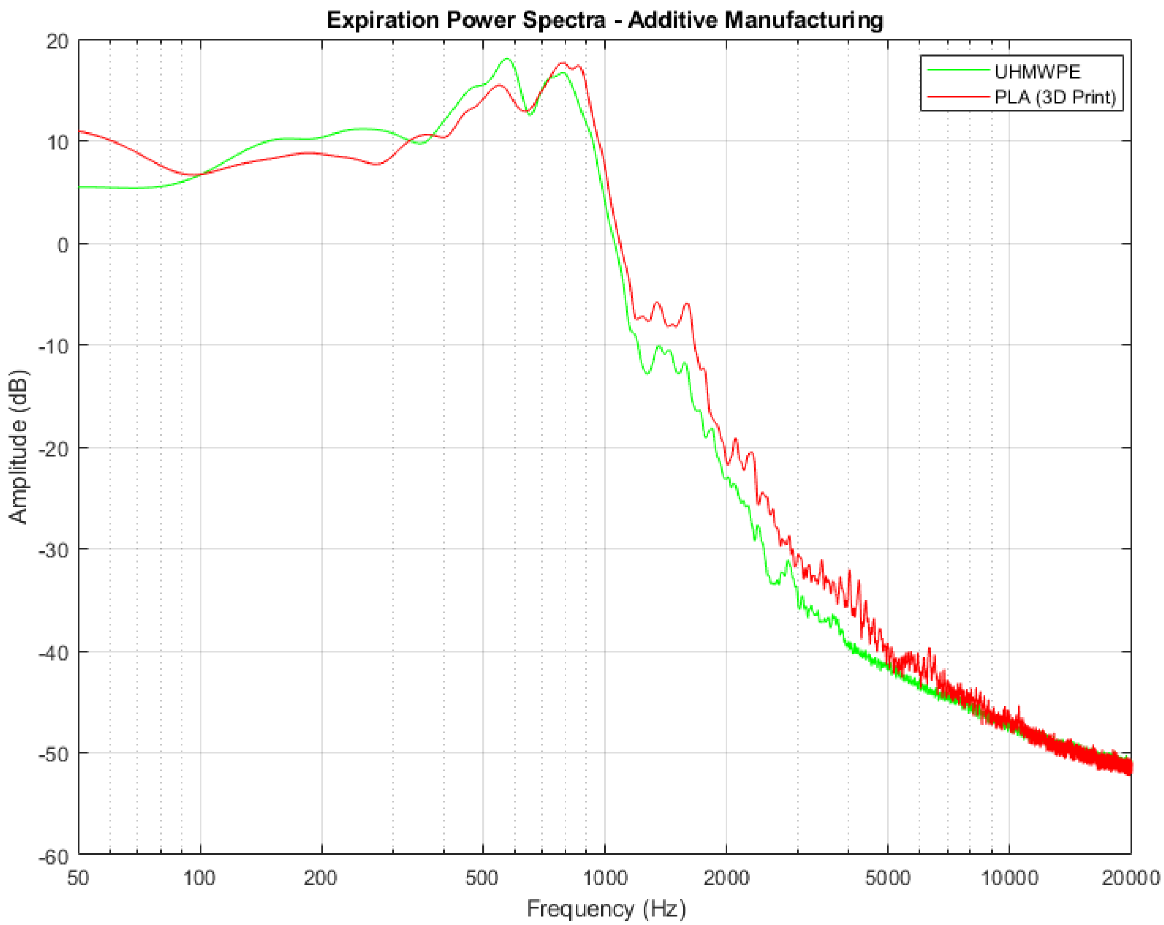

Figure 5.12. Microphone Air-Chamber response captured during expiration showing the comparison of the UHMWPE material vs. the PLA material.

During the expiratory phase (Fig. 5.12) prior to 100 Hz, the Microphone Coupler manufactured of PLA material provides the more optimal response. Between 100 - 330 Hz, the Microphone Coupler manufactured of UHMWPE material then shows the higher signal power. Following from 330 Hz, between 330 – 380 Hz, the response of the PLA material is slightly better, but then past 380 Hz and until 650 Hz the UHMWPE design provides the optimal response. From 650 Hz, the response of the two designs converges from approximately 650 – 730 Hz. Following from 730 Hz and through until 7000 Hz, the response of the Microphone Coupler manufactured of PLA material clearly shows a more optimal response with 3 – 5 dB higher signal power observed. Past 7000 Hz, the response of the two designs remains very similar for the remainder of the frequency spectrum, until 20,000 Hz.

Similar to as noted during the inspiratory phase, the response of the Microphone Coupler fabricated from PLA material shows the optimal response with higher signal power for much of the frequency spectrum, specifically for the range of 730 – 7000 Hz. Once again, the spectral peaks near to 5 kHz that were previously damped and indiscernible using the rubber isolator ring are once again discernible with the use of the harder PLA material and can be observed at 5600 Hz and 6300 Hz, respectively.

5.5. Discussion

The results suggest that the dimensions for the ideal Air-Chamber ultimately depends on the frequency bandwidth of interest since there is no single Air-Chamber design that is optimal for all frequencies. With that said however, the smaller diameter aperture chamber designs would be the most versatile for a full-spectrum (10 – 20,000 Hz) recording, with the caveat that larger diameter chambers perform slightly better at both the low and high ends of the 10 – 20,000 Hz frequency spectrum. These results are congruent with previous studies [25] [26], where the phenomena has been explained by two factors that are both desired to be optimal: 1) a minimal-volume air cavity is desired to have an increased air pressure which results in increased sensitivity at the microphone, and 2) a maximal aperture diameter at the surface of the skin is desired to capture the maximal amount of vibration at the skin surface resulting in higher signal power.

Following from the investigation of the optimal Air-Chamber dimensions, this report also describes the investigation and results of additional Microphone Coupler design characteristics including the use of a rubber isolator and the effects of material hardness. It is to the best of our knowledge that these design characteristics have not been investigated regarding the application of capturing of respiratory sounds previously, while these characteristics certainly play a role in capturing the optimal signal as demonstrated.

One additional topic of consideration regarding the design of the Air-Chamber dimensions is the effect of resonance. Specifically, with the setup consisting of the microphone placed at the base of the Air-Chamber, the effect of Helmholtz resonance must be considered. The effect of Helmholtz resonance describes a phenomenon that occurs when a container of a gas (typically air) with a single opening port experiences resonance; specifically, the air at the inlet port begins to vibrate due to the compression and then expansion of air inside the container. In our situation, the internal cavity within the microphone and before the diaphragm is the container and the Air-Chamber is the inlet port to the container. Hence, at the Helmholtz resonance, the air within the Air-Chamber would being to vibrate which in turn would vibrate the diaphragm of the microphone and produce a corresponding signal. Such a signal would not be originating from breathing sounds and should thus be avoided.

By calculation of the speed of sound in air, the cross-sectional area of the inlet port, length of the inlet port, and volume of the container, the frequency of resonance can be calculated as described by Eq. 4 below:

$$\text{Helmholtz Resonance Frequency } f = \frac{C}{2\pi}\sqrt{\frac{S}{VL}} \qquad \text{(Eq. 4)}$$

where f (in Hz) is the frequency of resonance, C is the speed of sound (in air), S is the surface-area of the inlet port, V is the volume of the container and L corresponds to the length of the inlet port.

For the chamber designs and dimensions described by this report, the Helmholtz frequency was calculated to be in excess of 20,000 Hz for each of the designs and as such, Helmholtz resonance does not play a role in generation of the relative peaks and troughs of the respective spectra for the evaluation of the Microphone Coupler and Air-Chamber designs.

In conclusion, the investigation presented takes the first steps into exploring the above-mentioned characteristics but is by no means an exhaustive analysis. Thus, we suggest that future studies venture further into various design characteristics other than the basic dimensions of the Microphone Coupler and Air-Chamber that may help further reveal intricate details contained within the full spectrum of sounds recorded. Particularly, individuals with a strong background in audio engineering would be an excellent candidate to aid in the design of a further improved Microphone Coupler with Air-Chamber.

Chapter 6

6. Battery Module

6.1. Introduction

The Battery Module is a self-contained, 1600 mAh lithium-ion polymer (Li-Po) battery attachment module that affixes to the side of the Audio Recorder and allows the device to operate completely portable, or as well, may act as an uninterrupted power supply (UPS). The Battery Module consists of two-lithium battery cells (3.7 V, 800 mAh) connected in parallel, a dedicated battery charging circuit, boost-converter circuit, and logic-level converter for the low-battery indication that signals the Audio Recorder to automatically shut-down when the battery cells are fully depleted. Additionally, the Battery Module contains a host of safety and protection features ensuring the battery does not pose a significant risk while in near proximity to the user.

Figure 6.1. Audio Recorder with Battery Module shown attached.

6.2. Design Specifications

Desired design specifications for the Battery Module and its usage are summarized in Table 6.2-1. below:

Table 6.2-1. Battery Module Design Specifications

Feature:	**Value or Range:**	**Explanation:**
Output Voltage	4.75 – 5.25 V DC	The voltage that must be supplied by the Battery Module to power the Audio Recorder.
Run-Time	≥ 6 Hours	The duration that the Battery Module can independently power the Audio Recorder.
Safety Considerations	Can be left unattended safely	The desired level of hazardous avoidance when using the Battery Module.
Physical Size	Minimal	The physical size of the battery module in comparison to the Audio Recorder.

In principle, the Battery Module must provide the correct power for the Audio Recorder to operate. The Audio Recorder is powered from DC voltage with amplitude between 4.75 V and 5.25 V; hence, the battery would need to provide such for the duration of use. Secondly, the Battery Module should be of reasonable capacity to meet the intended function of the device. Since the ASAD-III device may be used in overnight sleep studies, the battery should be able to provide power to the device for at least 6 hours (a night's sleep) before needing to be recharged. While maintaining this goal for battery capacity, the physical size of the battery should be minimal and not add considerable weight or size to the Audio Recorder device. Lastly, as the primary intended purpose of the devices involves microphones from the Audio Recorder attached to a human person, the Audio Recorder and hence Battery Module should be placed near the person; thus, safety considerations for the battery are considered of utmost importance. The goal for battery safety is to ensure that the battery could be left unattended while in use or being charged with only minimal risk for a hazardous situation.

6.3. Design

6.3.1. Battery

Battery selection was directly influenced by the design specifications outlining the ability to power the Audio Recorder, while also maintaining a minimal overall size. The initial step in the Battery Module design was to measure the current consumed by the Audio Recorder during full device operation. An ammeter was placed in series with the input to the Audio Recorder while supplying power from a 5 V DC voltage source. Both microphones, along with the micro-USB storage device were attached to the Audio Recorder and the device was set to record audio while the current consumption was measured. It was noted that the current consumption continually fluctuated and as such the current was measured 6 times over the course of 1 minute (at 10 second intervals). The current consumption readings are presented in Table 6.3.1-1 on the following page and the average of the 6 readings calculated to be 188 mA.

Table 6.3.1-1. Audio Recorder Current Consumption Measurements

Time (seconds)	**Current Measurement (mA)**
10	186
20	193
30	185
40	187
50	184
60	196
Average Current Demand:	**188 mA**

Batteries are rated in capacity in terms of milliampere-hours (mAh), thus the required battery capacity to achieve the desired specification is calculated by multiplying the average current consumption by the desired number of run-time hours:

$$(188\ mA)(6\ hours) = 1128\ mAh$$

Battery chemistries/technologies were examined including Nickel Metal Hydride (Ni-MH), Nickel Cadmium (Ni-Cd), Alkaline, etc., however their overall size to meet the demand of 6 hours run time often exceeded the physical size of the entire Audio Recorder and were out of line with the desire to maintain a small physical size. Lithium-ion polymer (Li-Po) batteries were examined and found to meet the capacity goal while also remaining minimal in size. A single lithium-ion polymer cell that met both the physical size and capacity specifications could not be readily found and as such, it was decided to connect two, smaller but identical Li-Po battery cells (Manufacturer: Tattu, Product Number: B01N74TTW6, Voltage: 3.7 V, Capacity 800 mAh) in parallel to create an overall Li-Po battery with the capacity and physical size specifications desired.

When connecting the two Li-Po battery cells in parallel, it was critically important to ensure that the voltage level of each cell was as closely matched as possibly to avoid a large current flow (from one cell to the other) when the parallel connection is made. A multi-meter was used to firstly confirm the voltage of each cell was indeed 3.80 V, after which the original connectors for the two leads from each cell, respectively, were removed. After which, the parallel connection was made whereby the positive lead from each battery were connected, and then the negative lead from each battery were also connected.

6.3.2. PowerBoost Board

The PowerBoost Board (Manufacturer: Adafruit, Product Number: 2465) is a DC-DC power converter that, as the title implies, steps-up (boosts) voltage from the supply source (the battery) to the load (the Audio Recorder). At the heart of the PowerBoost Board is a boost converter (Manufacturer: Texas Instruments, Product Number: TPS61090). The requirement for the boost converter was necessitated by the difference in the acceptable input voltage range for the Raspberry Pi (between 4.75 V and 5.25 V) and the safe working voltage range of the lithium-ion polymer battery (between 4.20 V and 3.20 V). The boost converter effectively acts to provide a steady, fixed 5.20 V output for the full input (battery) voltage range between 4.20 V and 3.20 V. The step-

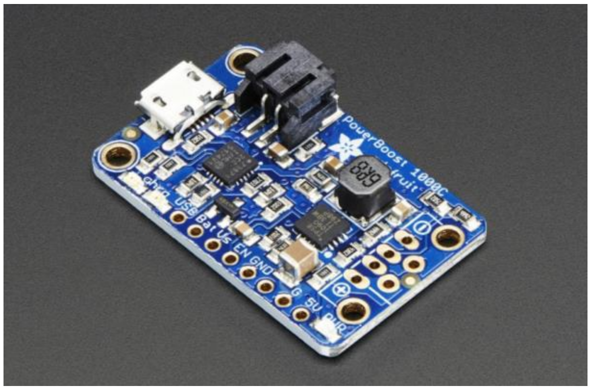

Figure 6.2. Adafruit PowerBoost 1000C circuit. Source: [47].

up (boost) process is achieved with excellent efficiency (90% +) and high-frequency operation (700 kHz).

In addition to the boost converter, the PowerBoost Board also employs an on-board, full-featured lithium-ion polymer battery charge management controller (Manufacturer: Microchip, Product Number: MCP73871) as part of the package. The MCP73871 utilizes a constant-current/constant-voltage charge algorithm with the advanced features including selectable preconditioning and charge termination points that act to greatly improve the efficiency and safety of the charging process. Moreover, the charging and boost conversion functions were designed to function in conjunction and hence the PowerBoost Board can facilitate charging of the battery while permitting the boost conversion simultaneously.

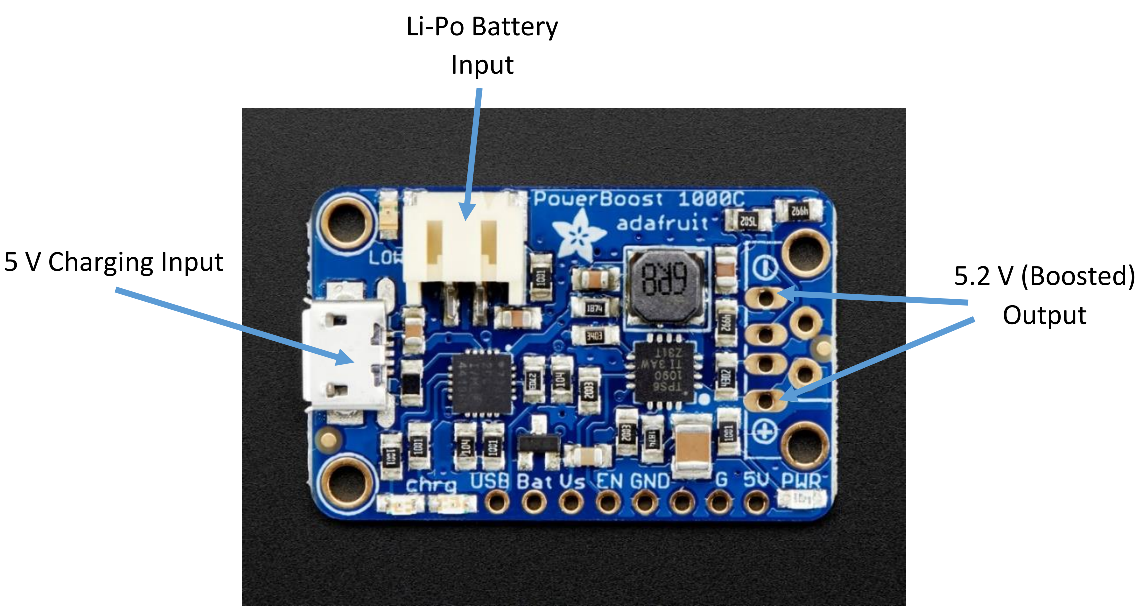

Figure 6.3. Adafruit PowerBoost 1000C circuit with main components illustrated.
Source: Adapted from [47].

By design of the PowerBoost Board, the output of the boost converter can be completely unlatched by connecting the on-board enable pin to ground. Conversely, there is no equivalent on-board configuration to unlatch the battery from the input to the PowerBoost Board, and hence the PowerBoost Board is powered on by the battery if the battery is connected. Since the design of the Battery Module intended for the battery to remain inside the enclosure without removal, a single-pole, single-throw (on/off) rocker switch (Manufacturer: ZF Electronics, Product Number: PRK22J5DBBNN) was placed between the positive terminal of the battery, and the positive input terminal of the PowerBoost Board. The switch acts to latch and unlatch the battery from the input of the PowerBoost Board, hence conserving the charge within the battery when the Battery Module is not in use.

6.3.3. Output Connector

The Battery Module utilizes a male, micro-USB connector (Manufacturer: Adafruit Industries LLC, Product Number: 1826), to connect and provide power, ground, and a low-battery signal to the Audio Recorder. The choice of style of connector was required as such due to the input connector on the Audio Recorder is a female micro-USB connector as part of the OnOff SHIM.

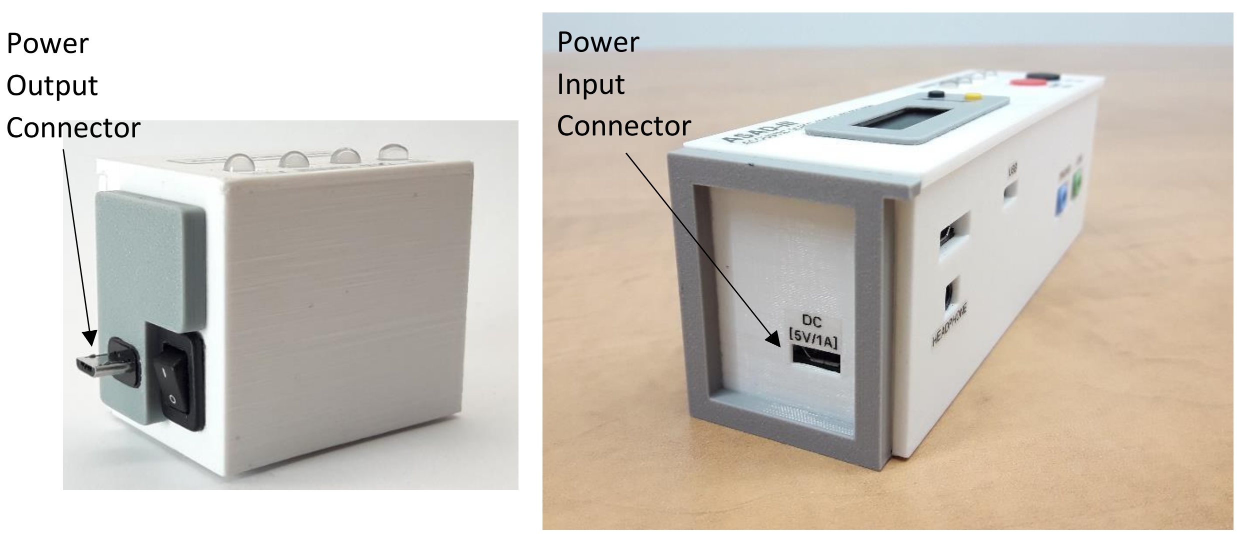

Figure 6.4. Power output connector on Battery Module (left) and Power input connector on Audio Recorder (right).

A micro-USB connector, by design, has five terminals, illustrated within Fig. 6.5:

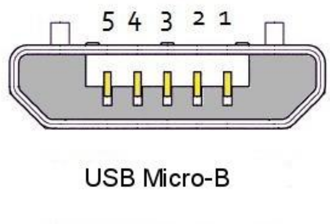

Figure 6.5. Micro-USB connector with pins labelled. Source: [52].

Table 6.3.3-1. Micro-USB Pin Configuration

Pin	Description
1	Power
2	Data (-)
3	Data (+)
4	N/C
5	Ground

Standard convention for the micro-USB pin polarity was adhered to both for the Battery Module design and for the OnOff SHIM used in the Audio Recorder. As noted above, in the normal configuration pins 1 and 5 are utilized to connect power and ground, respectively, between two devices. Also note in the normal configuration, pins 2 and 3 are utilized to transfer serial data between two devices. Additionally, in the normal configuration, pin 4 is not connected (N/C) and left unused.

For the female micro-USB connector on the OnOff SHIM, the connector has terminals for pins 1 through 5 inside the female connector, however, only pins 1 and 5 form a connection to the electronic circuit, pins 2, 3, and 4 do not form a connection to the circuit.

For the male micro-USB connector of the Battery Module, pins 2 and 3 were removed from the male USB connector since there is no requirement to send serial data between the Battery Module and the Audio Recorder. Pins 1 and 5, respectively, are used to connect the 5.2 V output and ground from the PowerBoost Board to the female micro-USB connector on the Audio Recorder. Similarly, the “Low Battery Output” (LBO) output of the PowerBoost Board is connected to pin 4 of the male micro-USB connector for signaling of low battery.

Moving back to the circuit present on the Audio Recorder, as was mentioned there was no connection from pin 4 of the female micro-USB connector to the circuit of the OnOff SHIM. To remedy this and allow for the low-battery signal to be sensed by the Audio Recorder, a small, 30-gauge wire was used to bride the gap from pin 4 of the female micro-USB connector to GPIO/BCM pin 17.

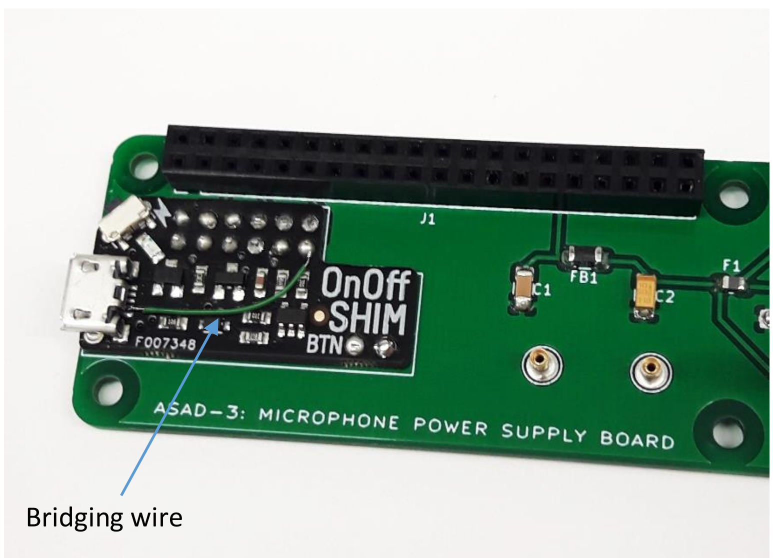

Figure 6.6. OnOff SHIM showing the (green) wire used to bridge the connection between pin 4 and GPIO/BCM pin 17.

6.3.4. Indicator Board

Although the PowerBoost Board had status indicators for the charging and boost converter circuit implemented via on-board surface mount LEDs, the desired placement of the PowerBoost Board within the enclosure for the Battery Module meant the LEDs would not be visible once the

PowerBoost Board was installed in the enclosure. It was thus decided to remove the surface mount LEDs from the PowerBoost Board, and in their place, attach wires that would extend to LEDs mounted in the top of the enclosure and hence be visible with the PowerBoost Board installed within the Battery Module enclosure.

A hot air soldering re-work gun was utilized to carefully heat the solder connection for each surface mount LED after which each LED was removed from the PowerBoost circuit board. Following this, 30-gauge wire was attached to the solder points on the PowerBoost circuit board and routed to a six-pin male connector (Manufacturer: JST Sales America Inc., Product Number: B6B-EH-A(LF)(SN)) affixed to the back side of the PowerBoost circuit board.

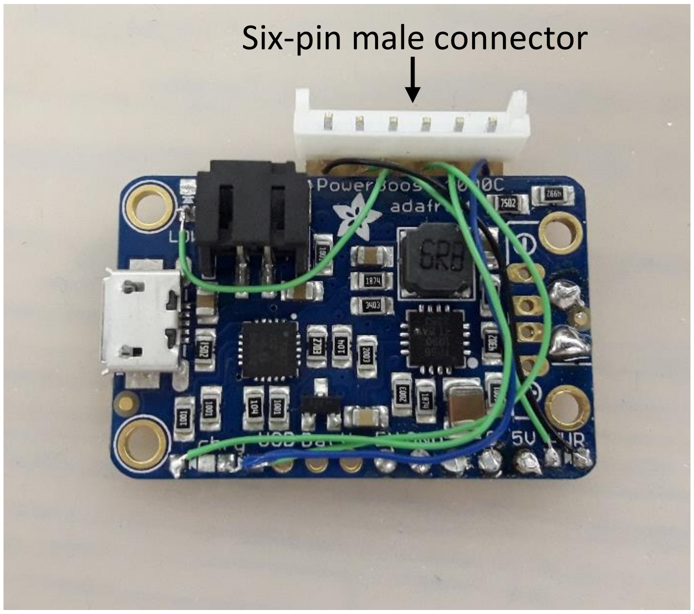

Figure 6.7. PowerBoost Board with surface-mount LEDs removed and connectivity made to six-pin male connector.

Due to the small and fragile nature of the wires attached to the solder points, the implementation of a male six-pin connector was utilized to allow the thin fragile wires to remain fixed in position, avoiding strain and possible damage, yet allow thicker, more sturdy wires (connecting via a female six-pin connector (Manufacturer: JST Sales America Inc., Product Number: EHR-6)) to be routed to the Indicator Board upon which are the LEDs which display through the top of the Battery Module enclosure.

There are 4 LED indicator lights located on Indicator Board for Battery Module status monitoring. The LEDs from the Indicator Board protrude through cut-outs in the top surface of the Battery Module enclosure, identical to implementation of the indicator LEDs on the Audio Recorder. This design was implemented to keep a consistent, user-friendly design while also providing a uniform aesthetic design making the Battery Module appear less like an attachment and more like one complete device.

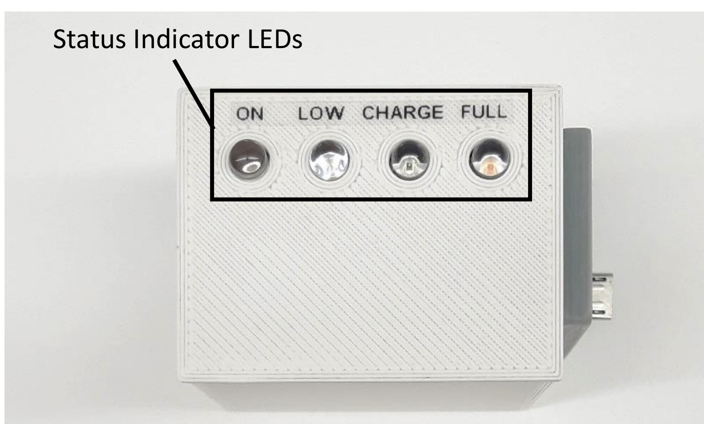

Figure 6.8. LED Indicator lights on Battery Module.

The first LED from the left, the “ON” LED is a blue-colored indicator which is illuminated when the Battery Module power switch is turned to on, letting the user know that the PowerBoost Board is powered on via the attached battery.

The second LED from the left, the “LOW” LED is a high visibility, super-bright (18,000 mcd) yellow-colored indicator which displays if the Li-Po battery cells have reached the minimum safe operating voltage. The “LOW” LED is illuminated when the battery voltage drops below 3.20V, indicating that the battery requires charging.

The third LED from the left, the “CHARGE” LED is a red-colored indicator that displays if the battery cells are currently being charged or not. The “CHARGE” LED is illuminated when a power source providing 5V to the PowerBoost charging input is supplying charge to the battery cells.

The fourth LED from the left, the “FULL” LED is a green-colored indicator which is illuminated when a power source supplying 5V to the PowerBoost charging input is connected, and the charging cycle for the attached battery is complete.

6.3.5. Safety/Protection Features

The battery design incorporates a host of various protection features that are designed to prevent damage to the battery and thus any hazardous situation if a fault or user misuse/error takes place. The battery incorporates thermal protection via a thermal fuse, overvoltage and over current protection via the battery charging circuit, and over-discharge protection whereby the Audio Recorder is automatically shut down preventing the battery from discharging any further. All potential hazardous situations are attempted to be protected against and hence the Battery Module may be left while in use, while charging, or both, unattended and with minimal risk.

6.3.5.1. Over-Voltage Protection

The scenario of battery overvoltage is applicable when the Battery Module is being charged, since once the battery is charged to full capacity, continuing to charge the battery can result in a hazardous situation. Extended charging above the maximum safe operating voltage will result in the plating of metallic lithium on the internal anode terminal of the battery. Additionally, the excessive loss of lithium ions from the cathode material permits the remaining cathode material to act as an oxidizing agent. The cathode in turn loses stability and produces gaseous carbon dioxide during the oxidation reaction. The internal pressure of the battery pack rises as a result and if the process continues (as a result of continued overcharging), the battery pack will eventually burst to vent the excess internal pressure.

Overcharging of the Battery Module was mitigated by using the PowerBoost Board, as the board not only acts as a boost converter but employs a full-featured lithium-polymer battery charge management controller (Manufacturer: Microchip, Product Number: MCP73871) as part of the package. The MCP73871 utilizes a constant-current/constant-voltage charge algorithm with the advanced features including selectable preconditioning and charge termination points. Charging of the battery is performed in three stages: firstly, a preconditioning stage that supplies low-current to bring the battery up to a predefined voltage, next a constant-current (1000 mA max), fast charge that charges the battery to near full capacity, and finally a constant-voltage trickle charge to bring the battery up to full capacity. At the end of the final charging stage, the constant-voltage trickle charge is terminated when the trickle charge current drops below 10 mA. At this point, the current is latched off the battery and the MCP73871 enters a charge complete/standby mode, whereby no additional current is supplied to the battery. Additionally, during the standby mode, the MCP73871 continually measures the voltage of the battery, if the battery voltage drops below the recharge threshold, another charging cycle is initiated.

6.3.5.2. Under-Voltage Protection

Undervoltage (over-discharge) protection is an important scenario that must be avoided with lithium-ion cells, not only to maintain recharging abilities of the battery, but also to avoid a potentially dangerous scenario to the user of the device. Inside the lithium-ion battery, a copper foil is used as an anode collector. When over-discharged, the copper is oxidized to copper ions, resulting in a degradation of the copper foil anode and a degradation in the efficiency of the battery as a whole [27]. Additionally, over-discharging can lead to the formation of internal short circuits within the battery, increasing the risk of the battery experiencing thermal runaway: a feedback reaction in which the internal temperature of the battery rises rapidly resulting in the sudden release of energy stored by the battery.

Undervoltage protection needed to be addressed in an intelligent fashion, first and foremost since it could potentially pose a risk for the user, but secondly, since at the point when the battery is considered fully discharged (the minimum safe operating voltage without being over-discharged) the power supplied to the Audio Recorder could not simply be abruptly halted. An abrupt halt to the power supplied to the Audio Recorder could result in a corrupted audio file (if recording were taking place) or worse, the corruption of the OS on the SD card due to the abrupt loss of power.

The optimal solution to prevent over-discharge of the battery and to avoid corruption of the audio file or OS would be to turn the Audio Recorder off and discontinue use when the battery reached the minimum safe operating voltage. Instead of relying on the user to closely monitor the state of the battery, an automated solution was implemented where upon detecting the battery reaching the minimum safe operating voltage, the Audio Recorder automatically executes a shut-down command on the Raspberry Pi. The shut-down command firstly stops the audio recording and closes the audio file, then completely shuts down the hardware and OS of the Raspberry Pi, in turn, preventing further discharge of the battery.

The above task was implemented utilizing the LBO of the PowerBoost Board. As mentioned in the application information for the PowerBoost Board, the LBO pin by default, has the same voltage as the battery when the battery is not fully discharged (i.e., above 3.2 V). However, when the PowerBoost Board detects that the battery is fully discharged (below 3.2 V) the LBO pin is latched to ground, and the LBO pin is sustained at 0 V potential.

Recalling that the trigger to perform a shut down on the Audio Recorder occurs by connecting GPIO/BCM pin 17 to ground (by pressing the “ON/OFF” button); it was realized the LBO output could also be utilized in parallel to the “ON/OFF” button to trigger a shut-down on the Audio Recorder. As such, a physical connection between the LBO pin of the PowerBoost Board and GPIO/BCM pin 17 on the Audio Recorder was facilitated utilizing the micro-USB connector already being used to connect the Battery Module to the Audio Recorder for supplying power. However, in examining the maximum recommended voltages to the Raspberry Pi GPIO, it was noted the GPIO pins are CMOS 3.3 V logic pins and as such, inputs to the GPIO pins should not exceed 3.3 V as prompt damage to the Raspberry Pi would result. As the battery cells and thus the LBO output pin of the PowerBoost Board regularly operate between the range of 3.2 V and 4.2 V, a logic-level converter (Manufacturer: SparkFun Electronics, Product Number: BOB-12009) was placed between the LBO pin of the PowerBoost Board and pin 4 of the male micro-USB connector.

The logic-level converter is a common circuit configuration that is used to convert 5 V signals to 3.3 V signals and vice versa. In the implementation of the Battery Module, the logic-level converter is utilized to step-down the LBO output potential from the range 4.2 V - 3.2 V to the range of approximately 3.0 V - 2.6 V (when the battery is not low), while still retaining the ability to permit the LBO output of approximately 0 V (when the battery is low).

Therefore, when the battery is not low in charge, pin 4 (and thus GPIO/BCM pin 17) measures in the range of 3.0 V – 2.6 V; thus, it will not trigger a shut-down of the Audio Recorder. However, when the PowerBoost Board senses the battery voltage has dropped below 3.2 V, the LBO is latched to ground and as a result, pin 4 (and thus GPIO/BCM pin 17) measures 0 V and triggers the Audio Recorder to shut down; the same as pressing the "ON/OFF" button would.

6.3.5.3. Over-Current Protection

Battery over-current conditions can occur during charging or discharging where the current flowing into or out of the battery, respectively, exceeds the recommended safe operating limit. When the current exceeds the operating limit, the cell temperature of the battery may begin to rise, which if left to continue, can result in a hazardous situation. Over-current protection during both charging and discharging is managed by the MCP73871 IC on the PowerBoost Board which employs both thermal regulation and thermal shutdown to optimize the charge cycle time and maintain device safety while in use; the further details of such explained within Section 6.3.5.4 (Over-Temperature Protection) of this report.

6.3.5.4. Over-Temperature Protection

Over-temperature protection is another important scenario that must be avoided with lithium-ion cells since an increase in the cell temperature can, at minimum, damage the cells, decreasing their performance and shortening their lifespan. More concerning though is the possibility for cell temperatures to rise high enough to cause surrounding materials to combust, or worse, the cell to reach a point of thermal runaway resulting in the cell rapidly venting pressure and thus possibly fire.

Over-temperature protection was implemented dually, using two solutions to effectively mitigate the risks for the two states of the battery: either during charging, or when being discharged. The first solution implements safety measures when charging the battery and is handled by the PowerBoost Board. The MCP73871 IC on the PowerBoost Board employs both thermal regulation and thermal shutdown to optimize the charge cycle time and maintain device safety while in use.

Thermal regulation performed by the MCP73871 acts to limit the charge and discharge currents based upon the internal temperature measured by the IC. As battery cell temperature has a correlation to charge current; the temperature measured by the MCP73871 is utilized as an indirect measure of thermal load upon the battery. As the temperature measured by the IC increases, the max charging current is regulated. Upon reaching 150 °C, the MCP73871 suspends the charge cycle and automatically resumes once the measure temperature decreases by approximately 10 °C.

During battery discharge, a secondary solution utilizing a thermal fuse was implemented to ensure the battery temperature does not increase past a safe operating temperature. The thermal fuse (Manufacturer: Cantherm, Product Number: SDF DF072S, Holding Temperature: 50 °C, Trip

Temperature: 72 °C) is a two-terminal device (input and output) and was placed in series with the positive lead wire of the battery cells. The fuse was mounted such that the case of the fuse is in direct contact with the lithium polymer cells inside the device enclosure; and hence maintains the same temperature of the battery cells while discharging. Upon the temperature of the fuse reaching 72 °C, the internal connection within the fuse (bridging the input to the output) is disconnected, breaking the positive lead terminal connection of the battery to the PowerBoost Board and hence preventing the battery from reaching a point of thermal runaway.

6.3.6. Enclosure

The enclosure for the Battery Module was designed to match closely that of the Audio Recorder, both in dimensions, and in physical appearance. The overall height and depth of the Battery Module enclosure are identical to the Audio Recorder enclosure, 42 mm and 37 mm respectively; whereas the width of the Battery Module measures 48 mm (compared to 123 mm for the Audio Recorder). The width of the Battery Module was optimized at 48 mm to accommodate the physical space required by two combined lithium-ion polymer battery cells: the combined cells measuring 45 mm wide, 25 mm in height, and 20 mm in depth.

Similar to the process used to design the enclosure for the Audio Recorder, precise dimensions of the overall hardware, including the two battery cells, the PowerBoost Board, and all provisions for the four status LEDs, power switch, and input/output micro-USB connectors were imported into a 3D modeling suite. An overall enclosed, original design was generated with considerations made to ensure component placement would be secure and relatively easy to access in the event of required service.

Similar to the Audio Recorder, a means of accessing the interior of the enclosure was again needed to be able to insert the electronic hardware and to permit access to the hardware if servicing were to be required. Identical to the Audio Recorder, the enclosure for the Battery Module is split into 2 components: one component forms the 2 side walls, back wall, and top of the enclosure; the second component forms the front wall and bottom of the enclosure. The two components of the Battery Module enclosure come together via the secondary component of the enclosure (front and bottom) being inserted into the primary component, from front to back in a snug friction-fit with a "latch" segment integrated into the primary component that holds the secondary component securely in place when fully inserted.

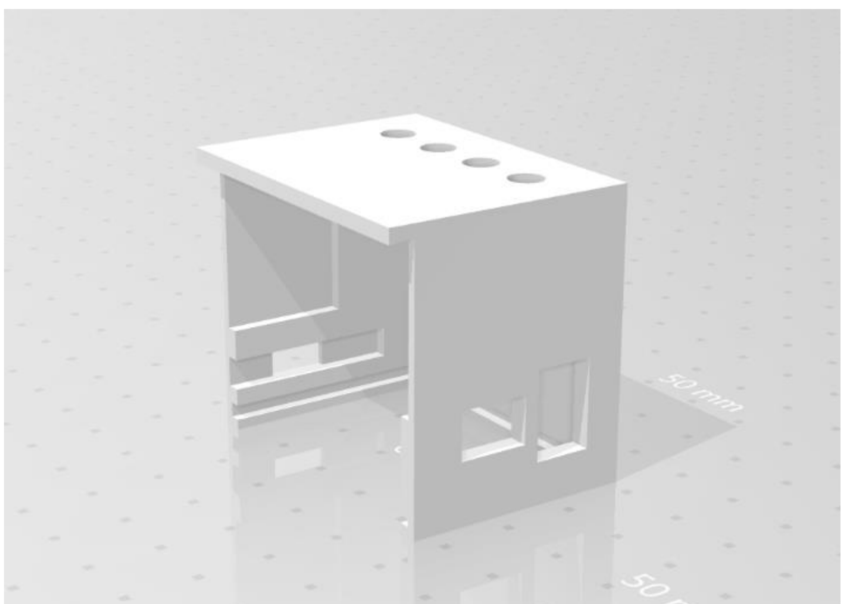

Figure 6.9. Enclosure model with primary component shown, including the two side walls, back-side wall, and top.

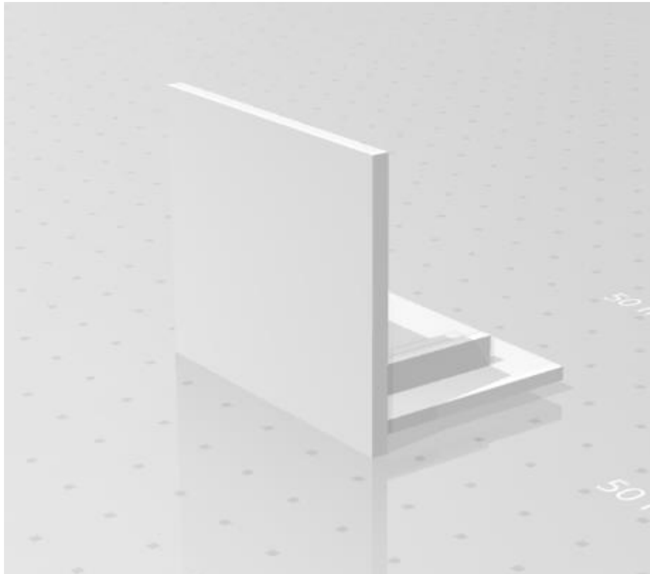

Figure 6.10. Enclosure model with secondary component shown, including the front-side wall and bottom.

Similar as well to the design of the enclosure for the Audio Recorder, provisions inside the Battery Module enclosure were integrated to allow for the support of several components, such as to support the battery cells and output connector.

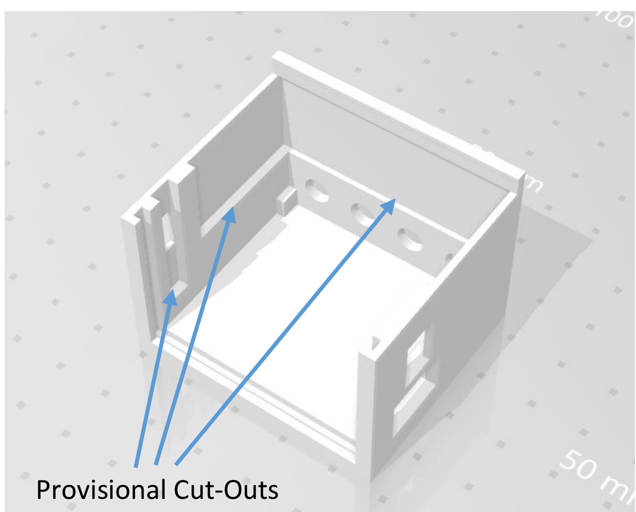

Figure 6.11. Primary component of Battery Module enclosure illustrating internal provisional cut-outs.

Additionally, special attention had to be paid to the support required for the PowerBoost Board since the board would need to be braced to handle repeated stresses of attaching a micro-USB connector for charging. A barrier was designed into the secondary component of the Battery Module enclosure to provide support to the circuit while a micro-USB plug is inserted.

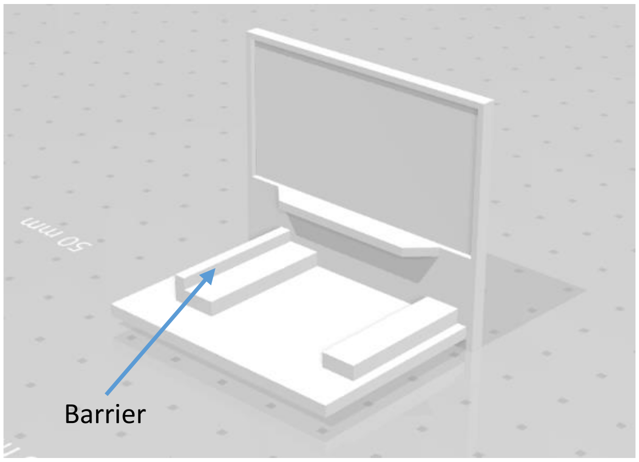

Figure 6.12. Secondary component of Battery Module enclosure illustrating the barrier to provide support while force is applied to insert micro-USB plug.

Equally as important was the task of placing a power switch for the Battery Module that would be easy to use; yet would not allow the user to mistakenly turn-off the Battery Module before the Audio Recorder was properly shut down (especially important to ensure corruption of the audio file or the OS does not occur). Of the six sides upon which the power switch could be installed, the side that would be in contact with the Audio Recorder was chosen as the switch would thus be inaccessible when the Battery Module was attached to the Audio Recorder. This placement of the switch permits the user to easily turn on the Battery Module before attaching it to the Audio Recorder yet prevents the switch from being accidently tripped when the Battery Module is connected to and powering the Audio Recorder.

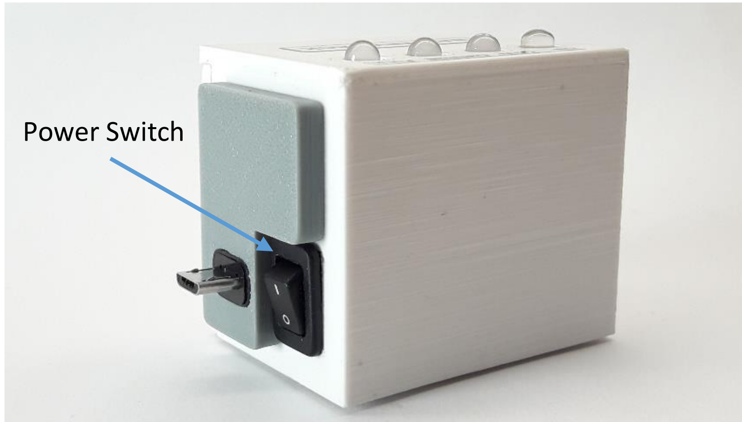

Figure 6.13. Power switch installed in Battery Module enclosure.

The final design aspect of the Battery Module enclosure entailed developing a means of securely providing a mechanism for affixing the Battery Module to the Audio Recorder that would also permit to module to be removed when desired. Compounding the challenge was the choice of the location for the switch and the necessity to avoid contact of the switch while the Battery Module is attached to the Audio Recorder. A simple solution, consisting of a friction, press-fit between a protruding piece (on the Battery Module) and a recessed piece (on the Audio Recorder) was designed in the 3D modeling suite and then printed in the same PLA material as used for the enclosures of the Audio Recorder and Battery Module. A tolerance of 0.20 mm between the mating parts was designed to ensure that the connection method would be removable yet provide a secure friction fit.

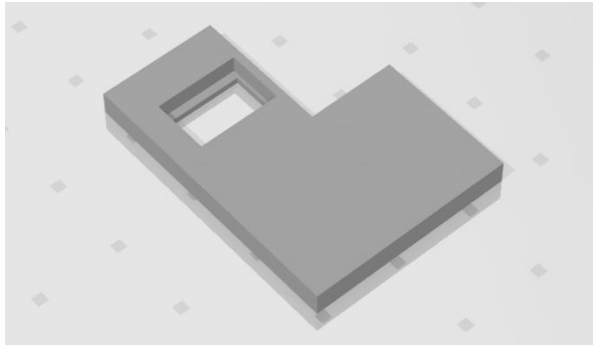

Figure 6.14. Protruding piece to be installed on Battery Module for attachment to Audio

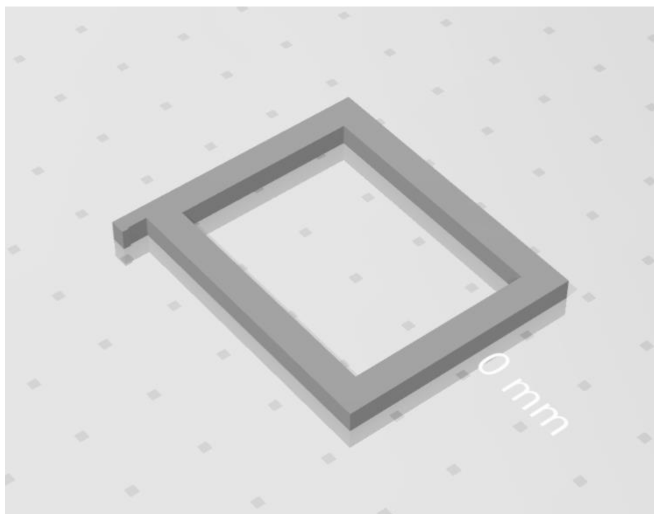

Figure 6.15. Recessed piece to be installed on Audio Recorder for attachment to Battery Module.

After the printing the attachment pieces, both the protruding piece and the recessed piece were adhered to the enclosure for the Battery Module and the Audio Recorder, respectively. Contact cement (Manufacturer: LePage, Product Name: Heavy Duty Contact Cement, 30 mL) was utilized to bond the attachment pieces to each respective enclosure and ensure a secure, permanent bond.

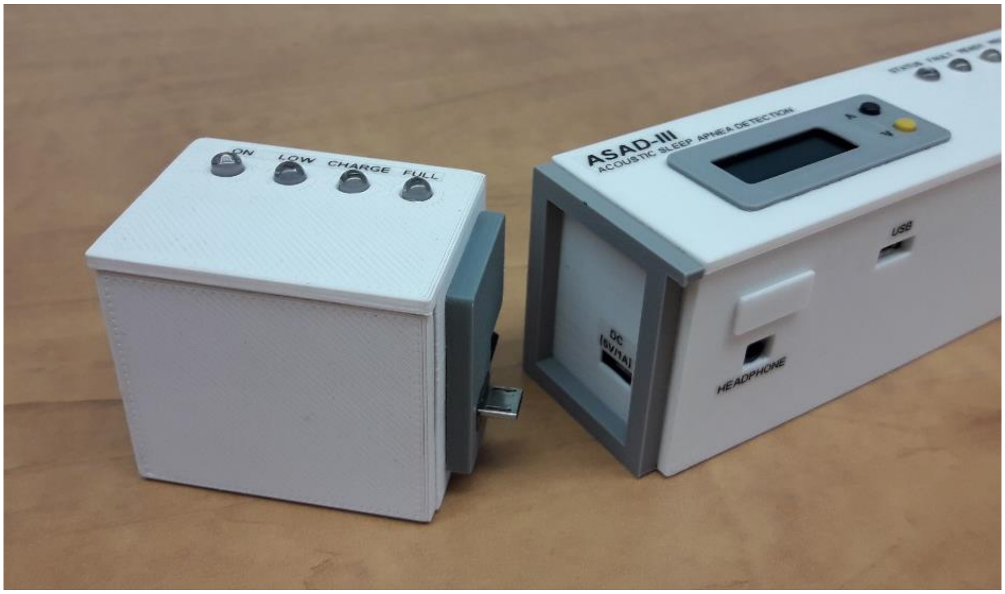

Figure 6.16. Battery Module (left) and Audio Recorder (right) with protruding and recessed pieces installed.

Figure 6.17. Battery Module shown attached to the Audio Recorder.

6.4. Evaluation

6.4.1. Battery Performance

Battery performance was firstly evaluated for the run-time duration from the Battery Module to investigate if the specification was met. The Battery Module was firstly charged to full capacity and then attached to the Audio Recorder. Both microphones were attached to the Audio Recorder and the recorder was set on record. Battery voltage measurements were taken every 30 minutes until the Battery Module was fully depleted.

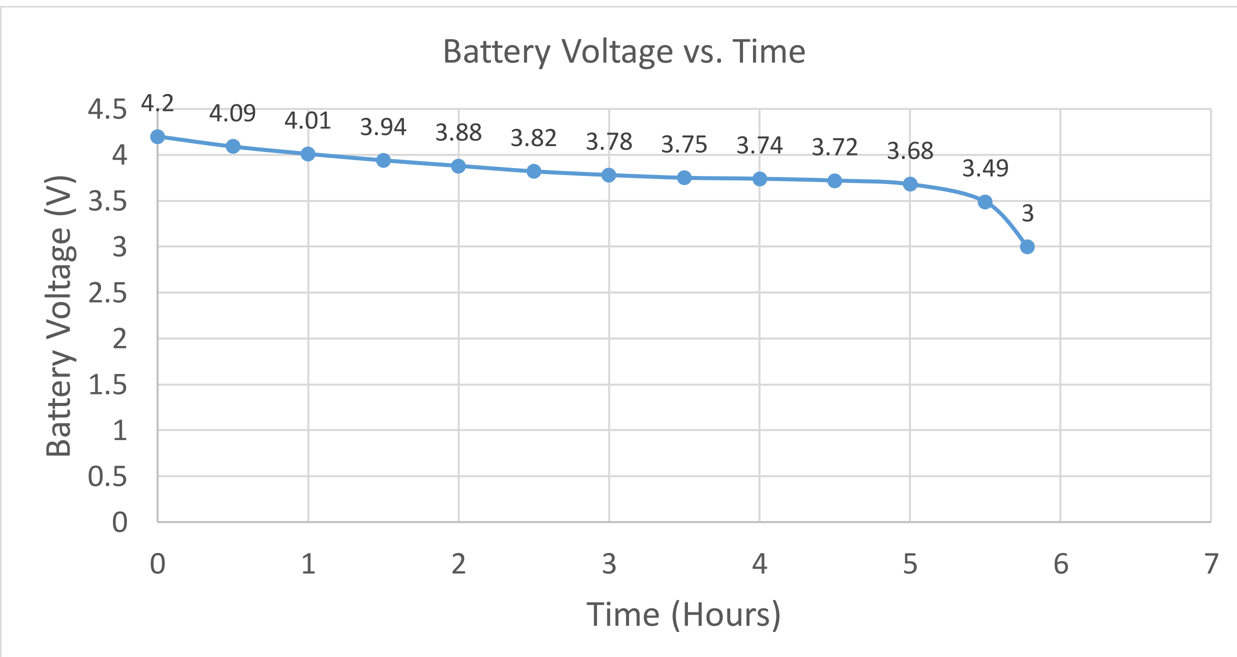

Figure 6.18. Results of Battery Module run-time test.

As can be noted by Fig. 6.18, the results initially looked promising, however the goal of 6-hours was not achieved. Unfortunately, the battery was determined fully depleted at approximately 5 hours, 45 minutes after the test began; ~96% of the desired goal. By rough estimation of the average current draw by the Audio Recorder from the measurements conducted during the design phase of the Battery Module, the capacity of individual battery cells can be calculated to be closer to approximately 540 mAH instead of the advertised 800 mAH. As a result of this finding, another 48 mAH of battery capacity would be required to meet the 6-hour run-time goal.

6.4.2. Leakage Current

Leakage current is an electric current that flows from an electronic device to ground; or in the case of devices that have a floating ground, it is the current that can flow to the ground through a user touching the device. In both scenarios and for the possible condition of a broken ground, this current has to be below 10 µA for the devices that are connected to a person externally. The Battery Module in conjunction with the Audio Recorder were evaluated for safety in terms of leakage current. The tests for measurement of leakage current are important to ensure that the device being tested will not result in electric shock to the user. As a proposed Medical Device, the ASAD-III device must meet the performance standards for leakage current that have been outlined within the International Standard IEC 60601-1. The prescribed tests outlined within IEC 60601-1 are intended to simulate the human body coming in contact with the different components of the electronic equipment, especially the device leads.

IEC 60601-1 provides the requirements for safety and performance of medical electrical equipment. The ASAD-III device is categorized as “BF-type Equipment” which is described as equipment where the leads intended to be applied to a patient’s skin have floating-ground input circuits, whereby there is no connection between the patient leads and Earth ground.

Due to the versatile design of the ASAD-III, the measurements for leakage current were conducted in the various operation modes and with the various power supply source modes. Specifically, leakage current measurements were conducted while powering the Audio Recorder by the three possible power sources: the direct supply of power by an AC power adapter, the supply of power from the Battery Module (while it was not being simultaneously charged), and the supply of power from the Battery Module (while it was being simultaneously charged from an AC power adapter). Additionally, in each of the power supply source modes, leakage current was evaluated in the two device modes: during standby mode where the USB drive is not connected and the device is not recording, and also during recording mode where the USB drive is connected and the device was recording auditory information. In both standby and recording mode, both microphones were connected to the Audio Recorder. A multimeter (Manufacturer: AstroAI, Model: DM6000AR) was set to measure current in µA DC mode to perform measurement for the leakage current.

6.4.2.1. Enclosure Leakage Current

The enclosure leakage current is defined as the current that can flow from the device enclosure, through the user, and to Earth ground, such as when touching the case or buttons to operate the device. For this test, a piece of aluminum foil 20mm x 20mm in size was placed on the enclosure of the Audio Recorder to simulate the surface area of a human finger touching the enclosure of the device. The multimeter was used to measure the leakage current from the aluminum foil placed on the enclosure to the Earth ground connection of an AC outlet. The measurement was recorded and shown as location "Case" as presented in Table 6.4-1. In addition, a second measurement was conducted from the USB drive connected to the Audio Recorder. Although not technically part of the enclosure, the USB drive is required to be inserted into the Audio Recorder for recording to take place and hence is always present during the recording mode. Once inserted into the Audio Recorder, there is an exposed metal part of the USB drive that can contact the user. The multimeter was used to measure the leakage current from the exposed metal of the USB drive to the Earth ground connection of an AC outlet. The measurement was recorded and shown as location "USB" as presented in Table 6.4-1. The limit for the enclosure leakage current as IEC 60601-1 is stated as 10 µA DC in both standby and recording mode.

Table 6.4-1. Enclosure Leakage Current

Power Source:	**Mode:**	**Location:**	**Measured Leakage Current:**	**Threshold Leakage Current:**
AC Power Adapter	Standby Mode	Case	0.0 µA	10 µA
	Recording Mode	Case	0.0 µA	10 µA
		USB	0.2 µA	10 µA
Battery (Not Charging)	Standby Mode	Case	0.0 µA	10 µA
	Recording Mode	Case	0.0 µA	10 µA
		USB	0.0 µA	10 µA
Battery (While Charging)	Standby Mode	Case	0.0 µA	10 µA
	Recording Mode	Case	0.0 µA	10 µA
		USB	0.5 µA	10 µA

6.4.2.2. Patient Leakage Current

The patient leakage current is defined as the current that can flow from the leads of the device (i.e., the microphones), through the patient, and to Earth ground, such as when the microphone is connected on the surface of the skin and the device is powered on. For this test, the multimeter was used to measure the leakage current from the metal capsule of the microphone to the Earth ground connection of an AC outlet. The measurement was recorded and is shown as location "Mic Capsule" as presented in Table 6.4-2. The limit for the patient leakage current as IEC 60601-1 is stated as 10 µA DC in both standby and recording mode.

Table 6.4-2. Patient Leakage Current

Power Source:	**Mode:**	**Location:**	**Measured Leakage Current:**	**Threshold Leakage Current:**
AC Power Adapter	Standby Mode	Mic Capsule	0.1 µA	10 µA
	Recording Mode	Mic Capsule	0.2 µA	10 µA
Battery (Not Charging)	Standby Mode	Mic Capsule	0.0 µA	10 µA
	Recording Mode	Mic Capsule	0.0 µA	10 µA
Battery (While Charging)	Standby Mode	Mic Capsule	0.1 µA	10 µA
	Recording Mode	Mic Capsule	0.1 µA	10 µA

6.4.2.3. Patient Auxiliary Leakage Current

The patient auxiliary leakage current is defined as the current that can flow between the multiple leads of the device (i.e., the microphones), through the patient from one microphone to the other, such as when the leads are connected on the surface of the skin and the device is powered on. For this test, the multimeter was used to measure the leakage current from the metal capsule of one microphone to the metal capsule of second microphone. The measurement was recorded and is shown as location "Mic Capsule" as presented in Table 6.4-3. The limit for the patient leakage current as IEC 60601-1 is stated as 10 µA DC in both standby and recording mode.

Table 6.4-3. Patient Auxiliary Leakage Current

Power Source:	**Mode:**	**Location:**	**Measured Leakage Current:**	**Threshold Leakage Current:**
AC Power Adapter	Standby Mode	Mic Capsule	0.1 µA	10 µA
	Recording Mode	Mic Capsule	2.0 µA	10 µA
Battery (Not Charging)	Standby Mode	Mic Capsule	0.1 µA	10 µA
	Recording Mode	Mic Capsule	3.3 µA	10 µA
Battery (While Charging)	Standby Mode	Mic Capsule	0.1 µA	10 µA
	Recording Mode	Mic Capsule	2.4 µA	10 µA

6.5. Discussion

With the results presented above, the battery module is a fully functional unit with the only shortfall being a lesser run-time than designed for. This issue could be remedied by simply adding an additional battery cell to the battery module. Adding a third 540 mAH battery cell (advertised as 800 mAH) in parallel with the existing two cells would satisfy the run-time requirement. However, in adding an additional cell, the overall size of the battery module would have to be expanded and redesigned to fit the additional cell; such a task is suggested for future work.

Alternatively, the versatile design of the ASAD-III system allows for two other techniques to meet the desired run-time requirement. Firstly, if it is known that the device will be required to record longer than permitted by the 5 hours, 45 minutes provided by the Battery Module, the Battery Module may be left removed and the Audio Recorder may be supplied directly by a 5 V, 1 Amp micro-USB AC adapter power supply for the duration of the recording. The Audio Recorder will operate continuously for the duration the device is supplied power by the wall-adapter with no need to worry about battery depletion.

Secondly, the Battery Module allows for simultaneous charging while suppling power to the Audio Recorder. It the Battery Module is initially used to power the Audio Recorder and the Battery Module nears depletion, but the recording is desired to continue without interruption, the Battery Module may be supplied by a 5 V, 1 Amp micro-USB AC adapter power supply for simultaneous charging of the battery cells while providing power to the Audio Recorder.

Finally, in all the various modes for power supply of the ASAD-III device, the ASAD-III device was evaluated for leakage current with respect to the International Standard IEC 60601-1. In each of the various modes for power supply, and additionally, during each device operation mode, the leakage current measured from the ASAD-III device met the requirements with a lower measured leakage current than the threshold requirement. Thus, with the implemented and numerous battery safety circuits, along with the leakage current measurements within safety thresholds, the user of the ASAD-III may rest assured the device remains safe to apply on the surface of the skin without electric shock and safe to perform its intended use.

Chapter 7

7. Concluding Remarks

7.1. Project Objectives

This thesis takes the first steps towards creating a device that can be used to quickly and accurately assess for OSA by implementing a fully functional prototype audio recording device, the ASAD-III (Acoustic Sleep Apnea Detection, Version 3). ASAD-III is intended to be used for recording breathing sounds over the trachea and lungs during either wakefulness or sleep. The main purpose of the prototype was to offer a proof-of-concept device capable of recording respiratory sounds to be used in conjunction with the AWakeOSA analysis technology developed by our research group. The combined efforts of the work presented by the thesis as well as the previous work on auditory estimation techniques by our research group thus comprise and hence demonstrate a rapid screening tool to assess for moderate and severe cases of OSA as an alternative to the traditional PSG study. The secondary objective was to have the device be a cost-effective, small, and light-weight unit that would be safe to be used by users even in their own home.

As presented within this report, the ASAD-III device achieves the primary goal by simultaneously recording both tracheal and lung respiratory sounds in high-quality by digital representation of the sounds with high resolution (16-bits) and high-frequency sampling rate (44,100 Hz). Following, the audio information is stored in the Microsoft WAV audio file-format, which is uncompressed and thus retains every detail of auditory information as it was originally recorded. As well, peripheral components, including the choice of Microphone and the choice of Air-Chamber geometry were optimized to achieve the best possible quality during capture of respiratory sounds. Appropriate shielding within the Audio Recorder as well as within in the Microphone cables was utilized to prevent interference as much as possible on the precious audio signals. Further to the point, all the connection points for the audio signals were chosen to be of gold material to act as the best possible conductor with ultimate corrosion resistance to ensure the connections perform excellent and reliably for years to come. With the above-mentioned features and other extensive design characteristics described by this report, the respiratory sounds recorded are not only compatible with the AWakeOSA algorithm, but also provide the algorithm with exceptionally excellent-quality auditory information.

As for the secondary design objectives, cost-effectiveness was stringently adhered to whilst also meeting maintaining to meet the primary objective. In the end, the overall cost of the ASAD-III recording device and its various components was totaled at $357.30. The objective to achieve a portable and small form-factor for the device was also well achieved with the overall design of the ASAD-III device incorporating the objective by several aspects. Firstly, the device is fully contained and does not require any additional equipment outside the ASAD-III device hardware to capture the respiratory sounds. A clear, illuminated, and easy-to-understand display screen provides real-time feedback and is paired with a set of straight-forward push-buttons to control and completely operate the device. Secondly, the ASAD-III device is adaptable in use and construction. The device can be powered by the included battery if there is no AC supply in the area, or alternatively, the device can also function by being powered from an AC supply with the included AC adapter. The peripheral components (i.e., Microphones, USB drive, Battery Pack) are removeable from the Audio Recorder for easy and secure transport or straight-forward replacement if needed. Most notably, adding to the portable nature of the ASAD-III device, the overall size and weight of the device was designed minimal as much as possible. Overall dimensions of the ASAD-III device measure as 127.0 mm length (175.0 mm length with Battery Module attached) x 37.5 mm width x 42.0 mm tall. Overall weight for the ASAD-III device is: 0.255 kg including all peripheral components.

7.2. High-Frequency Content

The ASAD-III prototype device met the design objectives to permit its use with the AWakeOSA technology, but as well, adds the ability to offer an expanded viewpoint of the spectrum of tracheal breathing sounds. Namely, the design of ASAD-III device enables respiratory sound recording with the ability to record auditory information with frequency up to 20 kHz. Typically, many precursory auditory estimation techniques only focused on lower frequency spectral analysis, typically 5 kHz and below. Early investigations note the spectrum of tracheal sounds is within the range of approximately 100 – 3,000 Hz [12]. Previous studies often implemented a hardware low-pass filter which limited the spectrum of sounds recorded; likely attributed to the range specified within the early investigations. However, with the high-resolution and high-quality sounds recorded by the ASAD-III device, it was our goal to investigate if the frequency spectrum of tracheal sounds extends beyond 5 kHz.

An observation that is recurrent throughout the spectra as presented throughout this report, tracheal respiratory sounds do show a wider spectrum than 5 kHz, albeit low amplitude, past 5 kHz. The design of the coupler was able to help in revealing the appreciable signal content above 5 kHz. Specifically, the results presented with the use of the Revision 3 Microphone Coupler design indicate the sounds originate from the sound source and form part of the spectrum for tracheal sounds. From the tracheal sounds recorded then, during inspiration, signal content is observed up to approximately 9 kHz, and similarly during expiration, signal content is observed up to approximately 8 kHz. Additional investigation and confirmation are still necessary and is suggested as part of future work for research involving tracheal sounds and their measurement. However, recording with full-spectrum (10 – 20,000 Hz) capability is recommended, or at minimum, recording up to a frequency of at least 10,000 Hz is highly suggested to fully capture the spectrum of tracheal sounds. Tracheal sounds, albeit low amplitude, and in excess of 5 kHz which were previously ignored, may hold critical clues for OSA diagnosis or other breathing disorders.

7.3. Suggestions for Future Work

As a prototype device, naturally there are some suggestions for improvements that can be made to improve the ASAD-III device for future development which are detailed in the following sections. General suggestions relate to the ASAD-III device as a whole whereas the following subsections relate to suggestions for the individual components of the device.

7.3.1. General Suggestions

The first and most general suggestion that can be made for the ASAD-III prototype involves integration of the device components. As a prototype, the ASAD-III device was designed to be modular as much as possible to facilitate the design and testing of each module. When designing such a device with complex behaviour, it is not always known which solution of component will perform optimally, and additionally, there are some occasions when each component/module will work as expected on its own, but unexpected behaviour occurs when placing all components/modules together as a working unit. The modular design allowed for an individual module to be changed or updated and avoid the need to re-design or re-fabricate unnecessarily.

Now that the modules, and prototype as a whole, has been shown to operate as desired, for future iterations the device would certainly benefit with greater integration of the modules. In the Audio Recorder, the individual circuit boards could be combined and optimized to save space removing the need for bulky and numerous connectors. The Battery Module would also greatly benefit with integration into the Audio Recorder. The need to attach a battery for operation could result in the battery being forgotten, and additionally leaves the possibility for the battery to be accidently disconnected thus halting the recording process. In the future, a better design would integrate the battery in the Audio Recorder hence eliminating the possibility to forget or mistakenly disconnect the battery.

As well, it is anticipated that one hinderance for the end user of the ASAD-III device in its current state is the need to attach the USB Drive for the storage of recorded data, and more so, the process of analyzing the data post-recording via the support vector machine. Going forward, the best-case scenario suggestion would be to have AWakeOSA algorithm and thus analysis integrated into and running real-time on the ASAD-III device. To achieve this, significant work would be required to port the AWakeOSA algorithm to run on the Linux-based Raspberry Pi OS in an efficient and effective manner.

Going together with the integration of the AWakeOSA algorithm on the Raspberry Pi OS, the next suggestion would be the ability to control and view recording progress and real-time analysis using some type of wireless device such as a cell phone or tablet. To achieve this, a communication protocol and supporting application suitable to run on the wireless device would need to be developed and optimized to be able to transmit the data being recorded and analyzed by the ASAD-III device. Such a feature would not only make recording and analysis convenient, but also likely increase its effectiveness since noisy or otherwise poor-quality recordings could be more easily identified before proceeding with a recording procedure.

A final suggestion relating to the ASAD-III device in a general sense is to remove all unnecessary features and configurations from the Raspberry Pi OS going forward. Doing so would decrease power consumption further and dedicate resources strictly to the audio recording process. As the OS for the Audio Recorder sits currently, the default OS has been left nearly unchanged with the command-script to control the recording process simply added as an additional task. The best-case scenario suggestion would be to write a custom device firmware that strictly performs the audio recording tasks for optimal efficiency.

7.3.2. Microphones

Regarding the use of the dual microphones, and specifically the method in which they receive power and ground from the Audio Recorder, the use of an isolated power supply for the microphones is suggested to both further improve user-safety and also possibly decrease fluctuations in the power supply to the microphones. An isolated power supply is a second power supply that has no electronic connection to either the power or ground of the main power supply.

Regarding user-safety, the use of an isolated power supply increases user safety since it removes the possibility for the main power supply that powers the Audio Recorder to be applied to the user through the microphones. The isolated power supply would be used to power the two microphones solely with no connection to the main power or ground that powers the Audio Recorder. This arrangement could also possibly benefit the quality of the audio recordings, since as noted by this report, the 5 V and 3.3 V power supplies of the Raspberry Pi are somewhat electrically noisy. The use of an isolated power supply for the two microphones could eliminate the issues caused by noise in the power supply from the Raspberry Pi thus further improving signal quality. One suggestion for an appropriate isolated power supply would likely consist of a small, 3 V battery to power the microphone with perhaps an opto-coupler to couple the battery negative terminal to the ground of the main power supply so each power supply has the same reference value. Note however this setup has no electrical connection between the two power supplies.

7.3.3. Microphone Coupler & Air-Chamber

The final suggestion offered is regarding the Microphone Coupler and Air-Chamber design and relates to the secondary objective of the thesis. As presented, the filtering effects resulting from the dimensions of the Air-Chamber and the construction of the Microphone Coupler itself can help to explore specific frequency bands. Although previous literature can be useful to describe basic design guidelines, it is suggested to test additional Air-Chamber designs and construction techniques/materials that can help to show more clearly the higher frequency content which has not been observed or analyzed in the past. As was shown, even by selecting a slightly harder material for the Microphone Coupler acted to decrease sound absorption and hence increase the amplitude in the higher frequency range. Finally, it is suggested to capture respiratory sounds on a much larger subset of participants, both from individuals classified as healthy and those diagnosed with OSA, to see if the higher frequency spectral components play a role in OSA or possibly even other disease diagnosis.

Chapter 8

8. Appendix

8.1. Review of Sleep Apnea

Sleep apnea is characterized as an abnormal breathing condition occurring during sleep whereby an individual experiences repeated episodes of shallow breathing (hypopneas) or halted breathing (apneas), followed by abrupt awakenings to reinitiate regular air intake. Sleep apnea is divided among three sub-categorizations: obstructive sleep apnea (OSA), central sleep apnea (CSA), and complex/mixed sleep apnea (MSA). Obstructive sleep apnea is characterized by the inability to breath due to occlusion of the upper airway that occurs during sleep. Central sleep apnea arises as a result of irregular brain function during sleep that leads to an inactivation of the muscles controlling breathing. And lastly, complex/mixed sleep apnea is a condition that is formed from the combination of occlusion of the upper airway and inactivation of the muscles controlling breathing during sleep [28]. As we will see, the large degree of risk factors and associated anatomical and physiological criteria that contribute to the onset of OSA lead to the conclusion that OSA is the most common type of sleep apnea. This review, hence, will focus only upon the topic of OSA and not the other, less common types of sleep apnea.

OSA arises from the partial or complete occlusion of the upper airway in the regions of the soft palate and base of the tongue [29]. During OSA events, the brain senses the difficulty and/or inability to breathe, and the individual awakens so that conscious control of muscles controlling the upper airway can re-establish an open, unobstructed airway and normal breathing can continue. Within the realm of OSA, the severity of conditions experienced are described and differentiated by an apnea-hypopnea index; a classification that describes the number of apneas and hypopneas occurring per hourly period. Individuals considered to have mild OSA, on average, suffer from 5-15 events per hour and hence have an apnea-hypopnea index of 5-15. Individuals considered to have moderate OSA have an apnea-hypopnea index of 15-30, and finally individuals who experience greater than 30 apnea-hypopnea events per hour are classified as having severe OSA [30].

8.2. Normal Anatomy of the Upper Airway

The upper airway, also known as the upper respiratory tract, is anatomically defined as the passageway to the lungs comprised of both the oral and nasal cavities and includes the pharynx down to the superior aspect of the larynx. The region between the hard palate and the larynx, illustrated in Fig. 8.1, is the region of primary concern regarding OSA.

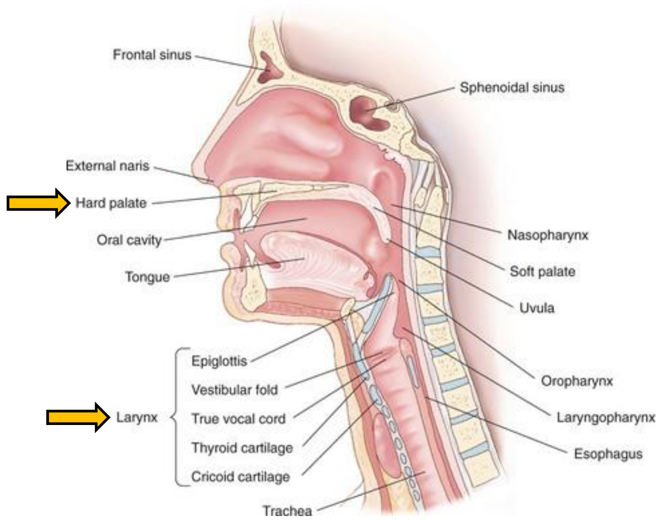

Figure 8.1. Anatomical structures of the adult human upper respiratory tract. Source: [44].

The upper airway can be described as a u-shaped fibromuscular tube innervated by many small and specialized muscles; however, it lacks any structural support by bone [31]. The upper airway in general performs a multitude of functional tasks in the everyday roles of human beings; the upper airway must meet the requirements to perform as a passage for fresh air intake to the lungs, assist in producing vocal sounds, and additionally must permit the passage of food and liquids as they pass to the esophagus. As one might expect, a complex set of functions leads to an inherent complexity in structure. To perform the tasks of swallowing and speech generation, the region of the upper airway between the hard palate and the larynx must be exceptionally flexible, and in certain situations must close completely. This area of the upper airway is aptly named the collapsible region [31]. To breath however, the collapsible region of the upper airway is required to remain dilated. It is the failure of the collapsible region of the upper airway to remain dilated during periods of sleep that leads to a difficulty to breath, and ultimately to OSA [32].

8.3. Epidemiology of Obstructive Sleep Apnea

OSA and its prevalence was not clinically recognized up until about 30 years ago, and even once recognized, knowledge was limited or non-existent outside the realms of sleep medicine. In addition, there were no clear-cut conditions leading to the cause of OSA. Following several large population-based studies, OSA and its overwhelming prevalence blind-sighted the medical community. By one critical analysis of the results of 12 studies, the estimated prevalence of OSA within western populations was found to be within 1-5% of adult men [33]. This estimate however only accounts for the individuals who willingly reported apneic events and thus diagnosed after sleep recording. Another study stated within the same journal paper estimates that for the western population as a whole (diagnosed and undiagnosed), up to 28% suffer from mild OSA, and up to 14% suffer from moderate OSA [33].

8.4. Etiology of Obstructive Sleep Apnea

Our general understanding of the major functions and/or functional deficits has allowed us some understanding of reasons to why OSA has become such a prevalent condition. In individuals suffering from OSA, it is known that airway collapse typically occurs in the regions posterior to the hard palate (i.e., velopharynx), posterior to the tongue (i.e., oropharynx), or both. It is known that during sleep, it is normal for many of the upper airway dilator and rigidity muscles have a decreased contractile power; the genioglossus and geniohyoid being the most greatly affected [34].

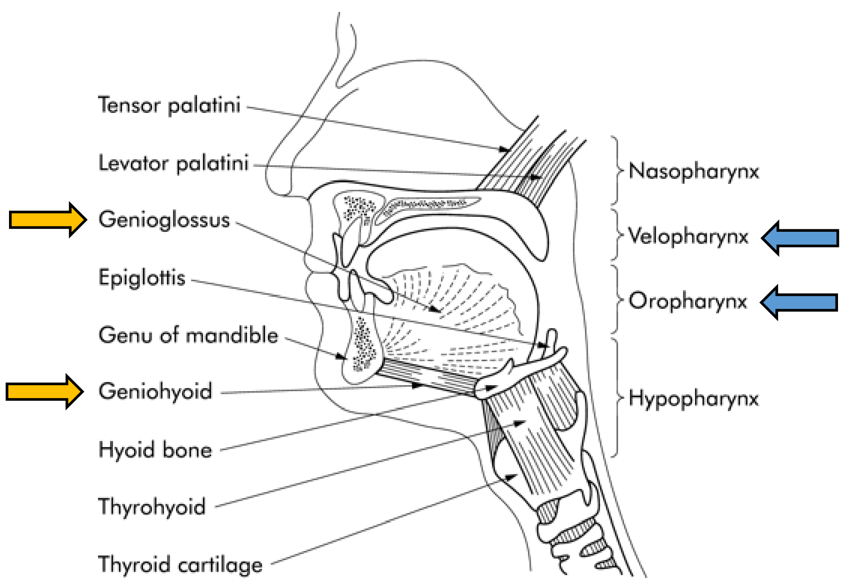

Figure 8.2. Anatomy of the upper airway showing regions of the airway and the muscles important in controlling airway dilation. Source: [43].

Now if the airway has abnormal anatomic features, or has excess tissue or pressures applied from surrounding tissues, the decreased contractile power of the dilator muscles is not enough to dilate the airway in these individuals, which ultimately results in the collapse of the soft tissues in this region. Hormonal imbalance is a key factor that is thought to be a contributor to the onset of OSA and may certainly help to explain why OSA is so more prevalent in males than in females, as well as after puberty rather than before [32]. Testosterone in males in a most general description is known to cause increased muscle bulk. In some individuals, higher than normal testosterone levels result in the increased parapharyngeal muscle bulk, including the region of the upper airway. Such muscle bulk has the effect of placing additional pressure on the outside walls of the upper airway tube. The increased pressure placed upon the exterior walls of the upper airway decreases the diameter of the upper airway and dictates that the muscles acting to dilate the upper airway must work at an increased effort to overcome the additional bulk. Both of these factors increase upper airway resistance and the tendency of the of the airway to collapse, especially during sleep.

More commonly, and in other cases, lower-than-average overall testosterone levels in men have shown increased risk for developing OSA [35] [36]. The decreased levels of testosterone in such individuals caused an increased level of adiposity throughout the body, including the structures of the neck surrounding the upper respiratory tract. The accumulation of adipose tissue in the areas of the upper airway has the same effects as the increased muscle bulk of the neck mentioned above; increased adipose tissue places additional pressure on the exterior walls of the upper airway, decreases the diameter of the upper airway, and dictates that the muscles acting to dilate the upper airway must work at an increased effort to overcome the additional tissue bulk. Once again, these factors increase upper airway resistance and the tendency of the of the airway to collapse [36].

Mandibular abnormalities also show correspondence to OSA. Mandible or tongue deformations such as a highly arched hard palate, small jaw, overbite, long face, and/or triangularly shaped chin may alter the ability of parapharyngeal muscles to maintain an unobstructed airway and hence collapse of the airway is experienced and OSA results [37]. Another common abnormality often associated with OSA is an inferiorly placed hyoid bone relative to the mandible, which results in narrowing of the upper airway [38]. As we have seen with other conditions, narrowing of the upper airway is closely linked to the tendency for the collapse of said airway, and hence OSA commonly develops. Infants who have suffered from chronic nasal obstruction in the past and who have thus adapted to sleep breathing primarily through their mouths can be left with altered mandibular structures as well, predisposing them to the onset of OSA in later years of life [38].

It must be clarified that, of all these factors listed above, no one factor can be ruled at the sole culprit for causing OSA. It is important to keep in mind that the upper airway is required to perform a multitude of tasks and in doing so must be able to alter its structure to be exceptionally rigid for unobstructed air intake, yet also collapse near completely for tasks such as speech generation or food ingestion. To accomplish such a variety of tasks, the upper airway must operate with a precise balance of muscle innervation, surrounding tissue pressure, air resistance, etc. Any of the deficits listed above result in small alterations to the upper airway and its control. Such small alterations “tip the balance” of the upper airway towards the tendency to collapse when conscious control is unable to compensate for abnormalities or deficits. It is for this reason that there exists a great difficulty in being able to easily diagnose OSA and its severity amongst those suffering from it.

8.5. Implications of Obstructive Sleep Apnea

OSA has severe implications and poses a serious health risk to affected individuals. The primary impact resulting from airway obstruction is the limitation of oxygen intake to the body. During these periods of limited oxygen intake, the concentration of carbon dioxide in the blood increases, and conversely the concentration of oxygen decreases. The body senses this increased concentration of carbon dioxide and communicates to the heart to work at an increased rate to compensate to increase blood oxygen concentration. It has been shown that a continuous increased workload placed upon the heart due to OSA can lead to increased blood pressure [39], risk of congestive heart failure, and even a stroke [40]. As well, the continued awakenings associated with OSA to consciously open the upper airway have seriously worrying implications as well. The inability to have an uninterrupted sleep night after night leads to chronic tiredness throughout the day (i.e., hypersomnia) which can lead to ongoing headaches, irritability, mood disorders, anxiety, depression, and most critically a lack of concentration; especially a risk when driving/operating dangerous equipment [28].

8.6. Audio Recorder Connectivity Flowchart

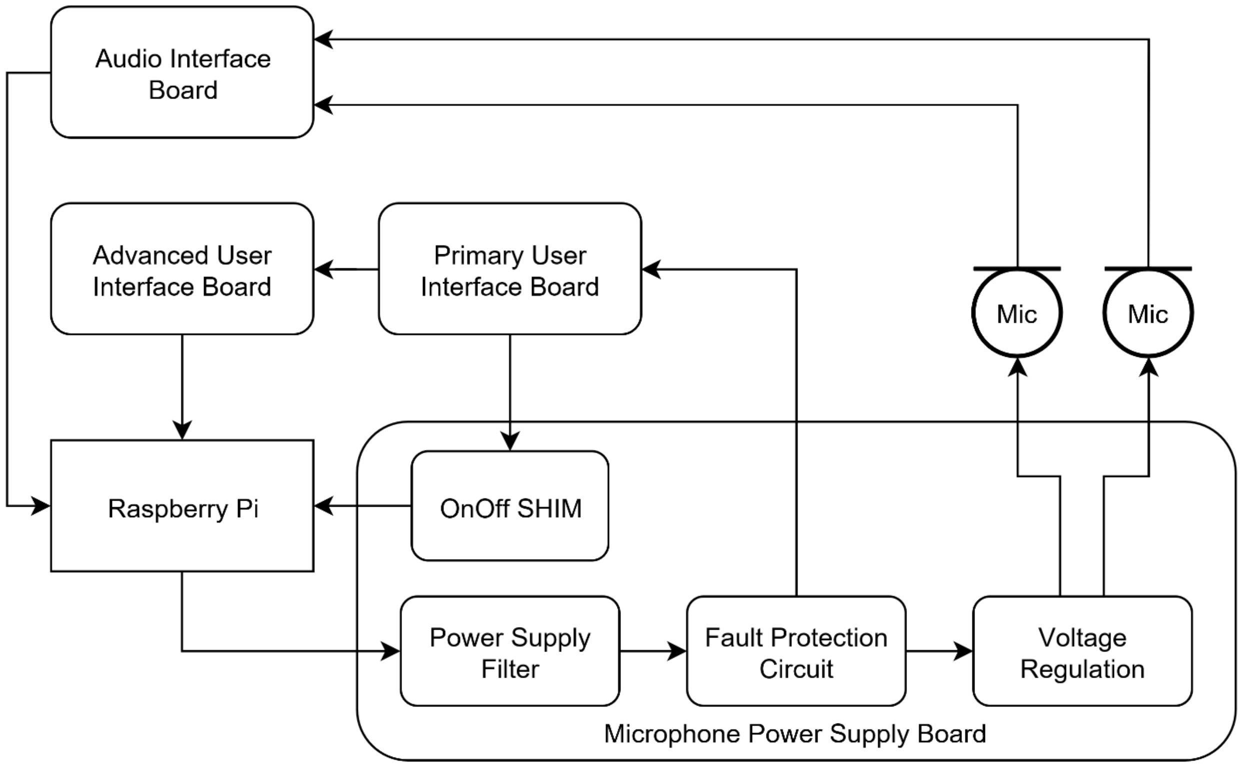

Figure 8.3. Chart showing interconnectivity of all components of the Audio Recorder.

8.7. Circuit Schematics

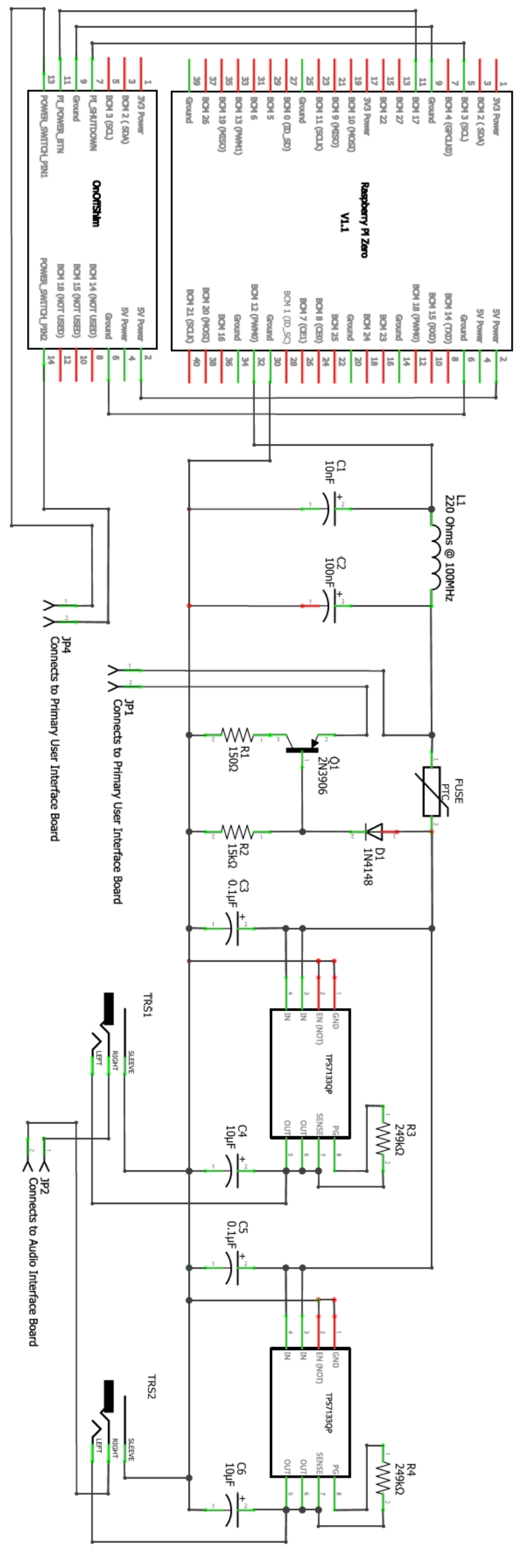

Figure 8.4. Circuit schematic for Microphone Power Supply Board.

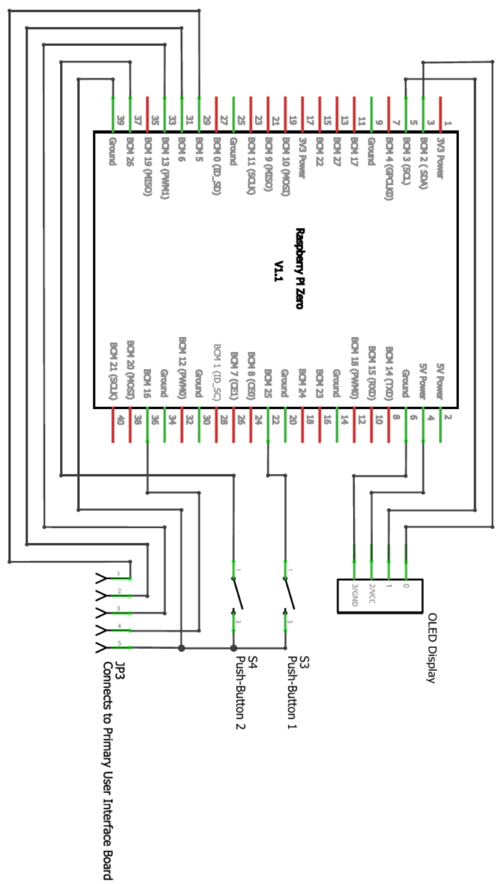

Figure 8.5. Circuit schematic for Advanced User Interface Board.

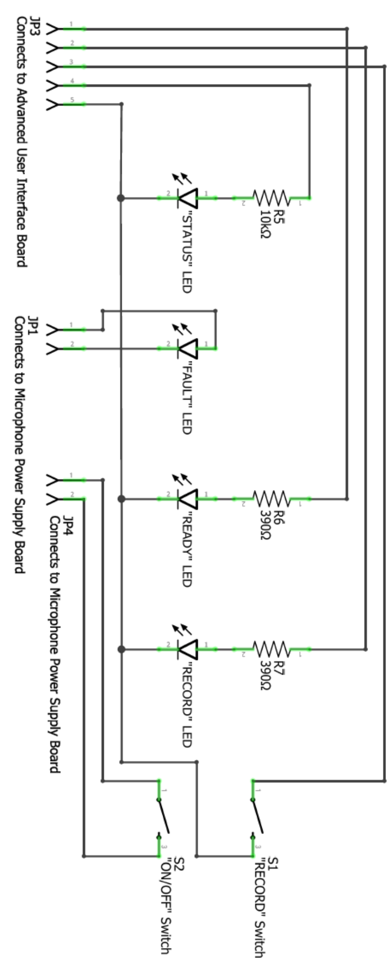

Figure 8.6. Circuit schematic for Primary User Interface Board.

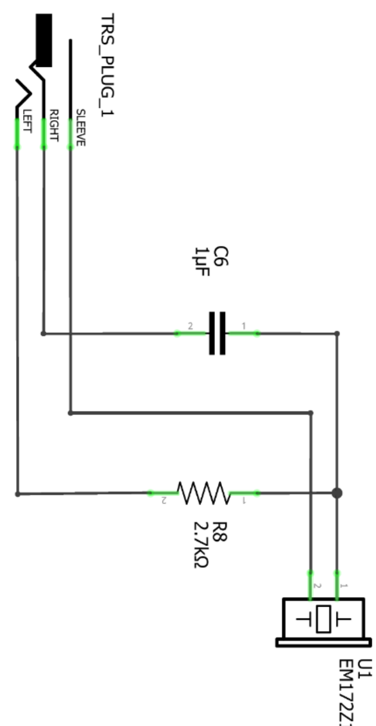

Figure 8.7. Circuit schematic for Microphone Drive Circuit.

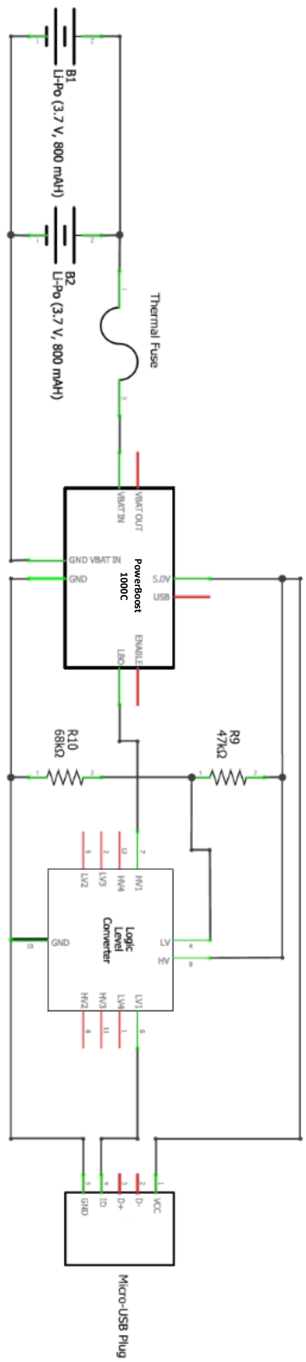

Figure 8.8. Circuit schematic of Battery Module.

8.8. Microphone Isolation Box

The microphone isolation box referred to within this report is a custom designed and fabricated sound isolation box to suppress sound reflections from the sound source and is shown in Fig. 8.9:

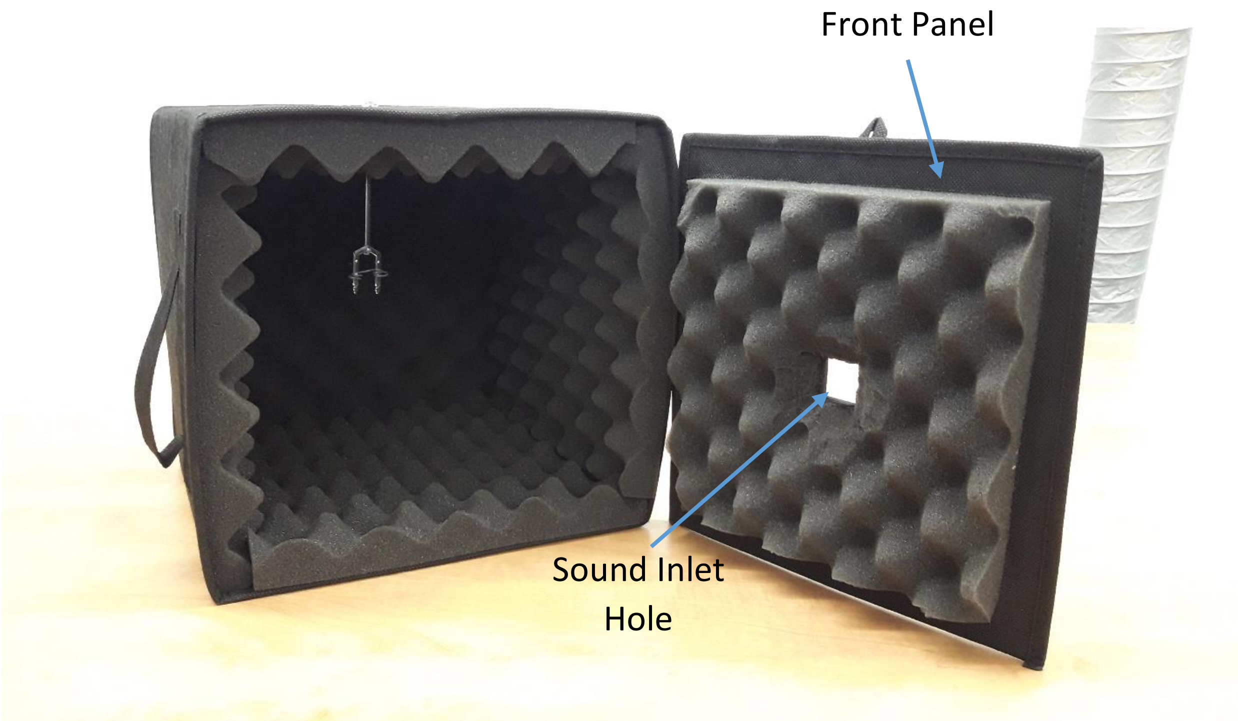

Figure 8.9. Microphone Sound Isolation Box with front panel opened.

The sound isolation box was constructed from a fabric storage bin of dimensions 28 cm x 28 cm x 28 cm. Acoustic foam (Manufacturer: Arrowzoom, Product Number: (25 cm x 25 cm x 3 cm) Convoluted Egg Crate Acoustic Foam) provides the suppression from sound reflections and was applied on all interior walls of the storage bin including the backside of the front panel. A small, 2.54 cm square hole was cut in the front panel to act as the sound inlet hole to which the sounds from a speaker enter the isolation box.

For all tests that utilized the Microphone Isolation Box, the front panel was installed to form a sealed box (minus the sound inlet hole). Microphones being tested were placed in the same location for all tests, near to the back of the interior of the isolation box, approximately 20 cm from the sound inlet hole.

Figure 8.10. Microphone being tested placed inside the Microphone Isolation Box.

8.9. Project Budget

Table 8.9-1. Project Budget

Module:	Manufacturer:	Device:	Product Number:	Quantity:	Unit Cost:	Total Cost:
Central Processing Unit	Raspberry Pi Foundation	Raspberry Pi Zero W	Pi Zero v1.3	1	$13.18	$13.18
	Samsung	Micro SD Card	MB-MC32GA/CA	1	$10.98	$10.98
	DFRobot	Heatsink	FIT0367	1	$1.53	$1.53
	Adafruit Industries LLC.	40-pin Header Pins (Long)	400	1	$3.95	$3.95
						$29.64
Audio Interface Board	Fe-Pi	Audio Z v2	Audio Z v2	1	$18.30	$18.30
	Adafruit Industries LLC.	40-pin Header Socket (Stacking)	2223	1	$3.29	$3.29
	Mill-Max Manufacturing	Male Printed Circuit Pins	800-10-020-10-002000	2	$0.21	$0.42
	Laird-Signal Integrity Products	Ferrite Sheet	MHLL12060-200	1	$9.32	$9.32
	Jeff Winkler	Plastic Sheeting	Custom Part	1	$2.00	$2.00
						$33.33
Microphone Power Supply Board	JLCPCB	Printed Circuit Board	Custom Part	1	$0.95	$0.95
	Pimoroni	OnOff SHIM	PIM269	1	$9.16	$9.16
	Texas Instruments	Voltage Regulator	TPS7133QDR	2	$5.88	$11.76
	AVX Corporation	10 µF Tantalum Capacitor	TAJA106K006SNJ	2	$0.36	$0.72
	Yageo	249 kΩ Resistor	RT1206BRD07249KL	2	$0.65	$1.30
	Kycon Inc.	3.5mm Female Socket	STX-3120-3B-284C	1	$1.17	$1.17
	Kycon Inc.	3.5mm Female Socket	STX-3120-3B-577C	1	$1.17	$1.17
	Mill-Max Manufacturing	Female Printed Circuit Pins	310-13-164-41-001000	2	$0.19	$0.38

	Murata Electronics	Resettable Fuse	PRG21AR220MS1RK	1	$1.53	$1.53
	Diodes Incorporated	PNP Transistor	ZXTP19100CFFTA	1	$1.07	$1.07
	Yageo	150Ω Resistor	RC1206JR-07150RL	1	$0.10	$0.10
	Yageo	15kΩ Resistor	RC1206JR-0715KL	1	$0.10	$0.10
	Diodes Incorporated	Diode	1N4148W-7-F	1	$0.22	$0.22
	KEMET	10 nF Capacitor	C1206C103JARACTU	1	$0.21	$0.21
	KEMET	100 nF Capacitor	T491A104M035AT	3	$0.51	$1.53
	Taiyo Yuden	Ferrite Bead	FBMH3216HM221NT	1	$0.29	$0.29
	Samtec Inc.	2-pin Header Socket	ESQ-102-33-G-S	2	$1.62	$3.24
	Adafruit Industries LLC.	40-pin Header Short Socket	2243	1	$2.57	$2.57
						$37.47
Primary User Interface Board	JLCPCB	Printed Circuit Board	Custom Part	1	$0.83	$0.83
	C&K	Red-Colored Push Button	D6R40 F2 LFS	1	$1.84	$1.84
	C&K	Black-Colored Push Button	D6R90 F2 LFS	1	$1.84	$1.84
	Broadcom Limited	Blue LED	HLMP-DB25-B0000	1	$1.45	$1.45
	Adafruit Industries LLC.	Yellow LED	2700	1	$0.26	$0.26
	Rohm Semiconductor	Green LED	SLA-560MT3F	1	$0.89	$0.89
	Rohm Semiconductor	Red LED	SLA-560LT3F	1	$0.98	$0.98
	Essentra Components	LED Spacer 6mm	LEDM-3-06	2	$0.70	$1.40
	Keystone Electronics	LED Spacer 7mm	8320	2	$0.34	$0.68
	Panasonic Electronic Components	390Ω Resistor	ERJ-8GEYJ391V	2	$0.15	$0.30
	Panasonic Electronic Components	10kΩ Resistor	ERJ-8ENF1002V	1	$0.14	$0.14

	TE Connectivity AMP Connectors	5-pin Header Pin Connector	5-535541-3	1	$2.26	$2.26
						$12.87
Advanced User Interface Board	JLCPCB	Printed Circuit Board	Custom Part	1	$0.64	$0.64
	Adafruit Industries LLC.	40-pin Header Normal Socket	2222	1	$1.98	$1.98
	TinySine	OLED Display	G5780D31C08EE9	1	$4.89	$4.89
	Omron Electronics Inc-EMC Div	Yellow Push Button	B3F-1062	1	$0.65	$1.30
	Omron Electronics Inc-EMC Div	Black Push Button	B3F-1060	1	$0.56	$1.12
						$9.93
Audio Recorder Miscellaneous	Jeff Winkler	Enclosure Top	Custom Part	1	$20.00	$20.00
	Jeff Winkler	Enclosure Bottom	Custom Part	1	$12.00	$12.00
	Jeff Winkler	OLED Screen Surround Trim	Custom Part	1	$2.00	$2.00
	Sandisk	USB Drive	SDDD3-032G-G46	1	$13.18	$13.18
	Essentra Components	Nylon Bolt	3404400137	2	$0.20	$0.40
	Essentra Components	Nylon Bolt	010440S100	4	$0.15	$0.60
	Essentra Components	Nylon Bolt	010440P137	4	$0.15	$0.60
	Keystone Electronics	Nylon Nut	9605	26	$0.27	$7.02
	RAF Electronic Hardware	Nylon Standoff	2054T-440-N	2	$2.62	$5.24
	Essentra Components	Nylon Standoff	15TSP106	2	$1.33	$2.66
	Keystone Electronics	Nylon Washer	3356	2	$0.15	$0.30
						$64.00
Microphones	JLCPCB	Printed Circuit Board	Custom Part	2	$0.86	$1.72
	Jeff Winkler	Microphone Coupler	Custom Part	2	$5.00	$10.00
	Jeff Winkler	Microphone Coupler Cap	Custom Part	2	$0.50	$1.00

	Primo	Microphone	EM172	2	$20.99	$41.98
	Micbooster	Rubber Isolator	FC037	2	$0.31	$0.62
	AVX Corporation	1µF Capacitor	TAJR105M020RNJ	2	$0.42	$0.84
	Yageo	2.7kΩ Resistor	RT0805BRD072K7L	2	$0.46	$0.92
	Mill-Max Manufacturing Corp.	Male Printed Circuit Pins	9137-0-00-15-00-00-38-0	4	$0.82	$3.28
	Neutrik	3.5 mm Stereo Plug	NYS231BG	2	$3.26	$6.52
	Tensility International Corp	Shielded Cable	30-00278	1	$16.32	$16.32
						$83.20
	Tattu	Battery Cell	3.7V 800mAh Li-Po	2	$5.00	$10.00
	Adafruit Industries LLC.	PowerBoost 1000C	2465	1	$26.30	$26.30
	Broadcom Limited	Blue LED	HLMP-DB25-B0000	1	$1.45	$1.45
	Adafruit Industries LLC.	Yellow LED	2700	1	$0.26	$0.26
	Rohm Semiconductor	Green LED	SLA-560MT3F	1	$0.89	$0.89
	Rohm Semiconductor	Red LED	SLA-560LT3F	1	$0.98	$0.98
	BusBoard Prototype Systems	Solderable Breadboard	SB300	1	$6.50	$6.50
	ZF Electronics	Rocker Switch	PRK22J5DBBNN	1	$1.72	$1.72
Battery	Adafruit Industries LLC.	Micro-USB Male Plug	1826	1	$1.36	$1.36
	Cantherm	Thermal Fuse	SDF DF072S	1	$1.70	$1.70
	SparkFun Electronics	Logic Level Converter	BOB-12009	1	$4.24	$4.24
	JST Sales America Inc.	2-pin JST Plug	PHR-2	1	$0.14	$0.14
	JST Sales America Inc.	2-pin JST Socket	B2B-PH-K-S(LF)(SN)	1	$0.24	$0.24
	Jeff Winkler	Enclosure Top	Custom Part	1	$15.00	$15.00
	Jeff Winkler	Enclosure Bottom	Custom Part	1	$8.00	$8.00
	Jeff Winkler	Enclosure Attachement Pieces	Custom Part	2	$2.50	$5.00
	JST Sales America Inc.	6-pin JST Male Plug	B6B-EH-A(LF)(SN)	1	$0.42	$0.42

	JST Sales America Inc.	6-pin JST Female Socket	EHR-6	1	$0.14	$0.14
	JST Sales America Inc.	JST Wire Leads	ASEHSEH22K152	4	$0.63	$2.52
						$86.86
					Grand Total:	**$357.30**

(Note that all prices listed are in Canadian dollars (CAD))

References

[1] M. Mussel, "The need for standards in recording and analysing respiratory sounds," *Medical and Biological Engineering and Computing,* vol. 30, no. 2, pp. 129-139, 1992.

[2] A. Elwali and Z. Moussavi, "A novel diagnostic decision making procedure for screening obstructive sleep apnea using anthropometric information and tracheal breathing sounds during wakefulness," *Scientific Reports (Nature),* vol. 9, no. 11467, 2019.

[3] A. Elwali and Z. Moussavi, "Obstructive Sleep Apnea Screening and Airway Structure Characterization During Wakefulness Using Tracheal Breathing Sounds," *Annals of Biomedical Engineering,* vol. 45, no. 3, pp. 839-850, 2017.

[4] N. Gavriely, Y. Palti and . G. Alroy, "Spectral characteristics of normal breath sounds," *Journal of Applied Physiology,* vol. 50, pp. 307-314, 1981.

[5] K. K. Motamedi, A. C. McClary and R. G. Amedee, "Obstructive Sleep Apnea: A Growing Problem.," *Ochsner,* vol. 9, no. 3, pp. 149-153, 2009.

[6] F. Chung, H. R. Abdullah and P. Liao, "Stop-Bang Questionnaire: A practical Approach to screen Obstructive Sleep Apnea," *CHEST,* vol. 149, no. 3, pp. 631-638, 2016.

[7] F. Chung, R. Subramanyam, P. Liao, E. Sasaki, C. Shapiro and Y. Sun, "High STOP-Bang score indicates a high probability of obstructive sleep apnoea," *BJA: British Journal of Anaesthesia,* vol. 108, no. 5, pp. 768-775, 2012.

[8] A. Yadollahi, E. Giannouli and Z. Moussavi, "Sleep apnea monitoring and diagnosis based on pulse oximetery and tracheal sound signals," *Medical & biological engineering & computing,* vol. 48, no. 11, pp. 1087-1097, 2010.

[9] F. Hajipour, A. Elwali, M. Jafari-Jozani and Z. Moussavi, "Regularized Logistic Regression for Obstructive Sleep Apnea Screening during Wakefulness Using Daytime Tracheal Breathing Sounds and Anthropometric Information," *Medical & Biological Engineering & Computing,* vol. 57, no. 12, pp. 2641-2655, 2019.

[10] H. Nakano, M. Hayashi, E. Ohshima, N. Nishikata and T. Shinohara, "Validation of a new system of tracheal sound analysis for the diagnosis of sleep apnea-hypopnea syndrome," *Sleep,* vol. 27, no. 5, pp. 951-957, 2004.

[11] A. Kulkas, E. Huupponen, J. Virkkala, M. Tenhunen, A. Saastamoinen, E. Rauhala and S.-L. Himanen, "New tracheal sound feature for apnoea analysis," *Medical & biological engineering & computing,* vol. 47, no. 4, pp. 405-412, 2009.

[12] H. Pasterkamp, S. S. Kraman and G. R. Wodicka, "Respiratory Sounds Advances Beyond the Stethoscope," *American Journal of Respiratory and Critical Care Medicine,* vol. 156, pp. 974-987, 1997.

[13] A. Yadollahi, A. Montazeri, A. Azarbarzin and Z. Moussavi, "Respiratory flow-sound relationship during both wakefulness and sleep and its variation in relation to sleep apnea," *Annals of Biomedical Engineering,* vol. 41, no. 3, pp. 537-546, 2013.

[14] A. Yadollahi and Z. Moussavi, "Acoustical Flow Estimation: Review and Validation," *IEEE EMB Magazine,* vol. 26, no. 1, pp. 56-61, 2007.

[15] Z. Moussavi, M. Leopando, H. Pasterkamp and G. Rempel, "Computerized Acoustical Respiratory Phase Detection without Airflow Measurement," *Medical and Biological Engineering and Computing,* vol. 38, no. 2, pp. 198-203, 2000.

[16] J. S. Chuah and Z. K. Moussavi, "Automated Respiratory Phase Detection by Acoustical Means," *Systemics, Cybernetics and Informatics (SCI),* vol. Conference, pp. 228-231, 2000.

[17] J. Gnitecki, Z. Moussavi and H. Pasterkamp, "Diagnostic potential in state space parameters of lung sounds," *Medical & Biological Engineering & Computing,* vol. 46, pp. 93-99, 2008.

[18] S. A. Taplidou and L. J. Hadjileontiadis, "Wheeze detection based on time-frequency analysis of breath sounds," *Computers in Biology and Medicine,* vol. 37, no. 8, pp. 1073-1083, 2007.

[19] C. S. Sapp, "WAVE PCM soundfile format," [Online]. Available: http://soundfile.sapp.org/doc/WaveFormat/. [Accessed 26 November 2019].

[20] Future Technology Devices International Limited (FTDI), "FTDI Chip," 1 November 2013. [Online]. Available: https://www.ftdichip.com/Support/Documents/AppNotes/AN_146_USB_Hardware_Design_Guidelines_for_FTDI_ICs.pdf. [Accessed 25 November 2019].

[21] H. Pasterkamp, S. S. Kraman, P. D. DeFrain and G. R. Wodicka, "Measurement of Respiratory Acoustical Signals: Comparison of Sensors," *Chest,* vol. 104, no. 5, pp. 1518-1525, 1993.

[22] M. T. Pourazad, Z. Moussavi and G. Thomas, "Heart Sound Cancellation from Lung Sound Recordings Using Time-Frequency Filtering," *Medical and Biological Engineering and Computing,* vol. 44, no. 3, pp. 216-225, 2006.

[23] S. Huq and Z. Moussavi, "Acoustic Breath-Phase Detection Using Tracheal Breath Sounds," *Medical & Biological Engineering & Computing,* vol. 50, pp. 297-308, 2012.

[24] A. Montazeri, E. Giannouli and Z. Moussavi, "Assessment of obstructive sleep apnea and its severity during wakefulness," *Annals of biomedical engineering,* vol. 40, no. 4, pp. 916-924, 2012.

[25] G. R. Wodicka, S. S. Kraman, G. M. Zenk and H. Pasterkamp, "Measurement of Respiratory Acoustic Signals: Effect of Microphone Air Cavity Depth," *Chest,* vol. 106, pp. 1140-1144, 1994.

[26] S. S. Kraman, H. Pasterkamp, G. R. Wodicka and Y. Oh, "Measurement of respiratory acoustic signals: effect of microphone air cavity width, shape and venting," *Chest,* vol. 108, no. 4, p. 1004–1008, 1995.

[27] H. Li, J. Gao and S. Zhang, "Effect of Overdischarge on Swelling and Recharge Performance of Lithium Ion Cells," *Chinese Journal of Chemistry,* vol. 26, pp. 1585-1588, 2008.

[28] Mayo Foundation for Medical Education and Research, "Mayo Clinic," 25 August 2015. [Online]. Available: http://www.mayoclinic.org/diseases-conditions/sleep-apnea/basics/definition/con-20020286.

[29] W. Schmidt-Nowara, A. Lowe, L. Wiegand, R. Cartwright, F. Perez-Guerra and S. Menn, "Oral Appliances for the Treatment of Snoring and Obstructive Sleep Apnea: A Review," *Sleep,* pp. 501-510, 1995.

[30] A. S. M. Shamsuzzaman, B. J. Gersh and V. K. Somers, "Obstructive Sleep Apnea: Implications for Cardiac and Vascular Disease," *JAMA: Clinical Cardiology: Clinician's Corner,* pp. 1906-1914, 2003.

[31] I. R. Morris, "Functional anatomy of the upper airway.," *Emergency Medical Clinics of North America,* pp. 639-669, 1988.

[32] D. J. Eckert and A. Malhotra, "Pathophysiology of Adult Obstructive Sleep Apnea," *Proceedings of the American Thoracic Society,* pp. 144-153, 2008.

[33] T. Young, P. E. Peppard and D. J. Gottlieb, "Epidemiology of Obstructive Sleep Apnea: A Population Health Perspective," *Epidemiology of Obstructive Sleep Apnea,* pp. 1217-1239, 2002.

[34] S. Chokroverty, Sleep Disorders Medicine: Basic Science, Technical Considerations, and Clinical Aspects, Butterworth-Heinemann, 2013.

[35] E. Barrett-Connor, T.-T. Dam, K. Stone, S. L. Harrison, S. Redline and E. Orwoll, "The Association of Testosterone Levels with Overall Sleep Quality, Sleep Architecture, and Sleep-Disordered Breathing," *Journal of Endocrinal Metabolism,* pp. 2602-2609, 2008.

[36] G. Wittert, "The relationship between sleep disorders and testosterone in men," *Asian Journal of Andrology,* pp. 262-265, 2014.

[37] M. S. Aldrich, Sleep Medicine, Oxford University Press, 1999.

[38] P. A. Cistulli, "Craniofacial abnormalities in obstructive sleep apnoea: Implications for treatment," *Respirology,* pp. 167-174, 1996.

[39] B. Phillips, K. Narkiewicz, C. A. Pesek, W. G. Haynes, M. E. Dyken and V. K. Somers, "Effects of obstructive sleep apnea on endothelin-1 and blood pressure," *Journal of Hypertension,* pp. 61-66, 1999.

[40] H. K. Yaggi, J. Concato, W. N. Kernan, J. H. Lichtman, L. M. Brass and V. Mohsenin, "Obstructive Sleep Apnea as a Risk Factor for Stroke and Death," *The New England Journal of Medicine,* pp. 2034-2041, 2005.

[41] M. Hawkins, "Raspberry Pi Spy," 18 July 2014. [Online]. Available: https://www.raspberrypi-spy.co.uk/2014/07/raspberry-pi-b-gpio-header-details-and-pinout/. [Accessed 5 December 2019].

[42] M. Gololicic, "Healthiack," [Online]. Available: https://healthiack.com/encyclopedia/pictures-of-chest-2. [Accessed 12 12 2020].

[43] R. Fogel, A. Malhotra and D. White, "Sleep. 2: pathophysiology of obstructive sleep apnoea/hypopnoea syndrome.," *Thorax,* vol. 59, no. 2, pp. 159-163, 2004.

[44] W. Chapleau and P. T. Pons, Emergency Medical Technician: Making the Difference, Mosby JEMS - Elsevier, 2006.

[45] "Sparkfun," [Online]. Available: https://cdn.sparkfun.com/assets/learn_tutorials/1/9/3/npn-pnp-symbols.png. [Accessed 15 December 2019].

[46] "Seeed Studio," 2018-2019. [Online]. Available: https://www.seeedstudio.com/Seeedstudio-Raspberry-Pi-Zero-W-Barebones-Kit.html. [Accessed 14 December 2019].

[47] "PowerBoost 1000 Charger - Rechargeable 5V Lipo USB Boost @ 1A - 1000C," Adafruit, [Online]. Available: https://www.adafruit.com/product/2465. [Accessed 18 December 2019].

[48] "Pimoroni," [Online]. Available: https://shop.pimoroni.com/products/onoff-shim. [Accessed 5 December 2019].

[49] Primo Co., Ltd. , "Micbooster," July 2015. [Online]. Available: micbooster.com/documents/EM172Z1%20July%202015.pdf. [Accessed 30 09 2020].

[50] "Fe-Pi," 2019. [Online]. Available: https://fe-pi.com/products/fe-pi-audio-z-v2. [Accessed 25 November 2019].

[51] "FEL Communications Ltd.," Micbooster.com, [Online]. Available: https://micbooster.com/primo-microphone-capsules/8-primo-em172.html. [Accessed 15 October 2020].

[52] "Eventide," 23 April 2017. [Online]. Available: https://www.eventideaudio.com/community/forum/stompboxes/replacing-midi-connectors-all-factor-pedals. [Accessed 19 December 2019].

[53] "Brüel & Kjær Products: TYPE 2250-S," [Online]. Available: https://www.bksv.com/en/products/measuring-instruments/sound-level-meter/2250-series/Type-2250-S. [Accessed 08 12 2020].